

UNIVERSITY OF PADOVA



Master Thesis in Bioengineering

Correlation of BOLD signal and kinematics during a reach-to-grasp movement

Giulia Bertó

SUPERVISORS:

Prof.ssa Alessandra Bertoldo

Prof. Umberto Castiello

14th of July 2015

Contents

Introduction	7
Synopsis	9
1 Reach-To-Grasp Movement	11
1.1 Phases and types of movement	11
1.2 Morphological and functional hand evolution	12
1.3 A developmental view	12
1.4 The kinematics of grasping	13
1.5 Neurophysiology in monkey studies	14
1.6 Neuroanatomical pathways and neuroimaging in human studies	17
1.6.1 Motor cortical pathways	17
1.6.2 Somatosensory pathways	18
1.6.3 Subcortical pathways	20
1.6.4 Neuroimaging studies using fMRI technique	20
1.7 Combining different techniques: fMRI and kinematic data	22
2 Functional Magnetic Resonance Imaging	23
2.1 Introduction	23
2.2 MRI scanner	24
2.3 Bases of MR signal generation	26
2.3.1 Equilibrium condition	26
2.3.2 Spin excitation	28
2.3.3 Spin relaxation	29
2.4 BOLD signal	30
2.4.1 BOLD contrast	31
2.4.2 Hemodynamic response	32
2.5 Experimental design	34
2.6 fMRI data preprocessing	36
2.6.1 Slice timing correction	36

2.6.2	Motion correction	37
2.6.3	Coregistration	38
2.6.4	Normalization	39
2.6.5	Spatial smoothing	39
2.7	Statistical analysis	40
2.7.1	General Linear Model	41
2.7.2	Correction for multiple comparisons	44
3	Kinematic Analysis	47
3.1	Principles of kinematic analysis	47
3.1.1	Non-optical systems	47
3.1.2	Optical systems	48
3.2	Kinematic analysis with SIMI Motion©	51
4	Materials	55
4.1	Participants	55
4.2	Apparatus	55
4.2.1	fMRI scanner	55
4.2.2	Motion capture system	55
5	Methods	57
5.1	Preparation	57
5.1.1	Cameras settings	57
5.1.2	3D Calibration	57
5.1.3	Markers placement	59
5.2	Experimental protocol	60
5.3	Data acquisition	61
5.3.1	Kinematic data acquisition	61
5.3.2	fMRI data acquisition	61
5.4	Preprocessing of fMRI data	61
5.5	Data analysis	67
5.5.1	Kinematic quantities computation	68
5.5.2	Kinematic parameters extraction	68
5.5.3	Linear regression analysis	70
5.5.4	1st level analysis	71
5.5.5	2nd level analysis	74
5.5.6	Strategy identification	76

6	Results and dicussions	79
6.1	3D Calibration	79
6.2	Preprocessed fMRI data quality check	80
6.3	Kinematic quantities computation	81
6.4	Kinematic parameters extraction	83
6.5	Linear regression analysis	85
6.6	Kinematic regressors selection	87
6.7	Hemodynamic response model selection	89
6.8	2nd level approach selection	92
7	Conclusions	99
	Bibliography	101
	List of Figures	108
	List of Tables	112

Introduction

The reach-to-grasp movement is a common gesture that all of us continuously perform during our everyday life. Even if it is a simple and spontaneous action that we have been learnt to execute since the first months of our life, the neural mechanisms which underlie its planning and its execution are very complex. Reaching, grasping and manipulating an object are actions that require multiple visuomotor transformation which imply the ability to transform the visual features of the object in the appropriate hand configuration and the capacity to perform and control the hand and the fingers movement.

A significant number of behavioural studies were conducted with monkeys in order to understand the neural circuit involved in the reach-to-grasp movement. Specific areas related to grasping have been identified in the monkey cortex [24] [25]: they play a role in the 3D features representation of the object, in the motor prototype selection and in the final movement execution.

The natural question is whether a similar circuit exists in humans. Considerable progress towards understanding the neural substrate of grasping in humans has been mainly made from neuroimaging experiments [2]. These studies [43]-[54] suggest that in humans, like in monkeys, reach-to-grasp movements involve a large network of interconnected structures in the parietal and frontal lobes. Nevertheless, how the neural control systems interact with the complex biomechanics of moving arms remains an open question.

The aim of the present thesis is to investigate the correlation between the human brain activity recorded by fMRI technique and the kinematic signal coming from the moving arm during the reach-to-grasp movement. The goal to capture the complex natural cerebral activity requires a multimodal approach which take benefits from all the different techniques used. The simultaneous recording of the BOLD signal and the kinematic data allows to exploit the technical advantages of both the investigation methods. In particular, kinematic data become useful in order to compensate the low temporal resolution of the MR images. The aim is therefore to find which kinematic parameters correlate better with the BOLD signal in terms of brain activation from the onset to the end of the movement.

Introduzione

Il movimento di raggiungimento e prensione é un gesto comune che tutti noi continuamente eseguiamo durante la nostra vita quotidiana. Nonostante sia un'azione semplice e spontanea che abbiamo imparato a compiere sin dai primi mesi di vita, i meccanismi neurali che stanno alla base della sua pianificazione ed esecuzione sono molto complessi. Raggiungere, afferrare e manipolare un oggetto sono azioni che richiedono molteplici trasformazioni visuomotorie le quali implicano l'abilitá nel trasformare le caratteristiche visive dell'oggetto nell'appropriata configurazione della mano e la capacità di compiere e controllare il movimento della mano e delle dita.

Un numero significativo di studi comportamentali é stato effettuato sulle scimmie per comprendere il circuito neurale coinvolto nel movimento di raggiungimento e prensione. Sono state identificate specifiche aree connesse con la prensione nella corteccia della scimmia [24] [25]: esse svolgono un ruolo nella rappresentazione 3D delle caratteristiche dell'oggetto, nella selezione del prototipo motorio e nella finale esecuzione del movimento.

La domanda che sorge spontanea é se un circuito simile esista nell'uomo. Considerabili progressi verso la comprensione del substrato neurale della prensione nell'uomo sono stati principalmente raggiunti dagli esperimenti di neuroimaging [2]. Questi studi [43]-[54] suggeriscono che nell'uomo, come nella scimmia, il movimento di raggiungimento e prensione coinvolge una larga rete di strutture interconnesse nei lobi parietali e frontali. Nonostante ciò, come il sistema di controllo neurale interagisca con la complessa biomeccanica dell'arto superiore in movimento rimane una domanda aperta.

Lo scopo della presente tesi é quello di indagare la correlazione tra l'attività del cervello umano acquisita tramite la tecnica di risonanza magnetica funzionale e il segnale cinematico proveniente dall'arto superiore durante il movimento di raggiungimento e prensione. L'obiettivo di catturare la complessa naturale attività cerebrale richiede un approccio multimodale che sfrutta i benefici di tutte le diverse tecniche utilizzate. L'acquisizione simultanea del segnale BOLD e dei dati cinematici permette di sfruttare i vantaggi tecnici di entrambi i metodi di indagine. In particolare, i dati cinematici diventano utili per compensare la bassa risoluzione temporale delle immagini di risonanza. Lo scopo é quindi quello di trovare quali parametri cinematici correlino meglio con il segnale BOLD in termini di attivazione cerebrale dall'inizio alla fine del movimento.

Synopsis

Chapter 1 provides an overview on the state of the art of knowledge regarding the reach-to-grasp movement. First, a description of the movement with an evolutionary and developmental contextualization is given. Then results of studies conducted on reaching and grasping are reported, in particular regarding the kinematics of grasping, the neurophysiology in monkeys and the neuroanatomical pathways and neuroimaging in humans. Lastly the advantages of combining different investigation techniques in the study of the reach-to-grasp movement are shown.

In Chapter 2 the basic theory of fMRI technique is provided. In the first part, a brief overview on the MRI scanner, the physics of MR signal generation and BOLD signal are given. In the last part, the general steps of a standard fMRI experiment conduction are reported, from the experimental design to the statistical data analysis.

In Chapter 3 a summary of the kinematic analysis theory is given. In the first part, the principles of the kinematic analysis are treated, in particular the calibration, the 3D reconstruction and the tracking. In the second part, the ways to implement the same aspects by SIMI Motion©, the motion capture system used in the present thesis, are briefly illustrated.

In Chapter 4 indications about the participants of the experiments and about the main components of the experimental apparatus are given.

In Chapter 5 all the methods used in the present thesis are described. In the first part, the preparation, the experimental protocol, the data acquisition and the fMRI data preprocessing are explained. In the second part, all the strategies adopted to analyse the kinematic data and the fMRI data are given.

In Chapter 6 all the results found from the implemented methods are collected and discussed. First, the results of the calibrations comparison and of the fMRI preprocessing are provided. Then all the results found in order to select the kinematic regressors are given. Lastly the results of the hemodynamic response selection and of the final Statistical Parametric Maps (SPMs) are illustrated.

In Chapter 7 the conclusions are derived and the future perspectives are given.

Chapter 1

Reach-To-Grasp Movement

This chapter provides an overview on the state of the art of knowledge regarding the reach-to-grasp movement. First, a description of the movement with an evolutionary and developmental contextualization is given. Then results of studies conducted on reaching and grasping are reported, in particular regarding the kinematics of grasping, the neurophysiology in monkeys and the neuroanatomical pathways and neuroimaging in humans. Lastly the advantages of combining different investigation techniques in the study of the reach-to-grasp movement are shown.

1.1 Phases and types of movement

The reach-to-grasp movement is composed by two phases, which partially overlap. The first phase, the *reaching*, consists of the movement of the arm and the hand toward the object and the second phase, the *grasping*, consists of the fingers aperture and the consequent hand contact with the object applying the optimal force in order to maintain the grasp stable. At a certain moment of the movement, there is the separation between the thumb and the other fingers (grip aperture). After that, the hand preshaping occurs, which means that the hand takes the appropriate shape according to the size, the shape and the intended use of the object. At the end of the movement, there is the closure of the fingers (grip closure) until they matched with the object size [1].

There are two different types of grip: the *power grip* and the *precision grip*. The power grip consists of grasping the object with the whole hand instead the precision grip is made by the opposition of the thumb and the forefinger (see Figure 1.1).

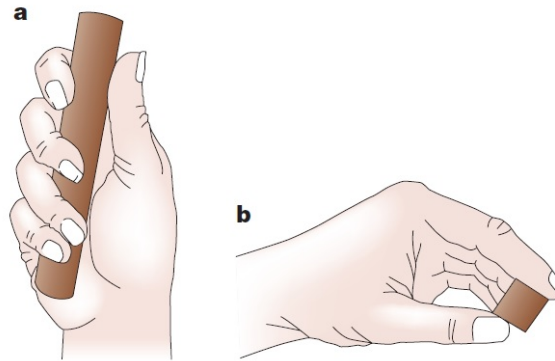


Figure 1.1: Examples of different types of grip. a| Power grip. b| Precision grip. [2]

1.2 Morphological and functional hand evolution

The hand morphology and functionality of the man's ancestors continuously evolved throughout the millenniums in order to be able to perform tasks with increase precision.

The divergent thumb appeared on the pentadactyl hand of the man's first ancestors. The primates became able to grasp and manipulate objects and their ability to actively interact with objects progressively increased [3].

In the more recent man's ape-like ancestors, the reach-to grasp movement skill became more sophisticated thanks to the fingers ability to move independently and to the opposition of the thumb to the forefinger [4].

With bipedalism hands became free and there was a progressive increase of the hands use of tools and consequent precision until the current age [5].

1.3 A developmental view

Strategies adopted to reach towards and grasp objects are very different during different stage of the human development [6]. The precision and the speed of the movement vary significantly during the growth of the child. For example, the opposition of the thumb to the forefinger emerges only at ten months of age [7]. The first attempts to perform a precision grip by young children is usually characterized by excessive force application and large variability. Moreover, the movement is not fluid and seems to be composed by different phases. A skilled manipulation of objects, in order to become efficient, requires a sophisticated control of the finger-tip forces, which is possible using both feedback and feed forward mechanisms [8] [9]. However young children are not able to learn from their previous manipulative experience with objects and cannot optimize the output force performing the following attempts [10]. Only at the age of two years, children become able to calibrate the output force using a feed

forward control [8].

The grasping performance of a child is not comparable to the one of an adult until an age range from six to eight years. Smaller improvements occur also until the adolescence. These findings suggest that grip coordination may coincide with the development and maturation of the neural structure responsible for the control of prehension [11].

1.4 The kinematics of grasping

A significant number of behavioural studies were conducted both with humans and with monkeys in order to understand how the reach-to-grasp movement changes in relation to the object to be grasped. A relevant contribution was given by the kinematic analysis of the movement that is possible using specific systems that can record the movement and extract parameters like the speed and the acceleration of the hand and the fingers. In one of these studies, it has been discovered that the maximum grip aperture is a pretty constant reference point of the grasping movement that can be noticed usually within the 60-70% of the overall reach-to grasp time [12]. Other studies have demonstrated that the type and the precision of the grasping movement is strictly influenced by some objects features: the size, the weight, the texture, the fragility and the contact surface [13]. For example, a small stimulus naturally requires a precision grip and the maximum grip aperture varies linearly with the size of the object [14]. With the small stimulus it can also be noticed an anticipated maximum and a lower grip aperture together with a longer movement duration and a lower amplitude of the peak velocity [15] (see Figure 1.2). However, the chosen grip does not depend exclusively on the visual intrinsic properties of the object but also on the object meaning and on what the agent of the action wants to do with it [16] [17].

Compared with human grasping, little is know about the kinematic characteristics of grasping movements in monkeys [18] [19] [20] [21]. The comparison across species is not easy because it has to be taken into account both morphological and behavioural differences between them [22] [5]. Some studies proposed experiments in which humans performed reach-to-grasp movements in a crouched posture similar to macaques or in which monkeys were forced to sit with an upright posture similar to human [21]. They found out both similar and different features of the monkeys and humans movements. However, this approach would impose movement constraints on the two species that might prevent the investigation of natural grasp kinematics [2].

In general, a large amount of attention has been given to object properties and their influence on kinematics of grasping. Even small differences in object properties can result in a significant change in order to grasp. These results demonstrated how detailed and sensitive

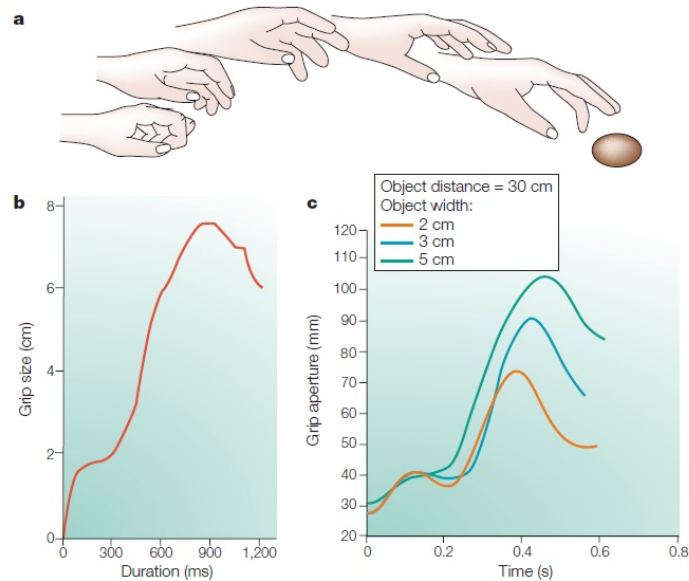


Figure 1.2: Kinematics of grasping. **a**| Hand preshaping during its journey to the target. **b**| Grip aperture during the overall movement. **c**| Representation of traces demonstrating the scaling of maximum grip aperture with respect to object size. [2]

the processes responsible for the "translation" of the object properties into the motor program implemented during the hand preshaping stage are. Recently, great contributions to understand these mechanisms have been provided by studies conducted in neurophysiology domain [23]. Researchers have often presumed that the human brain contains homologies of areas in the macaque brain that are involved in grasping. Although there do seem to be analogies of some such areas, the behavioural differences between species and the methodological differences between studies suggest to treat these homologies with scepticism [2]. In the two following sections, the neurophysiology of monkeys and humans are treated separately.

1.5 Neurophysiology in monkey studies

Most of the studies conducted in monkeys were carried out by registering the activity of single neurons in the cortex of the behaving animal. This method allows a very detailed observation of reach-to-grasp related brain activity of a few neurons in time, with high level of both temporal and spatial resolution. Three specific areas related to grasping have been identified in the monkey cortex [24] [25]:

- Primary motor cortex (F1)
- Ventral and dorsal sectors of the premotor cortex (vPMC and dPMC respectively)
- Anterior intraparietal area (AIP)

Primary Motor Cortex (F1)

The ability to perform a successful grasping action depends primarily on the integrity of the primary motor cortex. It has been shown that lesion of this areas in monkeys produce a remarkable deficit in the control of individual fingers [26]. Information from the primary motor cortex is then conveyed to cells in the spinal cord via the corticospinal tract, a primary neural substrate for independent finger movements [27]. The information sent to the spinal cord from the primary motor cortex is also conveyed to the intermediate zone of the cerebellum. Therefore, it has been proposed that the cerebellum could play a specific role in the control of hand movements during grasping [28] [29].

Another fundamental process for a successful grasp is the visuomotor transformation, that is the transformation of the intrinsic properties of the object, visually described, into motor actions [30]. Two key cortical areas seem to be involved: area F5 and the AIP.

Ventral Premotor Cortex (vPMC)

Area F5 forms the rostral part of the monkey vPMC. Execution of distal motor acts such as grasping, holding, manipulating and tearing is very effective in triggering F5 neuron responses. Interestingly, many hand grasping neurons also show specificity for the type of prehension that is performed to grasp an object. Among these different types of grasp, the precision grip is the most represented type [31]. Therefore, it has been proposed that in area F5 there is a "vocabulary" of elementary motor acts in which each "word" is represented by a population of F5 neurons. These words select specific "motor prototypes", such how the object should be reached, the goal of the action or the temporal segmentation of the action [25].

Anterior Intraparietal Area (AIP)

The AIP is a small zone in the rostral part of the posterior bank of the intraparietal sulcus and is directly connected to the area F5. On the basis of the functional role played by neurons in this area, it has been developed a model in which area AIP provides multiple descriptions of 3D objects in visual terms [32].

Dorsal Premotor Cortex (dPMC)

It has been demonstrated that in the dPMC (also called area F2) there is a distal forelimb representation where there are neurons that are selective for the type of prehension required for grasping an object [24]. The activity of these grasping neurons was not related to individual finger movements but to the grasping action as a whole. It was proposed that area F2 has the role of keep in memory the motor representation of the object and combining it with visual information to continuously update the configuration and orientation of the hand as it

approaches the object to be grasped.

To sum up the vPMC plays a primary role in selecting the most appropriate type of grip on the basis of the 3D object representation provided by AIP to which it is reciprocally connected, thus activating a motor representation of the object. This motor representation is then supplied to the dPMC, which keeps memory of it and combines it with visual information provided by cortical areas of the superior parietal lobe to continuously update the configuration and orientation of the hand as it approaches to the object to be grasped. The final output for action execution most likely involves both vPMC and dPMC. The represented action is initially coded globally and then it is temporally segmented and sent to the hand primary motor cortex (F1) for motor execution (see Figure 1.3) [31].

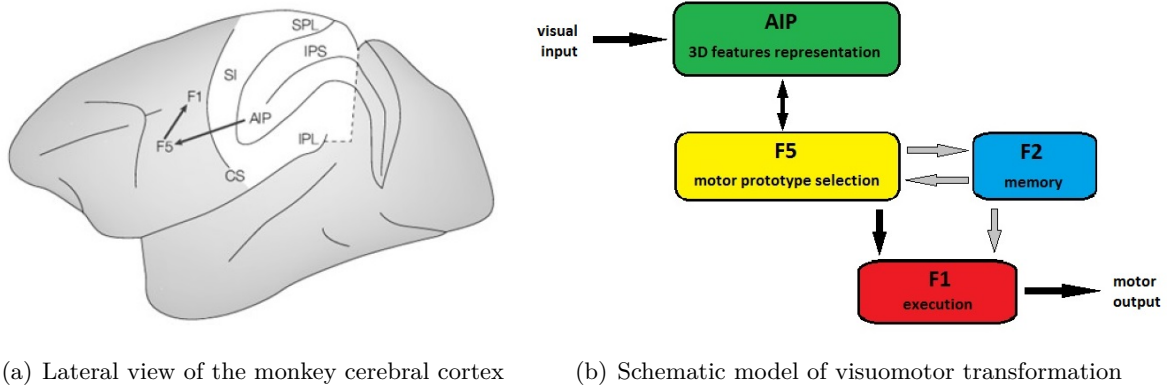


Figure 1.3: The visuomotor grasping circuit in the monkey cerebral cortex. [2]

Like vision, somesthesia is a crucial source of information for the motor system. Somatic receptors in muscles, joints and skin provide information regarding the current posture of the hand and its location and orientation with respect to potential targets for grasping. This information is necessary to compute a trajectory to bring the hand to the object and grasp it properly [2]. For this reason, also the somatosensory cortex (SI) is involved in grasping movements.

Given the wealth of evidence for a grasping circuit involving several areas in the monkey brain, the natural question is whether a similar circuit exists in humans. For ethical reasons, invasive physiological recordings of brain activity is rarely possible in humans. Nonetheless, considerable progress has been made towards understanding the neural substrate of grasping in humans, mainly from neuroimaging experiments [2].

1.6 Neuroanatomical pathways and neuroimaging in human studies

1.6.1 Motor cortical pathways

Human brain controls motor acts through some regions located in the caudal portion of the frontal lobes. This portion of the frontal lobes is called *agranular frontal cortex*, due to the lack of granular cells [33]. The three major areas of the agranular frontal cortex involved in motor control in humans are (see Figure 1.4):

- Primary motor cortex (M1)
- Premotor cortex (PCM)
- Supplementary motor cortex (SMA)

These areas have topographical representation of all the muscle groups of the body. Moreover, other structures like basal ganglia, brain stem and cerebellum are involved.

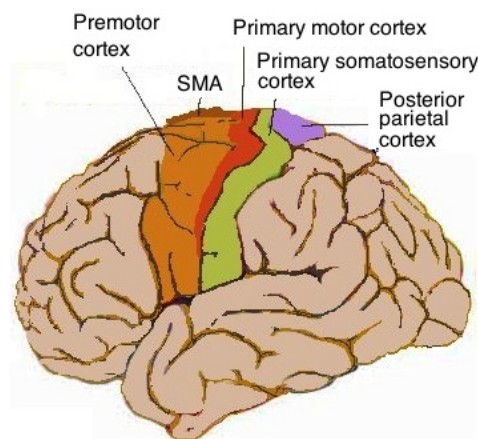


Figure 1.4: Motor cortical areas and somatosensory areas (Source: <http://en.wikipedia.org>).

Primary motor cortex (M1)

The primary motor cortex is a subdivision of the agranular frontal cortex described by Brodmann¹ as area 4 (see Figure 1.5). It is located anteriorly to the central sulcus, beginning laterally in the sylvian fissure and contains a somatotopical representation of the contralateral part of the human body. The representation of the hand is located dorsolaterally, between head and arm representation (see Figure 1.6, left side). Areas of the body that require a greater precision of movement, such as face, thumb, fingers and hand, have larger representation in the primary motor cortex than other body areas like for example limbs and trunk.

¹**Korbinian Brodmann (1868-1918)** was a German neurologist who subdivided the cerebral cortex into 52 distinct regions on the basis of their cytoarchitectonics structure, known as Brodmann areas [34].

Premotor cortex (PMC)

The premotor cortex encompasses Brodmann areas 6, 44 and 45 and lies anterior to M1, extending inferiorly to the sylvian fissure and superiorly into the longitudinal fissure. Its neurons project directly to M1, the red nucleus, the reticular formation, the basal ganglia and, indirectly, to the cerebellum [35]. The PMC can be divided into two subregions: the ventrolateral premotor cortex (vPMC) and the dorsolateral premotor cortex (dPMC). The vPMC seems to be involved in action observation and object manipulation tasks [36] instead the dPMC in action planning, response selection, movement preparation and visual guidance of motor responses [37].

Supplementary motor cortex (SMA)

The supplementary motor cortex is located anteriorly and superiorly to PMC and roughly corresponds to Brodmann area 6. It can be divided into two subregions: the proper SMA and the pre-SMA. The proper SMA appears to be involved in simple, externally triggered and well practiced motor tasks [38] instead the pre-SMA in more cognitive tasks, such as processing of cues rather than response selection [39].

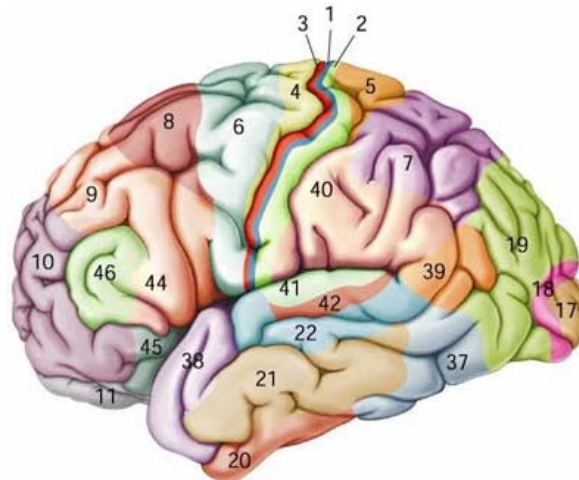


Figure 1.5: Brodmann areas (Source: <http://mybrainnotes.com>).

1.6.2 Somatosensory pathways

Somatosensation consists of touch proprioception, thermal sensation and pain. The inputs forming the basis for these sensations are collected from skin, joints, muscles and subcutaneous tissue. Like motor areas, also somatosensory areas have somatotopical organization, showing larger representations for areas densely innervated, like lips and fingertips (see Figure 1.6, right side). Three major areas are involved in the somatosensory pathway (see Figure 1.4):

- Primary somatosensory cortex (SI)
- Secondary somatosensory cortex (SII)
- Posterior parietal cortex (PCC)

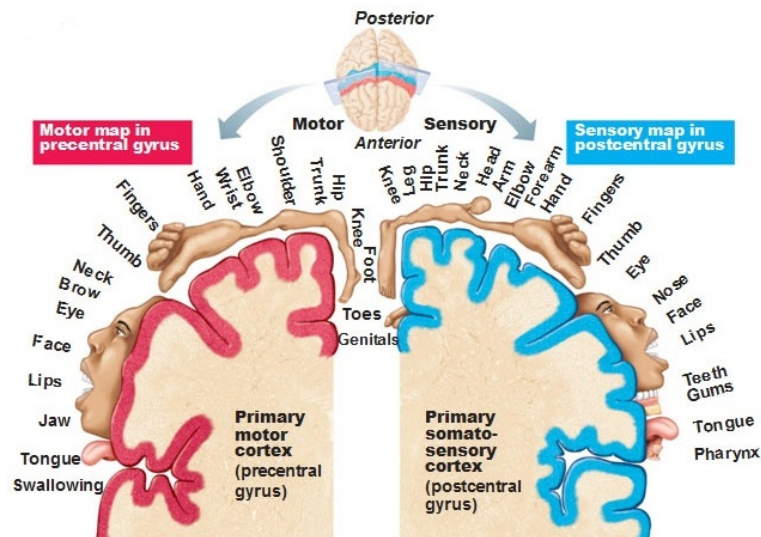


Figure 1.6: Motor homunculus (left side) and sensory homunculus (right side) (Source: <http://antranik.org>).

Primary somatosensory cortex (SI)

The primary somatosensory cortex is located in the posterior bank of the central sulcus in the post-central gyrus and is described by Brodmann areas 1, 2 and 3. It is specialized in processing informations coming from mechanoreceptors of the skin and in proprioception.

Secondary somatosensory cortex (SII)

The secondary somatosensory cortex lies in the upper bank of the sylvian fissure. Informations arrive to SII from both sides of the body, via thalamus, SI and also through other sensory areas, like visual and auditory cortices.

Posterior parietal cortex (PCC)

The posterior parietal cortex is located in the parietal lobe and encompasses Brodmann areas 5, 7 and 40. It is implicated in integration of informations coming from different sensory modalities. It has been demonstrated that a particular region of the PPC, the anterior intra-parietal sulcus (aIPS), plays a key role in the context of grasping movements, in particular in the hand shaping stage.

1.6.3 Subcortical pathways

The *corticospinal tract* is the most important pathway from M1 to periphery. Its neurons originate mostly from M1, PMC and SMA: the axons from cortex pass through the internal capsule and then downward through the brain stem and the medulla, where most of the fibers decussate to the opposite side. The fibers then descend in the lateral tract and project to interneurons of the intermediate region of the cord gray matter and form the lateral tract. Some of the fibers do not cross the medulla and form the ventral tract. The corticospinal tract is crucial for discrete and fine tuned movements, especially those including hands and fingers [33].

Also *basal ganglia* are involved in motor control. They receive inputs from somatosensory and motor cortices and are involved in the maintenance of muscle tone [40].

The *thalamus*, acting as relay, transmits information from basal ganglia and cerebellum to the motor cortex [41].

The *cerebellum* seems to be significantly implicated in motor learning [42]. It receives input from the spinocerebellar tract, conveying informations from muscle, joints, cutaneous receptors and spinal interneurons.

1.6.4 Neuroimaging studies using fMRI technique

Brain imaging experiments investigating neural substrates of grasping in humans usually take result obtain from neurophysiology as a reference point. Several studies conducted using fMRI (see Chapter 2) have focused on selected neuroanatomical regions, presumably the hypothetical human homologue of monkey AIP. In these experiments, subjects are scanned during either reach-to-grasp actions or only grasping actions using in general their (dominant) right hand [2].

In one of these studies [43] a comparison between grasping movement and pointing movement towards the same object was performed. The results showed a specific activation of AIP for the grasping task and also activations in the contralateral sensorimotor cortex, in bilateral PMC and in the PPC. The portion of AIP activated by the grasping task appears to be the homologue of AIP area in the monkey. This result was further confirmed by studies that used a region of interest (ROI) approach and an event-related design [44] [45] in which participants, lying in the MR scanner, had to reach towards objects and grasp them using a precision grip. The results provided clear evidence that AIP contributes to the ability to perform grasping actions towards objects.

In another study [46] it has been looked in humans for a neural network underlying grasping similar to those detected in area F5 of macaques. Two objects were used: one of these was a large object that would normally be grasped with a power grip, the other one was small and would normally be grasped by a precision grip. The activated areas were consistent

with the monkey AIP-F5 visuomotor circuit.

A more recent study [47] considered different type of prehension movement and different type of stimuli. Results indicated that the left aIPS was active when the subjects naturally adopted a precision grip to grasp the small object. Moreover, another related study [48] paid particular attention to the dorsolateral and dorsomedial network. Results showed that the aIPS was more active using a precision grip than using a power grip, independently of stimulus size. Conversely, the activities of both dPMC and M1 were modulated by the relationship between the type of grasp that was adopted and the size of the stimulus.

Other issues involved in grasping are related to force production for specific grasping patterns. Concerning this matter, a study [49] compared human brain activity during a precision grip and a power grip. Results showed that precision grip task involved extensive activation in both hemispheres and that, in addition to M1, also premotor and parietal areas are important for control of fingertip forces during a precision grip.

In another fMRI study [50] the human neural substrates of the transport component and its relationship with the grip component was examined. It has been found specialization for the grip component in bilateral aIPS and left vPMC and it has been postulated that the dPMC and the SMA are important in the coordination of the reach-to-grasp movement. In either species, human and macaques, the AIP is thought to be specialized for hand grip, whereas the superior parietal-occipital cortex and medial intraparietal cortex are specialized for arm transport. These areas then project to the vPMC and dPMC.

Other studies focused on the neural network responsible in planning and online control of reach-to-grasp movement. One of these [51] identified two large, independent networks of brain activity: a planning network (including PMC, basal ganglia, anterior cingulate, posterior medial parietal area, superior parietal occipital cortex and middle intraparietal sulcus) and a control network (including sensorimotor cortex, the cerebellum, the supramarginal gyrus and the superior parietal lobule). A different study [52] found also that, in contrast to the macaque monkey, grasp- and reach-specific activations were largely located outside of the human aIPS.

Lastly, some studies also tested the role of subcortical structures involved in reach to grasp movement execution. In this respect, basal ganglia have to be considered as another important system that could possibly play a role in grasp selection or movement execution planning, or even related to the online control of force or force pulses during movement [53]. Related experimental findings have identified the basal ganglia and also the cerebellum as complementary actors in regulation of ongoing actions when precise updating is required [54].

To sum up, these studies suggest that in humans, like in monkeys, reach to grasp movements involve a large network of interconnected structures in the parietal and frontal lobes. Moreover, this cortical network is differentially involved for the control of distinct aspects characterizing the planning and the control of reach-to-grasp movement. Nevertheless, how

the neural control systems interact with the complex biomechanics of moving arms remains an open question.

1.7 Combining different techniques: fMRI and kinematic data

A powerful method to investigate how the kinematic of the moving arm influences the neural network during the reach-to-grasp movement is to combine different recording techniques together. It is only through the use of converging techniques with different characteristics that how the human brain controls the grasping function might be fully understood [31]. What is so far lacking in the literature on cortical control of grasp in humans is a systematic documentation of the time course of neural activity and kinematical signals during the grasping movement. A recent study [55] co-registered kinematics and evoked related potentials (ERPs) in order to provide deeper insights into the neuro-functional basis of grasping in humans.

The goal to capture the complex natural cerebral activity requires a multimodal approach which take benefits from all the different techniques used. The simultaneous recording of the BOLD signal and the kinematic data allows to exploit the technical advantages of both the investigation methods. In particular, kinematic data become useful in order to compensate the low temporal resolution of the MR images.

Chapter 2

Functional Magnetic Resonance Imaging

In this chapter¹ the basic theory of fMRI technique is provided. In the first part, a brief overview on the MRI scanner, the physics of MR signal generation and BOLD signal are given. In the last part, the general steps of a standard fMRI experiment conduction are reported, from the experimental design to the statistical data analysis.

2.1 Introduction

Magnetic Resonance Imaging (MRI) is a non-invasive technique that uses strong magnetic fields to create images of biological tissue. The image creation is possible thanks to an appropriate MRI scanner that produces a static magnetic field and uses a series of changing electromagnetic gradients and oscillating electromagnetic fields. Depending on particular properties of the hydrogen nuclei, the MRI scanner can distinguish among different tissue types. The ability to examine multiple biologically interesting properties of tissues makes MRI an extraordinary flexible and powerful clinical tool. For example, it is possible to create images sensitive to tumors, abnormalities in blood vessels, lesions and many other conditions.

While much knowledge about the brain has come from the study of its structure, structural studies are lacking in revealing short-term physiological changes associated with the active function of the brain. To understand the working of the human brain, functional neuroimaging studies are necessary. Functional neuroimaging attempts to localize different mental processes to different parts of the brain, in effect creating a map of which areas are responsible for which processes. With Functional Magnetic Resonance Imaging (fMRI), a particular MRI technique, it is possible to provide this kind of information. Most fMRI stud-

¹This chapter is mainly based on [56].

ies measure changes in blood oxygenation over time without using any tracer. Because of the rapid changes in blood oxygenation levels following activity of neurons in a brain region, fMRI allows brain activity localizations on a second-by-second basis and within millimeters of its origin. Because of these advantages, fMRI has been adopted as a primary investigative tool by thousands of researchers.

Despite its broad use, fMRI is a quite recent technique. Basic physics work in the 1920s to 1940s set forth the idea that atomic nuclei have magnetic properties and that these properties can be manipulated experimentally. In 1946 the phenomenon of Nuclear Magnetic Resonance (NMR) was discovered and the first biological MR images were created in the 1970s. By the 1980s, MR imaging became clinically prevalent and in the early 1990s the discovery that changes in blood oxygenation could be measured by MRI ushered in a new era of functional studies of the brain. In little more than a decade, fMRI has grown to become the dominant technique in cognitive neuroscience.

2.2 MRI scanner

The three main components of an MRI scanner which together allow collection of images are:

- Static magnetic field
- Radiofrequency coils
- Gradient coils

There are also other necessary components in a MRI scanner such as shimming coils, specialized computer system and physiological monitoring equipment (see Figure 2.1).



Figure 2.1: MRI scanner. [57]

Static magnetic field

The static magnetic field is an absolute necessity for MRI to induce changes in proton spin. Modern MRI scanners use superconducting electromagnets that provide homogeneous and stable field strengths in the range of 1 to 9 T for human use. The static fields used in MRI are always active, even when no image are being collected.

Radiofrequency coils

While a strong static magnetic field is needed for MRI, the static field itself does not produce any MR signal. MR signal is actually produced by the clever use of two types of electromagnetic coils, known as transmitter and receiver coils, that generate and receive electromagnetic fields at the resonant frequency of the atomic nuclei within the static magnetic field. Such these fields are much less strong (~ 50 mT) than the main magnetic one (some T). Because most atomic nuclei of interest for MRI studies have their resonant frequency in the radiofrequency portion of the electromagnetic spectrum, these coils are also called radiofrequency coils. Unlike the static magnetic field, the radiofrequency fields are turned on and off during small portions of the image acquisition process and remain off for any other period.

In the case of fMRI, the radiofrequency coils are typically placed immediately around the head, either in a surface coil or volume coils arrangement (see Figure 2.2).

Gradients coils

The combination of a static magnetic field and a radiofrequency coil allows detection of MR signal, but MR signal alone cannot be used to create an image. The fundamental measurement in MRI is merely the amount of current through a coil, which itself has no spatial information. By introducing magnetic gradients superimposed upon the strong static magnetic field, gradient coils provide the final component necessary for imaging. The gradient coil causes the the MR signal to become spatially dependent in a controlled fashion, so that different locations in space contribute differently to the measured signal over time. Gradient coils are used to generate a magnetic field that increases in strength over one spatial direction with z direction going parallel to the main magnetic field and x and y directions going perpendicularly to it (see Figure 2.3). Similar to the radiofrequency coils, the gradient coils are only used during image acquisition.

Shimming coils

Ideally the main magnet would be perfectly homogeneous and the gradient coils would be perfectly linear, but it is hardly the case in reality. Shimming coils are able to generate high-order compensatory magnetic fields that correct for the inhomogeneity of the magnetic field.



Figure 2.2: Volume coils. [56]

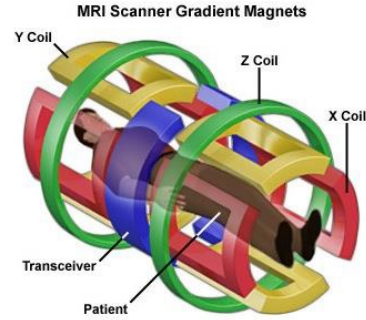


Figure 2.3: Gradient coils. [57]

2.3 Bases of MR signal generation

All magnetic resonance imaging, including fMRI, relies on a core set of physical principles. These principles were discovered by Rabi, Bloch, Purcell and other pioneers during the first half of the 20th century, and they form the basis for the detection of signal based on magnetic properties of atomic nuclei.

The most commonly imaged nucleus used in MRI is the *hydrogen nucleus* because it is the most abundant in the human body. It has a single proton and it is characterized by a specific *magnetic moment* (μ) and *angular momentum* (\mathbf{J}). Because of these properties, the hydrogen nucleus is useful for MRI and it is said to possess the nuclear magnetic resonance property.

$$\mu = \gamma \mathbf{J} \quad \gamma : \text{gyromagnetic ratio} \quad (2.1)$$

However, in the absence of any strong magnetic field, the spins of the hydrogen protons are oriented randomly (see Figure 2.4) and tend to cancel each other out. Thus, the sum of all magnetic moments from spins of different orientation, or *net magnetization* (\mathbf{M}), is infinitesimally small under normal conditions. To increase the net magnetization of the protons, a strong magnetic field must be applied.

2.3.1 Equilibrium condition

When protons are placed within a strong external magnetic field (\mathbf{B}_0), they change their orientation. Instead of turning to align with the magnetic field, the spinning protons initiate a gyroscopic motion known as *precession* (see Figure 2.5). This happens because spinning objects respond to applied forces by moving their axes in a direction perpendicular to the

applied force. The angular velocity is determined by the Larmor frequency:

$$\omega_0 = \gamma \mathbf{B}_0 \quad (2.2)$$

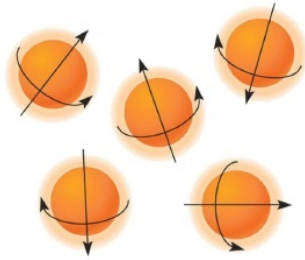


Figure 2.4: Random spin orientation. [56]

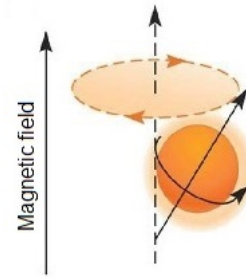


Figure 2.5: Spin precession. [56]

There are two states for precessing protons: one parallel to the magnetic field and the other anti-parallel (see Figure 2.6). Protons in the parallel state have a lower energy level, while protons in the anti-parallel state have a higher energy level. The parallel state is slightly more stable, so there will always be more protons in the parallel state than in the anti-parallel state, with the relative proportion of the two states dependent on temperature and strength of the magnetic field.

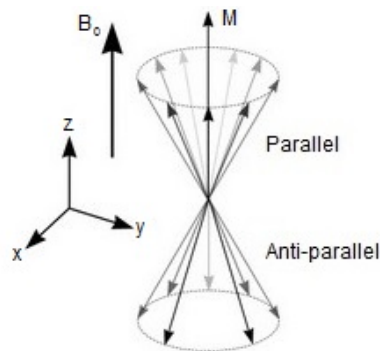


Figure 2.6: Net magnetization (Source: <http://wiki.umn.edu>).

It is important to underline that MR techniques do not measure single nuclei, but instead measure the net magnetization of all spins in a volume. The net magnetization can be divided into two components: a *longitudinal component* M_z that is either parallel or anti-parallel to the magnetic field and a *transverse component* M_{xy} that is perpendicular to the magnetic field. It should be noticed that under equilibrium conditions (i.e. without any perturbation):

- M_z depends on the difference in the number of the spins in the parallel and anti-parallel states

- M_{xy} will tend to cancel out because of the enormous number of spins within even the smallest volume, meaning that there is no net magnetization perpendicular to the main magnetic field

However, net magnetization itself cannot be measured directly under equilibrium conditions. A perturbation of the equilibrium state of the spins is needed in order to provide information about the net magnetization of a spin system.

2.3.2 Spin excitation

Radiofrequency coils within MRI scanners bombard spins in the magnetic field with photons in order to transfer them energy that allow some spins in the low-energy state to jump to the high-energy state. This process is called *excitation* and the portion of energy absorbed by each spin that changes level is equal to the energy difference between the two states. The frequency of the electromagnetic radiation that is needed to make spins change from one state to another is equal to the Larmor frequency (see Equation 2.2) and corresponds to the resonant frequency of the nucleus of interest. This principle represents the key concept of the magnetic resonance phenomenon.

The perturbation is thus caused by specialized radiofrequency coils that transmit an electromagnetic excitation pulse (\mathbf{B}_1) at the same frequency as the spin precession and along a perpendicular direction respect to the main magnetic field. The excitation pulse induces a rotation of the net magnetization vector that spirals down around the main field vector towards the XY plane (see Figure 2.7). The angle θ around which the net magnetization rotates is determined by the duration T of the applied electromagnetic pulse:

$$\theta = \gamma \mathbf{B}_1 T \quad (2.3)$$

This equation determines how long should be the duration of the electromagnetic pulse to change the net magnetization vector by an angle θ , called the *flip angle*. Usually, the excitation pulse should be presented for a brief period, on the order of milliseconds.

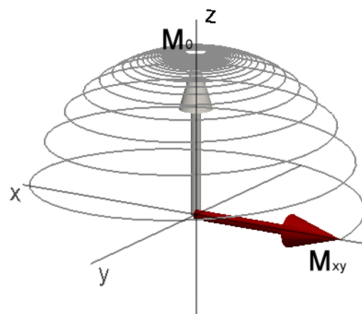


Figure 2.7: Spiral path of the net magnetization (Source: <http://fmrib.ox.ac.uk>).

Under this perturbed condition, if $\theta = 90^\circ$:

- M_z is equal to zero because the number of spins in the parallel state is equal to the number of the spins in the anti-parallel state
- M_{xy} is positive because the spins tilted down on the XY plane are all in phase

It is important to remember that when the net magnetization is entirely in the longitudinal direction it does not change over time and thus it is not measurable. Instead, if it is tipped into the XY plane with an excitation pulse, there will be very large changes in the direction of magnetization over time as it rotates. In this way, a measurable MR signal is created and can be detected by the receiver coils.

2.3.3 Spin relaxation

The MR signal created following an excitation pulse does not last indefinitely. When the excitation pulse is taken away, the signal decays over time, usually within few seconds, because the spins system gradually loses the energy absorbed during excitation. This phenomenon is called *spin relaxation*. Two primary mechanisms contribute to the loss of the MR signal: the *longitudinal relaxation* and the *transverse relaxation*.

Longitudinal relaxation

The longitudinal relaxation takes place because the excited spins in the high-energy state gradually go back to their original low-energy state. The consequence is that the transverse magnetization likewise returns back to the longitudinal direction, as it was before the excitation pulse. The time constant associated with this process is called $T1$ and the relaxation process is called $T1$ recovery (see Figure 2.8). If M_0 is the original magnetization, the amount of longitudinal magnetization present at time t following an excitation pulse is given by:

$$M_z = M_0(1 - e^{-\frac{t}{T_1}}) \quad (2.4)$$

Transverse relaxation

The transverse relaxation takes place because the coherence between the spins is gradually lost resulting in a progressive dephasing. For this reason, the transverse magnetization becomes smaller over time. The time constant associated with this process is called $T2$ and the relaxation process is called $T2$ decay (see Figure 2.8). The amount of transverse magnetization present at time t following an excitation pulse is given by:

$$M_{xy} = M_0 e^{-\frac{t}{T_2}} \quad (2.5)$$

However, another additional source of signal loss has to be considered, that is the inhomogeneity of the main magnetic field. This fact, together with the spins dephasing, causes a

relaxation process actually characterized by the time constant $T2^*$ and called $T2^*$ decay. The constant $T2^*$ is much more smaller than the constant $T2$ and thus the decay is in reality faster.

$$\frac{1}{T2^*} = \frac{1}{T2} + \gamma \frac{\Delta B_0}{2} \quad \Delta B_0 : \max B_0 \text{ inhomogeneity} \quad (2.6)$$

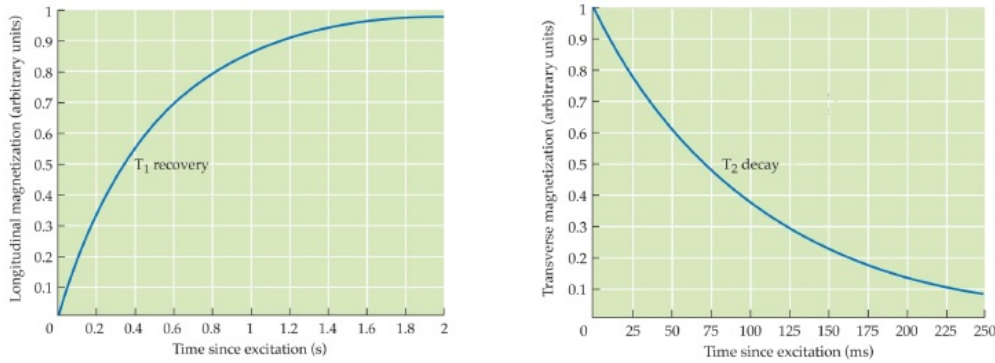


Figure 2.8: Longitudinal (left side) and transverse (right side) relaxation. [57]

These relaxation processes constrain how much MR signal can be acquired following a single excitation pulse. The versatility of MRI as an imaging tool results from its sensitivity to different relaxation properties of tissues. In Table 2.1 are collected some examples of $T1$ and $T2$ values regarding the white matter, the grey matter and the cerebrospinal fluid at 1.5 T field strength.

	White Matter	Grey Matter	Cerebrospinal Fluid
$T1$	600 ms	900 ms	4000 ms
$T2$	80 ms	100 ms	2000 ms

Table 2.1: $T1$ and $T2$ values at 1.5 T field strength.

2.4 BOLD signal

In 1936, Linus Pauling and his student Charles Coryell discovered a remarkable fact of nature: the hemoglobin molecule has magnetic properties that differ depending upon whether or not it is bound to oxygen. In particular, they found that the oxygenated hemoglobin (Hb) is *diamagnetic*, i.e. it has a zero magnetic moment, and in contrast, that the deoxygenated hemoglobin (dHb) is *paramagnetic*, i.e. it has a significant magnetic moment. Completely deoxygenated blood has therefore a *magnetic susceptibility* about 20% greater than fully oxygenated blood.

Introducing an object with magnetic susceptibility into a magnetic field causes spin dephasing, resulting in a decay of transverse magnetization that depends on the time constant $T2^*$. Consequently, using a specific MR pulse sequence, more MR signal should be seen

where blood is highly oxygenated and less MR signal where blood is highly deoxygenated. This prediction was verified experimentally in the early 1980s by Thulborn and colleagues, who demonstrated that the decay of transverse magnetization depends on the proportion of oxygenated hemoglobin. In particular, they shown that the value $1/T_2$ decreases with increasing oxygenation (i.e. the more oxygenated hemoglobin that is present, the shorter the T_2) and that the value $1/T_1$ is not affected by blood oxygenation level (see Figure 2.9). Moreover, they noted also that the magnitude of this effect increases with the square of the strength of the static magnetic field. At low field strength (i.e. less than 1.5 T), there is little difference between the transverse relaxation time for oxygenated and deoxygenated blood, but in higher field (i.e. 1.5 T or greater), their values differs significantly.

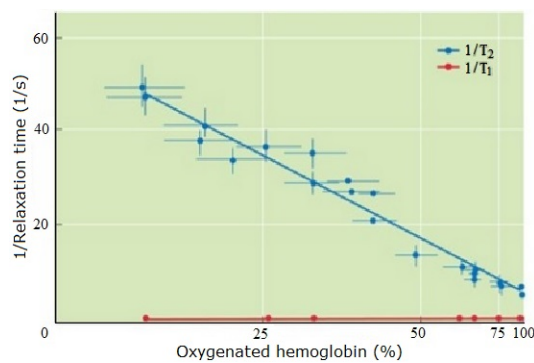


Figure 2.9: Effects of blood deoxygenation upon MR relaxation constants. [56]

2.4.1 BOLD contrast

During the late 1980s, Seiji Ogawa, a research scientist at Bell Laboratories, investigated the possibility of examining brain physiology using MRI. Based on the previous finding that deoxygenation decrease the T_2^* value of blood, Ogawa hypothesized that the proportion of blood oxygen would affect the visibility of blood vessels on T_2^* -weighted images. The difference in signal as a function of the amount of deoxygenated hemoglobin was called *Blood-Oxygenation-Level Dependent (BOLD) contrast*. Ogawa conducted his experiments according to the hypothesis that BOLD contrast would enable measurement of functional changes in brain activity. His results shown that BOLD contrast depended upon the total amount of deoxygenated hemoglobin present in a brain region, which in turn depended upon the balance between oxygen consumption and oxygen supply. Although it seems reasonable that increased neuronal activity would result in increased oxygen consumption and thus greater decrease in MR signal, as Ogawa originally hypothesized, experimental observations of the brain during increased neuronal activity shown that there is an *increase* in the MR signal. To explain this effect, the relation among cerebral blood flow, blood oxygenation level and metabolism has to be taken into account.

After the stimulus presentation, the metabolic demands of increased neuronal activity result in oxygen consumption and in an increased inflow of oxygenated blood. However, more oxygen is supplied to the brain area than is extracted, and this leads to an impairment between oxygenated and deoxygenated hemoglobin with a relative decrease of deoxygenated hemoglobin. For this reasons, an increased MR signal can be measured during neuronal activity in respect to the baseline condition (see Figure 2.10).

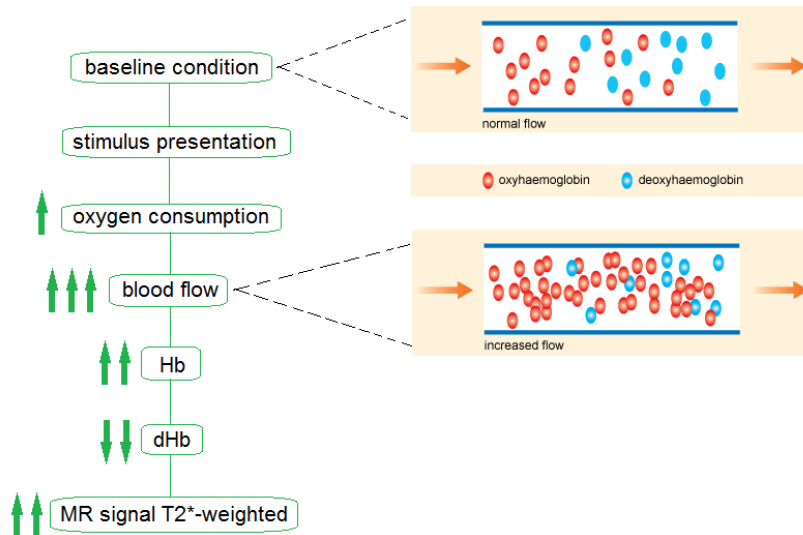


Figure 2.10: Sequence of events after stimulus presentation.

2.4.2 Hemodynamic response

The change in the MR signal triggered by neuronal activity is known as the *hemodynamic response (HDR)*. The shape of the HDR varies with the properties of the evoking stimulus and, presumably, with the underlying neuronal activity. It should be reasonable to expect that increasing the rate of neuronal firing would increase HDR amplitude, whereas increasing the duration of neuronal activity would increase HDR width. Determining the exact relation between the neuronal events that trigger the HDR and the shape of HDR, however, is complicated by their differing dynamics (see Figure 2.11).

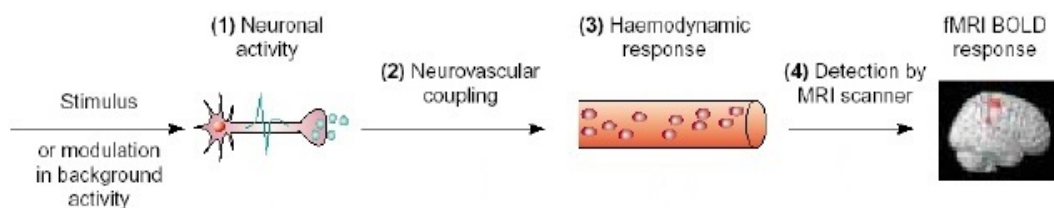


Figure 2.11: Neuronal events that trigger the HDR and cause the fMRI BOLD response. [58]

Cortical neurons responses occur within tens of milliseconds following a sensory stimulus, but the first observable HDR changes do not occur until 1 or 2 seconds later. At that point, the positive change of the MR signal is preceded by a smaller decrease, called *initial dip*. It may result from initial oxygen extraction before the later overcompensatory response. Then, due to the increased cerebral blood flow and volume, the MR signal grows until reaching its maximum, producing an *overshoot*. If neuronal activity is extended across a block of time, the peak may be similarly extended into a plateau. After that, the BOLD signal decreases in amplitude to a below-baseline level producing a post-stimulus *undershoot* (see Figure 2.12).

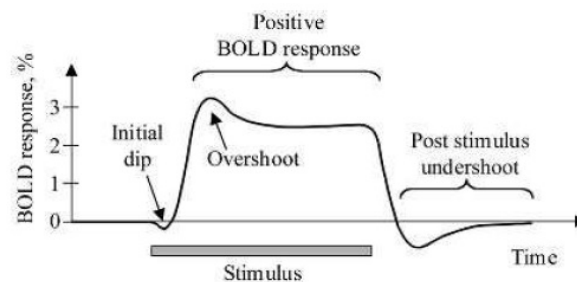


Figure 2.12: Hemodynamic response. [57]

To understand the reason of the undershoot, the changes in cerebral blood flow and cerebral blood volume has to be considered separately. Following cessation of neuronal activity, blood flow decreases more rapidly than blood volume. Thus, a greater amount of deoxygenated hemoglobin is present and the overall fMRI signal is reduced below baseline level. As blood volume slowly returns to normal levels, the fMRI signal will similarly increase to baseline, ending the undershoot (see Fig. 2.13).

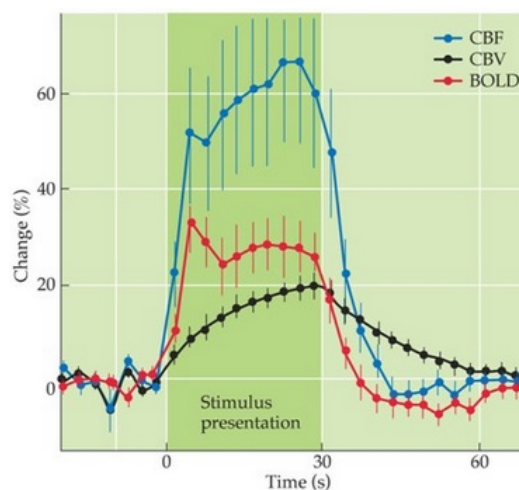


Figure 2.13: Relative changes in cerebral blood flow (CBF) and cerebral blood volume (CBV) following neuronal activity. [56]

2.5 Experimental design

One of the most important issue in fMRI experiments is to set up an adequate experimental design in order to test a research hypothesis. Every research hypothesis, that is a proposition about the nature of the world that makes predictions about the results of an experiment, has to be verified by measuring the outcomes of a peculiar experiment. In modern fMRI experiments, scientists often manipulate some aspects of a stimulus and then measure the change in BOLD signal within the brain. In this way it is possible to identify hemodynamic and neuronal activities in specific areas of the brain and derive conclusions on its functionality.

The experimental design has to be as more efficient as possible in order to answer meaningful question about the world. When selecting conditions for an experiment, it is important to avoid confounding factors, or variables that unintentionally covary with the variable of interest. A well-designed experiment has to test specific hypotheses, to rule out alternative explanations of the data and to minimize the cost of running experiment. Advance planning to ensure good experimental design is especially important for fMRI experiments, given the significant resources they require in terms of money, time and energy.

In fMRI studies, there is no optimal experimental design. The fundamental rule when designing a study is to choose the design that best suits the experimental question. There are two main types of fMRI experimental design: *blocked design* and *event-related design*.

Blocked design

In a blocked design, each condition is presented continuously for an extended time interval and the different conditions are usually alternated over time (see Figure 2.14). It is possible to compare two or more different *task conditions* or compare a task condition with a *control* or *rest condition*. The best block length and timing have to be chosen according to the kind of task and the research hypothesis.

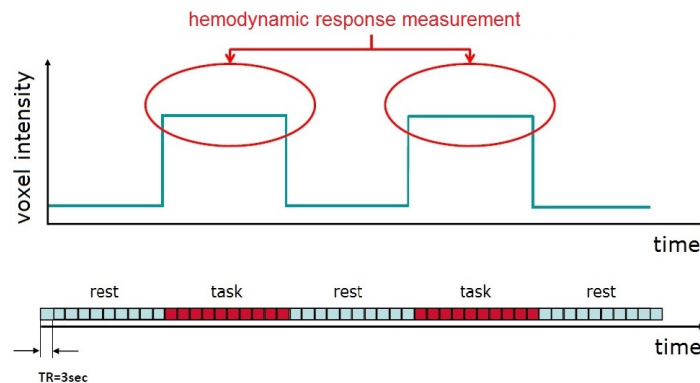


Figure 2.14: Blocked experimental design. [59]

Event-related design

Event-related design presents stimuli one at a time rather than together in a block. Each stimulus is separated in time from the previous one with an *interstimulus interval (ISI)* that has a different value depending on the goal of the experiment. The different conditions are usually presented in a random order rather than an alternating pattern (see Figure 2.15).

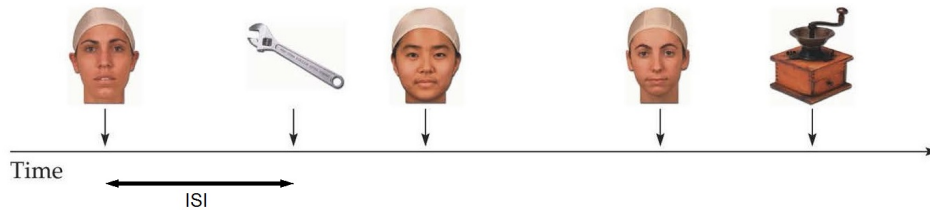


Figure 2.15: Event-related experimental design. [59]

Both the designs have advantages and disadvantages (see Table 2.2). In general, the strengths of blocked designs mirror the weaknesses of event-related designs, and vice versa.

	Advantages	Disadvantages
Blocked design	High detection power Simple analysis	Poor estimation power Insensitive to the shape of HDR Sensitive to the movement Potential problems with selection of conditions
Event-related design	Good estimation power Flexibility	ISI dependent Low SNR

Table 2.2: Advantages and disadvantages of blocked and event-related designs.

It is also important to underline that the experimental design influences the shape of the hemodynamic response. In particular, with a block of multiple consecutive stimuli, the HDR does not have time, after its peak, to return at its baseline and thus presents a plateau (see Figure 2.16).

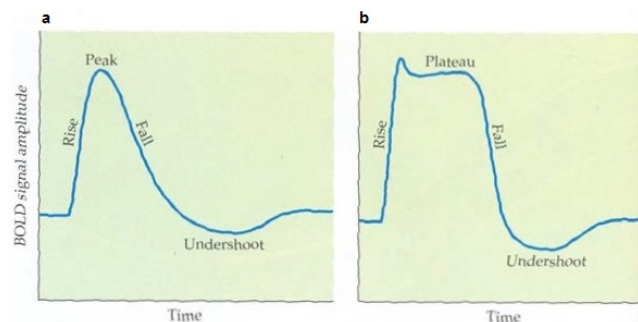


Figure 2.16: Schematic representations of the fMRI BOLD hemodynamic response. **a**| HDR to a single short-duration stimulus. **b**| HDR to a block of multiple consecutive stimuli. [56]

2.6 fMRI data preprocessing

All fMRI data suffer from spatial and temporal inaccuracy caused by many factors such as subject head motion, physiological oscillations, inhomogeneities of the static field and differences in the timing of image acquisition. If uncorrected, this variability may reduce or even eliminate the detection power of an experiment. To solve this problem, a series of computational procedures, known as data preprocessing steps, are necessary before performing every statistical analysis. Preprocessing is fundamental to reduce variability in the data that is not associated with the experimental task and to prepare the data for statistical testing. The most common preprocessing steps are:

- Slice timing correction
- Motion correction
- Coregistration
- Normalization
- Spatial smoothing

2.6.1 Slice timing correction

Most fMRI scanners acquire images one slice at a time, due to the use of spatial gradients that limit the influence of an excitation pulse to a single slice within the brain. For this reason, for each slice, the measured time course will have a particular sampling delay, which can greatly influence the correspondence between observed data and experimental hypotheses. The consequences of slice timing errors are much greater for event-related designs than for blocked designs and for long TRs than for short TRs.

Slice timing correction consists of modifying the predicted hemodynamic responses so that each slice is compared to a hemodynamic response function with slightly different timing. One of the most common method to correct for slice timing errors is temporal interpolation which uses information from nearby time points to estimate the amplitude of the MR signal at the onset of the TR (see Figure 2.17).

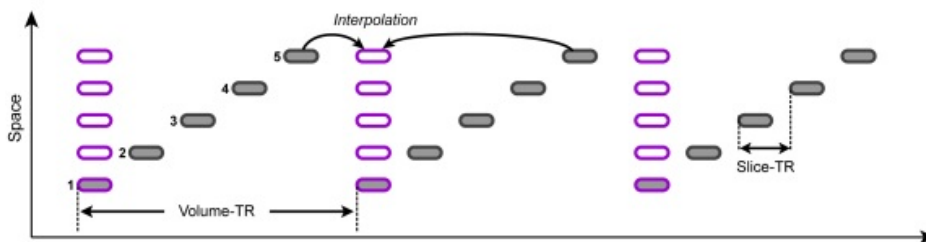


Figure 2.17: Interpolation to correct slice timing errors (Source: <http://brainvoyager.com>).

Several strategies for interpolation are used in fMRI, including linear, spline and sinc functions. The accuracy of interpolation depends on two factors: the variability in the experimental data and the sampling rate. If the experimental data change very rapidly over time compared to the sampling rate, then interpolation will not be able to capture changes between data points. On the contrary, if the data change very slowly compared to the sampling rate, the interpolation will be more effective.

2.6.2 Motion correction

One of the most damaging problem for fMRI studies is subject head motion. Even tiny movements have drastic effects upon the data and can cause irreversible loss of data.

Like many other problems, head motion prevention is easier to apply than head motion correction. Many laboratories use head restraints of some forms such as bite bars, masks and vacuum packs (see Figure 2.18). Another adoptable easy trick is partitioning the fMRI experiments into a number of relatively short runs to reduce subject fatigue and therefore head motion.

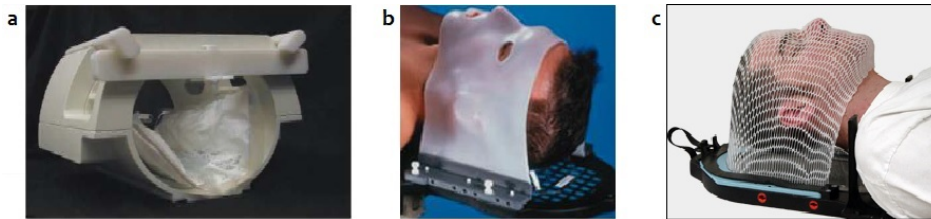


Figure 2.18: Head restraint systems. a) Volume head coil with a bite bar system and a vacuum pack [56]. b) Thermoplastic mask [56]. c) Immobilization mask (Source: <http://cdrsys.ca>).

However it is not always possible to prevent subject head motion and for this reason motion correction algorithms are necessary. The purpose of motion correction is to adjust the time series of images so that the brain is in the same position in every image. Successive image volumes in the time series are coregistered to a single reference volume. It is possible to use a rigid-body transformation because the brain is the same in every image of the time series. Rigid-body transformations in fact assume that the size and the shape of the two objects to be coregistered are identical, and that one can be superimposed exactly upon the other by a combination of three translations and three rotations. Computer algorithms identify the set of translation and rotation parameters that provides the best match to a reference volume, such as the first volume acquired in the session, minimizing a cost function (see Figure 2.19 and Figure 2.20).

Once a set of realignment parameters is determined, it is necessary to resample the original data to estimate the values that would have been obtained without head motion. This procedure is called spatial interpolation and can be implemented by linear methods or by more complex algorithms such as spline or sinc interpolation.

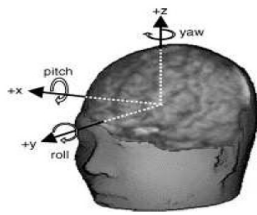


Figure 2.19: Head rotations. [60]

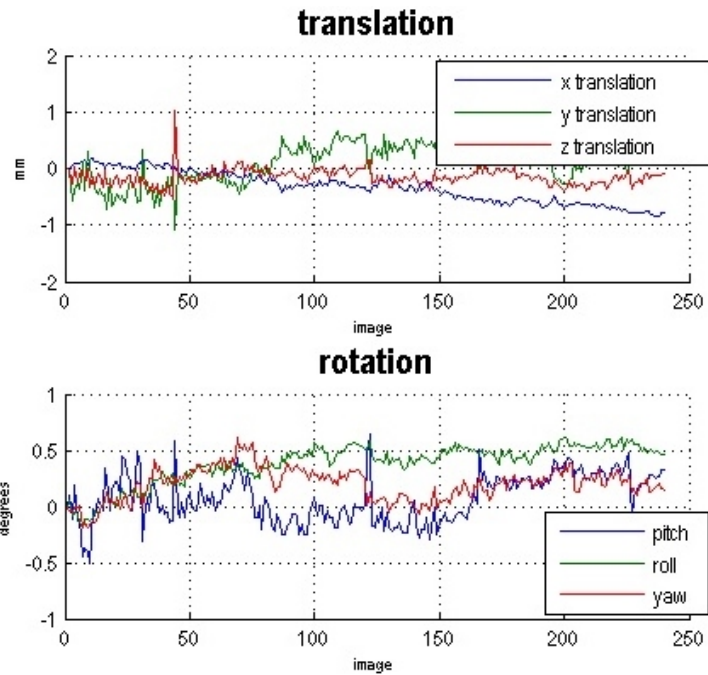


Figure 2.20: Plots of head motion over an experimental session. [56]

2.6.3 Coregistration

In general, fMRI data have low spatial resolution and little anatomical contrast together with geometric and intensity distortions. Due to these problems, it is really hard to find a correspondence between the functional data and the underlying neuroanatomy. In order to facilitate this procedure, coregistration algorithms are necessary. The goal of coregistration steps is to map the functional data onto high-resolution and high-contrast structural images from the same subject. In fact, structural T1-weighted data have much higher resolution than functional data (usually, $1 \times 1 \times 1$ mm and $3 \times 3 \times 3$ mm of voxel size respectively, see Figure 2.21). After coregistration is therefore possible to identify with much more precision different regions of the brain.

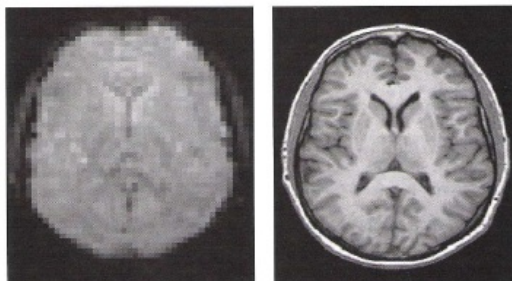


Figure 2.21: Functional (left side) and structural (right side) images. [56]

2.6.4 Normalization

Even if brain activity can be well localized within a subject through coregistration, there remains the problem of comparing activity across subjects, whether in the same study or across studies. Human brain varies significantly from one individual to another considering its shape, its size and its orientation. In order to perform an intersubject comparison, each subject's brain should be transformed in a way to obtain the same size and the same shape as all of the others. This process, called normalization, compensates the differences by mathematically stretching, squeezing and warping each brain into a common stereotaxic space. The stereotaxic space is a precise mapping system (in this case of the brain) that uses three-dimensional coordinates (see Figure 2.22). If data within two different studies have been normalized in the same fashion, then areas of activity found in each study can be compared.

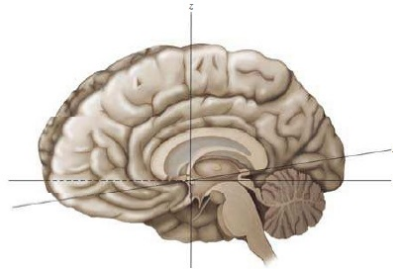


Figure 2.22: Typical coordinate system for fMRI data. [56]

2.6.5 Spatial smoothing

In neuroimaging, spatial smoothing is used to remove uninteresting variation in the data that can be safely attributed to noise sources, while preserving signals of interest. This procedure is used to increase functional SNR and to facilitate the following statistical analysis. In fMRI analyses, the most common smoothing technique applies a Gaussian filter. In this way, the new voxel intensity is a weighted average among the nearby voxels intensities. The weights and the number of voxels involved in this operation depend on the width of the filter, that is generally expressed through the Full Width at Half Maximum (FWHM) (see Figure 2.23 and Figure 2.24).

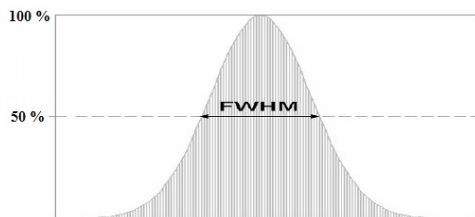


Figure 2.23: Gaussian filter 2D. [60]

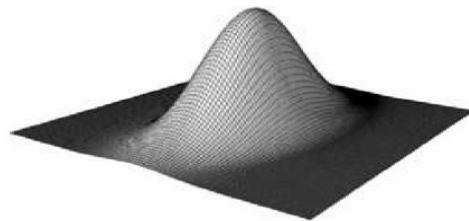


Figure 2.24: Gaussian filter 3D. [60]

The final image obtained is a blurred image with reduced high-frequency spatial components (see Figure 2.25).

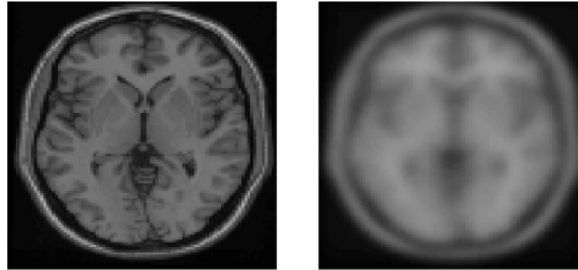


Figure 2.25: Original functional image (left side) and smoothed image (right side). [56]

2.7 Statistical analysis

One of the main goal of fMRI experiments is to extract information regarding the brain activities related to specific tasks. The statistical analysis is used to verify these information from a statistical point of view and thus to derive statistical parametric maps of active and inactive voxels in the brain. Moreover, with the inferential statistics, it is possible to make inferences about the characteristics of a population based upon data obtain from a smaller sample (see Figure 2.26).

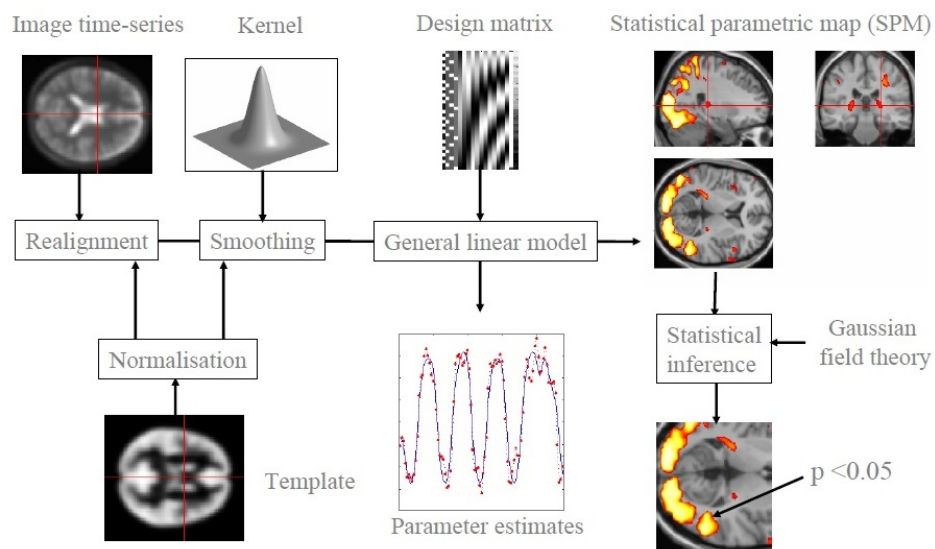


Figure 2.26: Steps from data preprocessing to data statistical analysis. [61]

There are many different approaches to fMRI data statistical analysis and the correct one for any given experiment depends on the nature of the experimental design, the hypotheses to be tested and the field of application. Some of these statistical methods are:

- t-test
- Correlation Analysis
- General Linear Model (GLM)
- Kolmogorov-Smirnov
- Fourier Analysis
- Independent Component Analysis (ICA)

Mostly because its flexibility and power, nowadays the standard is the *General Linear Model*.

2.7.1 General Linear Model

The General Linear Model is a mathematical model that assumes that the data can be treated as a linear summation of a number of dissociable factors. The basic idea behind a linear model is that the observed data (y) is equal to a weighted combination of several model factors (x_i) plus an additive error term (ϵ). The parameter weights (β_i) indicate how much each factor contributes to the overall data.

$$y = \beta_0 + \beta_1 x_1 + \beta_2 x_2 + \dots + \beta_n x_n + \epsilon \quad (2.7)$$

The Equation 2.7 is known as a univariate multiple regression model, but it can be extended to include a large number of dependent variables, such as the many time points within an fMRI study, through the general linear model (see Figure 2.27).

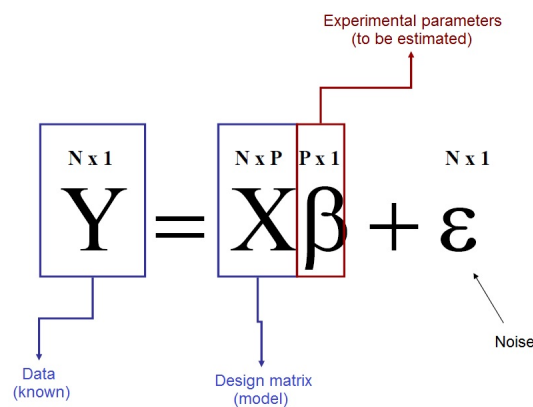


Figure 2.27: Matrix notation of the General Linear Model.

In the linear model equation there is only one known quantity, the experimental data. The model factors represent hypothesized components of the data, but may or may not be meaningful. Given the data and a specified set of model factors, it is possible to calculate which combination of weight is needed to minimize the error. The error term is modelled as additive Gaussian noise independently distributed $\epsilon \sim \mathcal{N}(0, \sigma^2 \mathbf{I})$.

Model specification

The matrix X is known as the *design matrix* and has one row per observation and one column (explanatory variable) per model parameter. It is a near description of the model that encodes and quantifies the knowledge about how the expected signal was produced. In particular, the explanatory variables $x(t)$ represent the predicted BOLD time course arising from neuronal activity up to some scaling factor [62]. This neuronal activity is assumed to be caused by a sequence of experimental manipulations and is usually referred to as the stimulus function. A key concept is that the predicted BOLD response $x(t)$ can be expressed as the convolution of the stimulus function $u(t)$ with the impulse hemodynamic response $h(t)$:

$$x(t) = u(t) \otimes h(t) = \int_0^T u(t - \tau)h(\tau)d\tau \quad (2.8)$$

Observing the Equation 2.8, the dependence of the BOLD signal from both the stimulus and the hemodynamic response becomes evident and therefore setting up an appropriate experimental design is crucial.

The hemodynamic impulse response function $h(t)$ can be mathematically described in many different ways. Some of them are:

- Canonical
- Canonical temporal derivatives
- Canonical dispersion derivatives

The *canonical* function is a "typical" BOLD impulse response characterized by two gamma functions, one modelling the peak and one modelling the undershoot [62] (see Figure 2.28). It can be described by Equation 2.9 (introduced by Friston in 1998), in which the values of a_1 , a_2 , b_1 , b_2 and c are fixed.

$$h(t) = \left(\frac{t}{d_1}\right)^{a_1} \exp\left(\frac{-(t-d_1)}{b_1}\right) - c\left(\frac{t}{d_2}\right)^{a_2} \exp\left(\frac{-(t-d_2)}{b_2}\right) \quad d_i = a_i b_i \quad (2.9)$$

The *canonical temporal derivatives* function is composed by two gamma functions plus a multivariate Taylor expansion in time. The temporal derivative (see Figure 2.28) can model (small) differences in the latency of the peak response.

The *canonical dispersion derivatives* function is composed by two gamma functions plus a multivariate Taylor expansion in time and in width. The dispersion derivative (see Figure 2.28) can model (small) differences in the duration of the peak response. In particular, it can model also the initial undershoot.

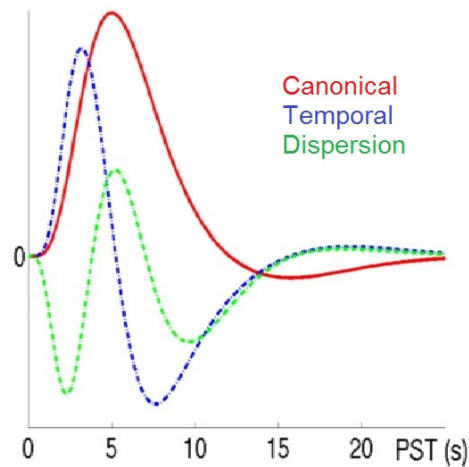


Figure 2.28: Canonical function (red), temporal derivative (dashed blue) and dispersion derivative (dashed green). [59]

Parameter estimation

The parameters that have to be estimated are the weights β_i per each explanatory variable and the noise variance σ^2 . The weights are determined in order to minimize the error and thus, for their estimation, the ordinary least squares method is used:

$$\hat{\beta} = (\mathbf{X}^T \mathbf{X})^{-1} \mathbf{X}^T \mathbf{Y} \quad (2.10)$$

The residuals could be seen as an estimation of the error:

$$\mathbf{Y} - \mathbf{X} \hat{\beta} = \hat{\epsilon} \quad (2.11)$$

If N is the number of time points and P is the number of explanatory variables, the noise variance is estimated with:

$$\hat{\sigma}^2 = \frac{\hat{\epsilon}^T \hat{\epsilon}}{N - P} \quad (2.12)$$

Significance test

Each column of the design matrix corresponds to an effect that could be of interest (because it is built into the experiment) or of no interest (because it may confound the results). Usually, an effect of interest is specified by a vector of contrast weights c that gives a weighted sum of parameter estimates referred to as a *contrast* [62]. This vector is composed by positive and negative integer values and each vector is orthogonal to all the other contrast vectors.

Once decided the contrast vector, it is necessary to apply a *t-test* for each brain voxel that tests for the effect of interest in that voxel. A *t-statistic*, called also *t-contrast*, can then be formed by dividing a contrast of the estimated parameters (effect size) by its estimated standard deviation (uncertainty of effect size):

$$t = \frac{\mathbf{c}^T \boldsymbol{\beta}}{\sigma \sqrt{\mathbf{c}^T (\mathbf{X}^T \mathbf{X})^{-1} \mathbf{c}}} \quad (2.13)$$

The statistic calculation is often used to decide whether the statistic represents convincing evidence of the effect of interest. In general, the statistic is tested against the *null hypothesis* (H_0), which is the hypothesis that there is no effect. If the statistic is not compatible with the null hypothesis, it is possible to conclude that there is an effect [62]. It is therefore necessary to compare the t-statistic against to a *null distribution*, which is the distribution of statistic values expected if there is no effect and that is completely determined by the number of degrees of freedom ($N - P$). Then a *significance level* (*alpha value*) has to be set, which corresponds to the probability to reject H_0 when H_0 is true (*type I error*, or *false positive rate*, see Figure 2.29). The result of the comparison provides information regarding the significance of the effect of interest.

		ASSUMPTION	
		H0 assumed	H0 rejected
REALITY	H0 true	HIT	Type I Error
	H0 false	Type II Error	Correct Rejection

Figure 2.29: Possible results of a significance test.

2.7.2 Correction for multiple comparisons

One of the central problem in fMRI data analysis is the problem of multiple comparison. Due to the fact that there are many thousands of voxels and therefore many thousands of statistic values, the greater the number of statistical tests conducted, the greater the chance of a false positive result. The standard strategy for overcoming the problem of multiple comparisons is reducing the alpha value, so that voxels are less likely to pass the significance threshold do to chance. A common and stringent method for doing so is *Bonferroni correction*, in which the alpha value is decreased proportionally to the number of the independent statistical test, that is equal to the total number of voxels per slice (n):

$$\alpha(\text{corrected}) = \frac{\alpha}{n} \quad (2.14)$$

Bonferroni correction effectively controls for type I error, increasing the researcher's confidence that positive statistical tests correspond to meaningful activation (see Figure 2.30).

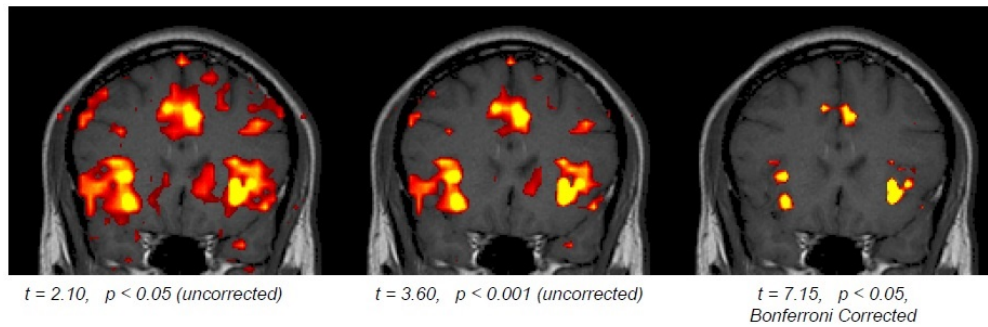


Figure 2.30: Effects of Bonferroni correction. [56]

However, in practice, it has severe disadvantages. While it decreases type I error, it also increases the probability of type II error, or failing to detect voxels with real activity. For many research questions, especially those that are novel or exploratory or have clinical relevance, an increased rate of type II error may be unacceptable. In these cases, a less conservative approach could be used, like the *false discovery rate*.

Chapter 3

Kinematic Analysis

In this chapter a summary of the kinematic analysis theory is given. In the first part, the principles of the kinematic analysis are treated, in particular the calibration, the 3D reconstruction and the tracking. In the second part, the ways to implement the same aspects by SIMI Motion©, the motion capture system used in the present thesis, are briefly illustrated.

3.1 Principles of kinematic analysis

Kinematic analysis is the process of measuring kinematic quantities used to describe motion without considering its causes. Kinematic quantities that can be measured during motion are the position of points (or objects) in space, their trajectories and other specific properties like velocity and acceleration. The multitude of possible applications of kinematic analysis allows it to be widely used in a lot of different fields, such as astrophysics, mechanics, robotics and many others. Since ancient times, a discipline of particular interest was the study of the human body movement and thus, in consequence, the human movement analysis.

With the help of the recent technology it is possible to detect human body movement using specific systems, known as *motion capture systems*. Motion capture consists of recording a motion event and translating it into a mathematical representation [63]. This is possible by tracking a number of key points in space over time in order to have a single 3D reconstruction of the performance. The digital model obtained is then useful for further studies and specific applications. In general, motion capture systems are divided into two main categories: *non-optical systems* and *optical systems*.

3.1.1 Non-optical systems

Non-optical systems include electromechanical and electromagnetic devices.

Electromechanical systems are usually made up of potentiometers and sliding rods fixed at specific points in the body. The movement of the subject is detected thanks to small changes in the potentiometers. Their main disadvantage is that, due to their weight and encumbrance, they may limit the range of motion that could be performed [64].

Electromagnetic systems involve instead the placement of sensors devices on the subject. The strength of these systems is that they are cheap and highly portable and thus permit to extend the range of motion that is possible to capture. However, the sensors often need wires connections and this still represents a strong limitation [64].

3.1.2 Optical systems

Optical systems consist of multiple video-cameras that record from different views the moving subject in order to determine its position over time. The system could be marker-based (with the use of active or passive markers) or could use a markerless approach. Systems that use passive markers are the most widespread, especially for clinical applications [64]. Data acquisition is possible thanks to the use of simple little balls covered with a retroreflective coating that are able to reflect the illumination. In this way, markers appear on each camera image as bright dots easily detectable and the position of their centroids can be measured [65].

Optical systems are nowadays largely the most popular in movement analysis, thanks to several advantages over the other techniques [64]. Some of them are:

- high level of accuracy of results
- markers do not cause encumbrance on the subject
- markers do not limit spontaneous movement
- markers do not require any powering

One of the main drawback is that the motion capture system loses track of the markers when they are completely hidden or when a markers swapping occurs.

Calibration

Calibration of the cameras is a fundamental step required for the 3D reconstruction of the movement. The main goal of calibration is to estimate two different sets of parameters: the *intrinsic parameters* and the *extrinsic parameters* [66]. The intrinsic parameters are parameters of the optical model that explains how the 3D scene is projected to the 2D image frame (focal length, principal points coordinates and distortion coefficients). The extrinsic parameters are instead associated to the position and the orientation of the cameras in the space (position of the camera reference frame with respect to absolute reference system).

Particularly popular is the *Direct Linear Transformation (DLT) algorithm* [66], where all the parameters are estimated at the same time from the projection image of a calibration grid of known size. Similarity equations are written for every control point and then combined into a system that is solved by standards methods. The best accuracy is achieved when the control points are large in number and evenly distributed in the calibration volume.

Another method for cameras calibration allows to estimate the principal parameters of the cameras without using any other additional device [67]. This approach, very common in the computer vision community, is able to calibrate on-line the intrinsic and extrinsic parameters by surveying a rigid bar in motion inside the working volume.

The calibration is performed with three subsequent transformations [68] (see Figure 3.1):

1. A *rigid transformation* from the absolute coordinate system to the camera's coordinate system, which is placed in the center of projection
2. A *perspective projection* from the three-dimensional (3D) space to the two-dimensional (2D) space of the camera
3. A *2D affine transformation* from the image coordinate system to the sensor's reference system

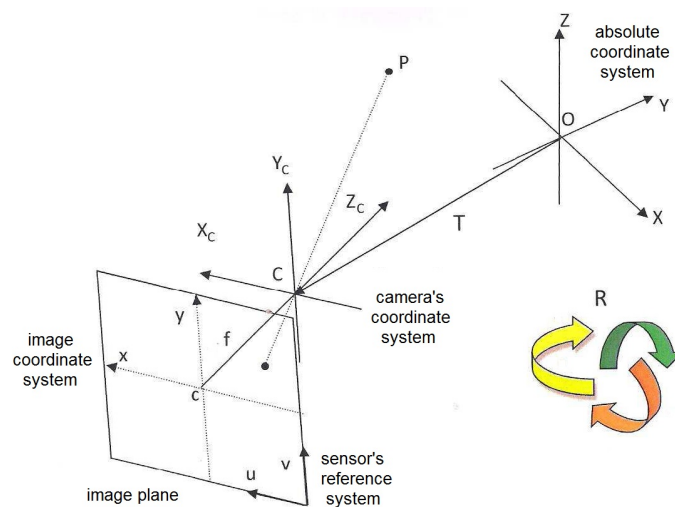


Figure 3.1: The point P projection on the image plane in the 3D space. [68]

Each camera can be described by the simple *pin-hole model* [69]. The pin-hole model is the perspective projection model used to transform the real 3D coordinates to 2D image coordinates. In this model, all the rays coming from the scene must cross a small hole to impact with the image sensor (see Figure 3.2). Real lenses do not have this linear behaviour, so that the pin-hole model can be corrected with distortion corrective terms. In this way, the ideal behaviour can become as close as possible to the real behaviour of the lenses [70].

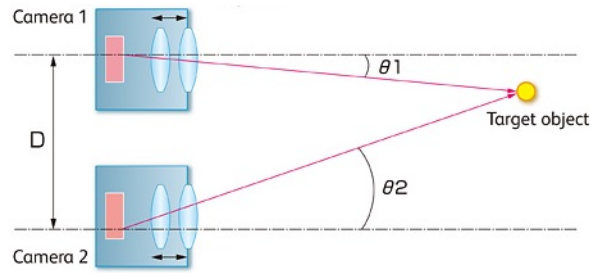


Figure 3.4: Graphical representation of the triangulation method. [70]

The tracking procedure is one of the main problems for marker-based capture systems due to the fact that multiple markers are present in the scene at the same time and thus some of them could be not visible in some frames. A great effort has been spent on algorithms that are able to perform a correct tracking of the 3D trajectories throughout a sequence, even when the markers are occluded in some views, or when they are very close to each other [65].

3.2 Kinematic analysis with SIMI Motion©

SIMI Motion© is a motion capture and analysis system developed by Simi Reality Motion System GmbH© in Munich, Germany (<http://simi.com>). It is an optical system particularly suitable for movement and behaviour analysis for medicine, sport, industry and entertainment.

Calibration with SIMI Motion©

There are two main cameras calibration procedures that can be implemented: a *Static Calibration* and a *Wand-Calibration*.

The Static Calibration is performed by recording a short video of a particular device placed inside the working volume. Usually, the device looks like a grid that consists of multiple points whose coordinates in the absolute reference system are known. Due that the device is not moving over time, it is enough to record just one frame. With this procedure, all the cameras parameters required are estimated. A rapid check to measure the accuracy of the calibration is to control the output regarding the axis angle, which could be $\simeq 90^\circ$.

The Wand-Calibration consists of a static calibration and a dynamic calibration. The static calibration is performed laying down a rigid object on which are fixed 4 marker forming an "L" (*L-Frame*, see Figure 3.5). The small shank is used to set the x-axis and the long shank to set the y-axis of the global coordinate system. The z-axis could be found choosing a right hand coordinate system. At the same time, the dynamic calibration is performed using

a rigid object on which are fixed 3 markers forming a straight line (*T-Wand*, see Figure 3.5). While the distances between the markers on the L-Frame are of no interest, it is on the other hand important to know the distance between the external markers of the T-Wand. The T-Wand is therefore moved for 30-40 seconds in random positions covering the movement area to set the metric system. From the recorded video, that lasts for all the duration of the T-Wand movement, it is possible to extract all the cameras parameters of interest. A first indication about the accuracy of the calibration is obtained in terms of mean and standard deviation of the T-Wand length measurements: the first should be close to the real value and the second should be as low as possible.



Figure 3.5: Devices used for the Wand Calibration.

It has been demonstrated that the Wand-Calibration leads to more accurate results and for this reason it has almost completely replaced the older Static Calibration.

3D reconstruction and tracking with SIMI Motion©

Once having calibrated the cameras and having recorded a movement video using passive markers, it is possible to reconstruct the 3D coordinates of the markers. With the automatic tracking, the software is able to automatically detect all the visible markers in the video. It is also possible to set the marker sensitivity in order to obtain the value that fits best in the specific video. The automatic tracking procedure has the advantage to be fast but however it could fail in the case of markers occlusion. To solve this problem, different strategies are available. If the gaps are small, after the 3D coordinates reconstruction of the visible markers it is possible to estimate the missing values of the hidden markers using the interpolation method (linear or spline). On the other hand, if there are many missing values, the interpolation method could lead to unacceptable results and thus it is recommended to execute a manual tracking.

After the tracking, it is necessary to do the markers assignment, that means to label every marker in every frame with its name. Usually, in human movement analysis, every marker takes the name of the correspondent part of the body on which it is placed (see Figure 3.6). The markers assignment consists of two steps: first, it is necessary a manually association of every marker with its correct label in just one image frame and second, the software automatically recognizes the same markers in all the subsequent image frames. One of the major problem of this process is when two or more markers overlap and some markers swapping occur. In this situations, it is better to manually check and correct the markers assignments.

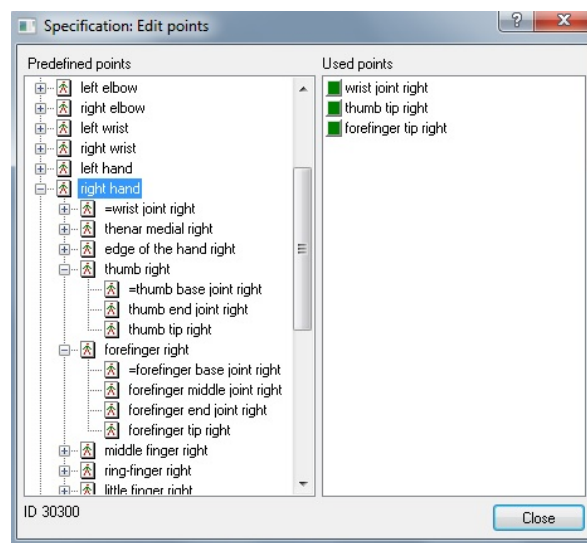


Figure 3.6: Examples of markers labels.

At this point, the software performs a 3D calculation of all the 3D markers coordinates over time. It is possible to manipulate the 3D coordinates succession applying many different mathematical algorithms like filters, interpolations and many others. Moreover, from these "primary" information it is possible to obtain a multitude of "secondary" information, like distances, velocities, accelerations and so on. Results can easily be displayed and the data can be exported for further computations.

Chapter 4

Materials

In this chapter indications about the participants of the experiments and about the main components of the experimental apparatus are given.

4.1 Participants

Ten healthy volunteers (3 men, 7 women, mean 24.8 ± 2.6 years old) participated in the experiments. All participants fulfilled the inclusion criteria indicated by the Italian Society of Medical Radiology, none had a history of neurological, major medical, or psychiatric disorders. They were all right-handed according to the Edinburgh Handedness Inventory (Oldfield, 1971). Experimental procedures and scanning protocols were approved by the Padova University Hospital and conducted in accordance with the Declaration of Helsinki (Sixth revision, 2008). All participants gave their informed written consent to participate at the experiments.

4.2 Apparatus

4.2.1 fMRI scanner

All the fMRI images were acquired using the whole body scanner Siemens Magnetom Avanto 1.5 T located at Padova University Hospital. The scanner was equipped with a standard Siemens eight channels coils.

4.2.2 Motion capture system

All the movement data acquisitions and analyses were conducted using the SIMI Motion© System developed by Simi Reality Motion System GmbH© in Munich, Germany (<http://simi.com>).

The motion capture and analysis equipment was composed by:

- two cameras
- a set of passive markers
- SIMI Motion© Software

Cameras

Two high-speed industrial cameras Allied Vision Technologies (AVT) were used for all the videos acquisitions. The cameras were modified in their electronic parts in order to be placed inside the MR room. They were handed on the ceiling in front of the scanning bed, one on the left and one on the right side.

Markers

A set of passive reflective markers of 10 *mm* diameter was used (see Figure 4.1), both for the calibrations and the experiments.

Software

The Software Simi Motion© version 9.0.5 was used.



Figure 4.1: Reflective passive markers with plastic support.

Chapter 5

Methods

In this chapter all the methods used in the present thesis are described. In the first part, the preparation, the experimental protocol, the data acquisition and the fMRI data preprocessing are explained. In the second part, all the strategies adopted to analyse the kinematic data and the fMRI data are given.

5.1 Preparation

5.1.1 Cameras settings

The focus and the aperture of the two cameras were adjusted for the reach-to-grasp experiment in order to cover only the movement area. There was no need to correct for the "eye fish" effect using distortion correction parameters because the field of view was small and well-focused. The exposure time was set to 3 *ms* and the acquisition frequency was set to 50 *Hz*.

5.1.2 3D Calibration

Before the beginning of the first experiment, the 3D calibration of the camera system was performed. Because the positions and the zoom of the cameras have not been changed until the end of the last experiment, there was no need to perform the calibration other times. Both the different way of calibration were tested: the *Static Calibration* and the *Wand-Calibration*.

Static Calibration

The Static Calibration was performed using a parallelepiped placed on the scanning bed in correspondence of the movement area (see Figure 5.1). On the parallelepiped (24 *cm* x 24 *cm* x 44 *cm*) were fixed 25 markers, 5 on each face except on the bottom one, with known coordinates (see Figure 5.2 and Table 5.1). However, in order to perform the calibration with

two cameras, only the markers that were visible from both of the cameras could be used. Therefore, the markers considered have been the numbers 1, 2, 3, 4, 5, 6, 7, 11, 12, 13, 14, 15, 21 and 22.

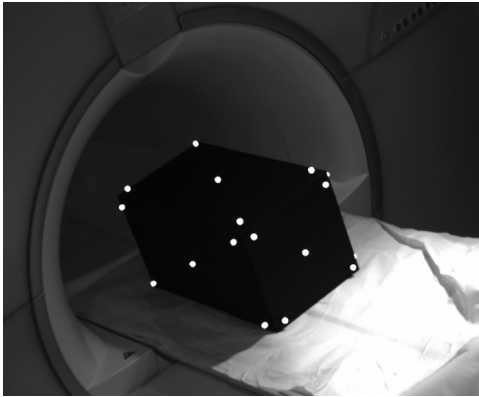


Figure 5.1: Parallelepiped used for the Static Calibration.

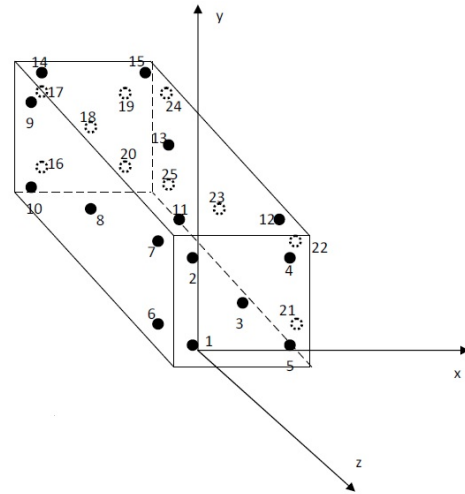


Figure 5.2: Positions of the markers on the parallelepiped used for the Static Calibration.

Wand-Calibration

The Wand-Calibration consisted of a static calibration and a dynamic calibration. The static calibration was performed positioning 4 markers on the scanning bed forming an "L" (see Figure 5.3). The dynamic calibration was performed using a rigid object on which were fixed 3 markers forming a straight line (see Figure 5.3). The distance between the external markers was 27 cm. This object (Wand) was moved for 30-40 seconds in random positions covering the movement area.

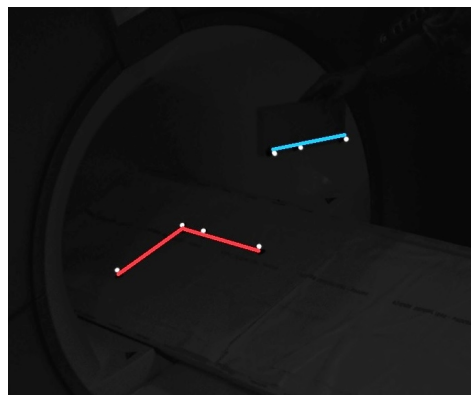


Figure 5.3: The static "L" and the moving Wand.

# marker	x	y	z
1	0	0	0
2	0	20	0
3	10	10	0
4	20	20	0
5	20	0	0
6	-2.5	0	-2.5
7	-2.5	20	-2.5
8	-2.5	10	-22.5
9	-2.5	20	-42.5
10	-2.5	0	-42.5
11	0	22.5	-2.5
12	20	22.5	-2.5
13	10	22.5	-22.5
14	0	22.5	-42.5
15	20	22.5	-42.5
16	0	0	-45
17	0	20	-45
18	10	10	-45
19	20	20	-45
20	20	0	-45
21	22.5	0	-2.5
22	22.5	20	-2.5
23	22.5	10	-22.5
24	22.5	20	-42.5
25	22.5	0	-42.5

Table 5.1: Coordinates of the marker centers [cm] on the parallelepiped used for the Static Calibration.

Calibrations comparison

In order to compare the two way of calibration, a video of a moving object with a known length (27 cm) was recorded. Therefore, the length of the object was measured using the two different calibration videos.

5.1.3 Markers placement

On the right hand of the participant were fixed 3 passive markers: one on the wrist, one on the thumb tip and one on the forefinger tip (see Figure 5.4). They were slightly modified prolonging a little the plastic support to minimize markers occlusions and thus to make them visible from the cameras as much time as possible. The participant was then instructed to perform the reach-to-grasp movement a couple of times before the acquisition in order to verify if all the markers were correctly detected from all the cameras. If some markers appeared not well-visible, their position was mildly adjusted until reaching the best setting.



Figure 5.4: Position of the 3 markers on the right hand.

5.2 Experimental protocol

The experimental stimulus consisted of a small wooden sphere of 2 *cm* diameter fixed on a platform in front of the participant (see Figure 5.5). Participants were requested to perform the reach-to-grasp movement using a precision grip and to keep their eyes on the stimulus during movement execution. To facilitate direct viewing of the stimulus, the head was slightly tilted ($10 - 15^\circ$) by means of foam MRI compatible cushions. Given that participants performed the actions with the right hand, a further cushion was placed under the upper right arm in order to minimize discomfort during the movement. The "go" signal to start the movement was provided to the participants by an acoustic tone delivered through MR-compatible headphones. Participants were requested to perform the movement at a natural speed.

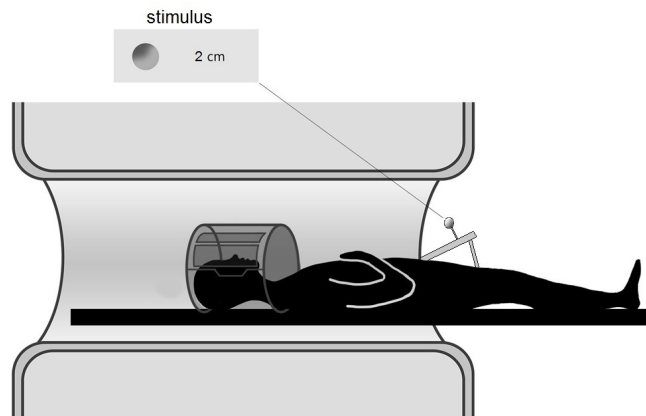


Figure 5.5: Experimental setup of data acquisition.

The entire experiment consisted of two runs (i.e. sessions) of 50 trials each. A mixed design was adopted with variable interstimulus interval (ISI) that varied from 5 to 10 seconds. This approach has been used mainly to control for predictability phenomena, possibly induced by ISI duration of constant length. The ISI sequence in the two runs was different and was kept the same for all the participants.

5.3 Data acquisition

Kinematic data and fMRI data were acquired simultaneously.

5.3.1 Kinematic data acquisition

One high resolution video (AVI format) per run was recorded. Each video was composed by two views, provided by the two cameras. The onset time of the video corresponded to the onset time of the acquisition of the first considered fMRI volume.

5.3.2 fMRI data acquisition

Functional images were acquired with a gradient-echo, echo-planar (EPI) T2*-weighted sequence in order to measure blood oxygenation level-dependent (BOLD) contrast throughout the whole brain (37 contiguous axial slices acquired with ascending interleaved sequence, 54 x 64 voxels, 3.5 mm x 3.5 mm x 4 mm resolution, FOV = 196 mm x 224 mm, flip angle = 90°, TE = 49 ms). Volumes were acquired continuously for each run with a repetition time (TR) of 3 s. 114 volumes were collected in each single scanning run, resulting in functional runs of 5 min and 42 s duration (11 min and 24 s of acquisition time in all). For each participant, the first two volumes of each fMRI run were discarded because of the non-equilibrium state of the magnetization in order to allow for stabilization. High-resolution T1-weighted image were acquired for each participant (3D MP-RAGE, 176 axial slices, no interslice gap, data matrix 256 x 256, 1 mm isotropic voxels, TR = 1900 ms, TE = 2.91 ms, flip angle = 15°).

5.4 Preprocessing of fMRI data

Preprocessing of fMRI data was performed using SPM12 (Statistical Parametric Mapping, Wellcome Institute of Cognitive Neurology, London, UK), that is a software used for neuroimages data analysis.

The preprocessing operations applied in the present thesis were:

1. Realign
2. Segment
3. Coregister
4. Normalise
5. Smooth

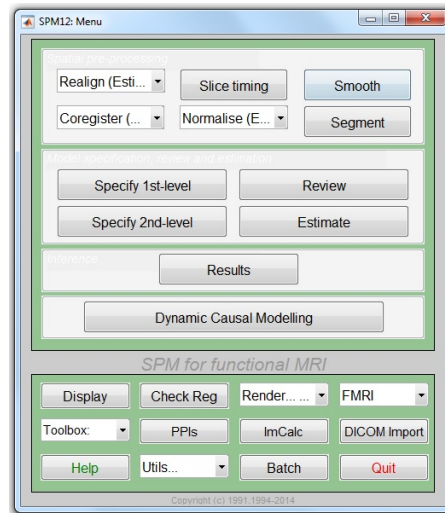


Figure 5.6: The SPM12 base window.

Realign

The realignment aligns the time series of images by minimizing the distances between all the images and a reference image. The 6 spatial transformation (rigid body) parameters are estimated and saved into a file named `rp_***.txt` and a set of new realigned images (`rf***.nii`) is created. A mean image is calculated and saved as `meanf***.nii` and two graphs of the translation and rotation movements are also obtained, which were carefully examined in order to see if the movements were limited and thus correctable.

The steps followed to realign the images were:

- Select "Realign (Est & Res)"
- Highlight "Data", select "New Session" and insert all the functional images (`f***.nii`) of the first session
- Highlight "Data", select "New Session" and insert all the functional images (`f***.nii`) of the second session
- Press "Interpolation" in the "Estimation Options" and select "7th Degree B-Spline"
- Press "Interpolation" in the "Reslice Options" and select "7th Degree B-Spline"

Segment

The segmentation is used to extract the gray matter image from the anatomical T1 image. The gray matter image is saved in a file named `c1s***.nii` and a deformation field is saved in a file named `y_s***.nii`.

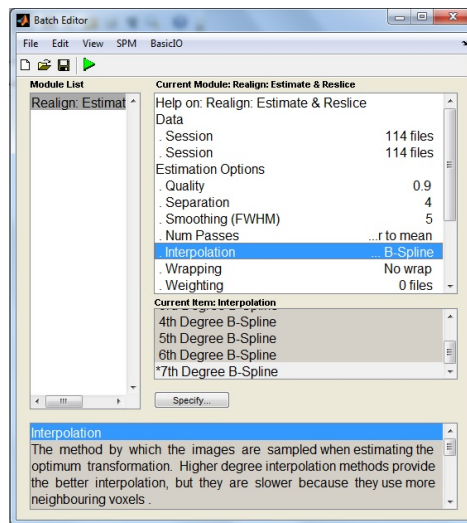


Figure 5.7: Batch Realign: Estimate & Reslice.

The steps followed to segment the gray matter were:

- Select "Segment"
- Press "Native Tissue" in the first "Tissue" ad select "Native Space"
- Press "Native Tissue" in all the other "Tissue" ad select "None"
- Press "Deformation Fields" and select "Forward"

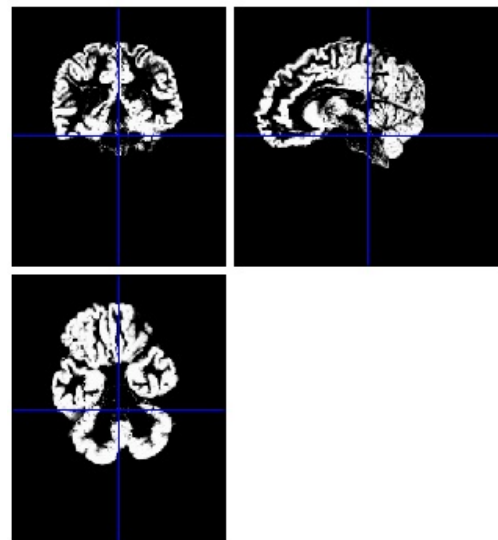
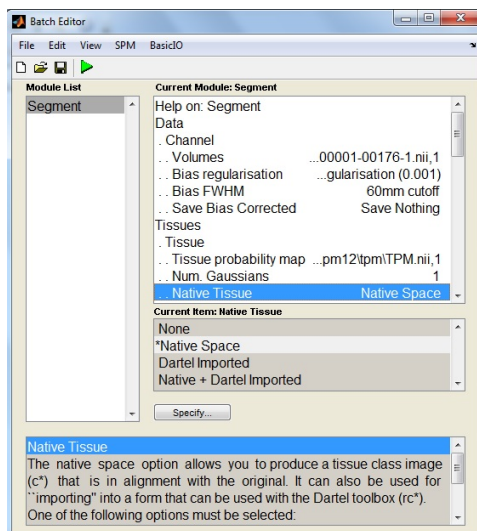


Figure 5.8: Batch Segment.

Figure 5.9: Segmented gray matter.

Coregister

The coregistration is needed to align the functional images to the anatomical image. This procedure is implemented by maximizing the mutual information.

The steps followed to coregister the images were:

- Select "Coregister (Estimate)"
- Select "Reference Image" and insert the segmented gray matter image `c1s***.nii`
- Select "Source Image" and insert the mean image `meanf***.nii`
- Select "Other Image" and insert all the other functional images of both sessions (`rf***.nii`)

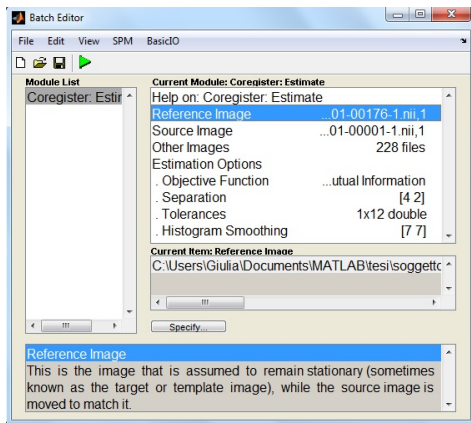


Figure 5.10: Batch Coregister.

Normalised Mutual Information Coregistration

$$X1 = -0.362\%X - 3.546\%Y + 0.579\%Z + 202.886$$

$$Y1 = 0.414\%X + 0.466\%Y + 4.034\%Z + 58.832$$

$$Z1 = -3.474\%X + 0.405\%Y + 0.401\%Z + 194.247$$

Original Joint Histogram

Final Joint Histogram

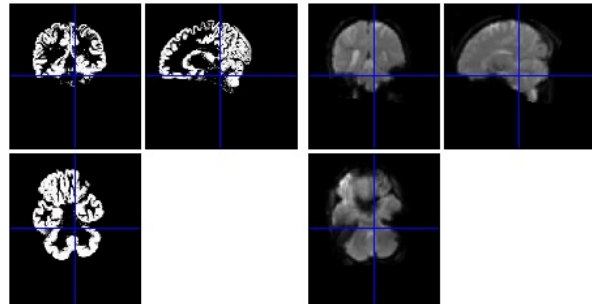
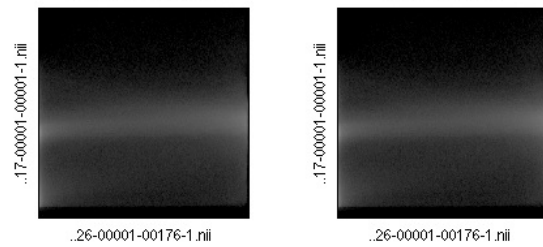


Figure 5.11: Normalized mutual information coregistration.

Normalise

The normalization is executed to adjust the coregistered images into a common stereotaxic space. This procedure was needed in order to perform a comparison across subjects. A set of new normalized images (`wrf***.nii`) is created.

The steps followed to normalise the images were:

- Select "Normalise (Write)"
- Select "Deformation Field" and insert the deformation field image `y_s***.nii`
- Select "Images to Write" and insert all the coregistered images of both sessions (`rf***.nii`)
- Press "Voxel sizes" and enter `[3.5 3.5 4]`
- Press "Interpolation" and select "7th Degree B-Spline"

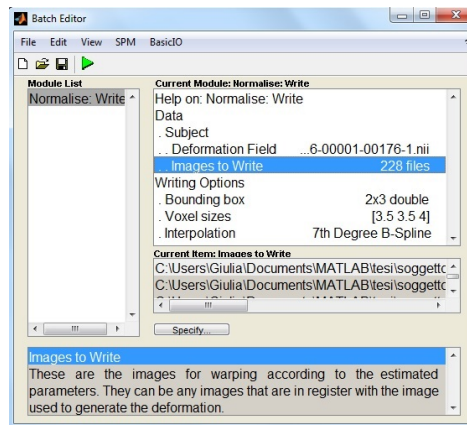


Figure 5.12: Batch Normalise.

Smooth

The spatial smoothing is performed to improve the SNR of the functional images. The filter used was a Gaussian filter with a FWHM equals to twice the voxel size. A set of new smoothed images (`swrf***.nii`) is created.

The steps followed to smooth the images were:

- Select "Smooth"
- Press "Images to Smooth" and insert all the normalized images of both sessions (`wrf***.nii`)
- Press "FWHM" and enter `[7 7 8]`

At this point it was checked if the normalization process have generated acceptable results. This procedure is very sensitive because little errors or imprecisions could lead to irreversible misinterpretations of the final results. This check was executed by pressing the "Check Reg" button and selecting two images to display: one random normalized image `wrf***.nii` and the template `avg305T1.nii` provided by SPM12 (see Figure 5.14). Using the mouse it is possible to navigate these images to confirm whether there is an anatomical correspondence.

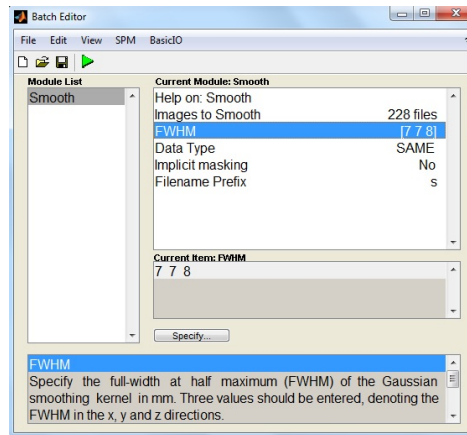


Figure 5.13: Batch Smooth.

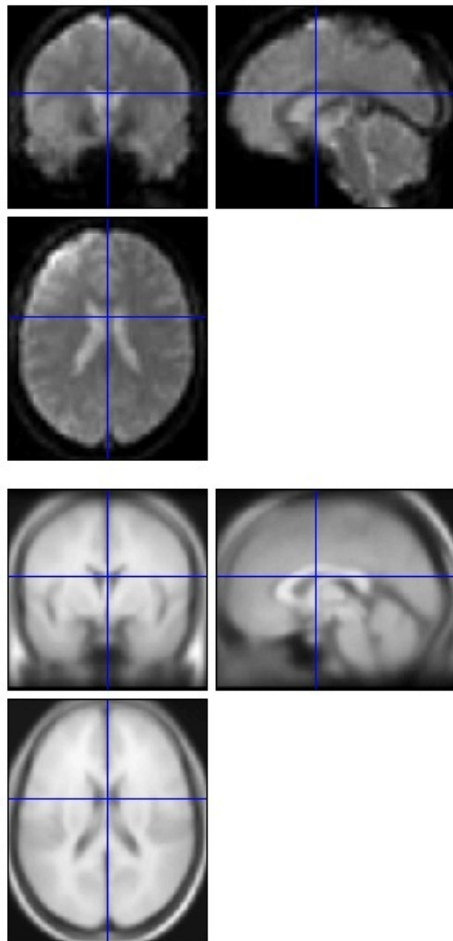


Figure 5.14: Normalized image (top) and common space (bottom).

5.5 Data analysis

The data analysis was executed combining the information provided from both the techniques, i.e. from the movement videos and the fMRI images.

First of all, a set of kinematic parameters were extracted from the movement videos (see Section 5.5.1 and Section 5.5.2). Then, a linear regression analysis was performed (see Section 5.5.3) in order to select only those parameters to insert in the following analyses.

Second of all, a within-subject analysis (1st level analysis, see Section 5.5.4) and a between-subject analysis (2nd level analysis, see Section 5.5.5) were implemented following some different strategies (for a summary, see Table 5.2). Two main methods were tested: the first one consisted of using the kinematic information at the 1st level and the second one of using them at the 2nd level. In the first case, *kinematic regressors* were inserted in the 1st level analysis and then at the 2nd level a "one-sample t-test" was applied (this process was repeated also using normalized kinematic regressors). In the second case, the 1st level analysis was done without kinematic regressors and at the 2nd level the kinematic information were included as *covariates* in the "multiple regression" approach.

Moreover, these analyses were replicated for all the three canonical models of the hemodynamic response function (canonical HRF), i.e. *canonical* (model 1), *canonical temporal derivatives* (model 2) and *canonical dispersion derivatives* (model 3).

	1st level	2nd level
Strategy I	kinematic regressors model 1	one-sample t-test
Strategy II	kinematic regressors model 2	one-sample t-test
Strategy III	kinematic regressors model 3	one-sample t-test
Strategy IV	normalized kinematic regressors model 1	one-sample t-test
Strategy V	normalized kinematic regressors model 2	one-sample t-test
Strategy VI	normalized kinematic regressors model 3	one-sample t-test
Strategy VII	no kinematic regressors model 1	multiple regression kinematic covariates
Strategy VIII	no kinematic regressors model 2	multiple regression kinematic covariates
Strategy IX	no kinematic regressors model 3	multiple regression kinematic covariates

Table 5.2: Summary of all the strategies adopted.

Lastly, the strategy that better describes the data from both a mathematical and a neurophysiological point of view was identified (see Section 5.5.6).

5.5.1 Kinematic quantities computation

The kinematic quantities computation was performed using the software Simi Motion©. At the beginning, the automatic tracking was tried on every video. In some videos the procedure correctly recognized all the markers, but in others the automatic tracking failed due to the presence of many markers occlusions, mostly of the thumb tip marker. In these cases, the manual tracking was performed. After the tracking, the markers assignment was done. In some videos the process correctly associated all the markers in all the image frames, but in others there were several markers swapping between the thumb tip marker and the forefinger tip marker. In these cases, every crucial frame was manually checked and corrected. At this point, it was possible to reconstruct for reach run the 3D coordinates of the wrist, the thumb tip and the forefinger tip over time.

In order to perform a better kinematic quantities computation, some preprocessing was needed. First of all, eventual little gaps in the data were deleted applying a spline interpolation with a maximum interpolation step of 25. Secondly, a first-order low-pass filter with a cut-off frequency of 8 Hz was applied. This is justified from the fact that the frequency content of a movement such as grasping is below 10 Hz [72].

From the 3D coordinates, the following kinematic quantities were derived:

1. wrist absolute velocity
2. wrist absolute acceleration
3. grip aperture (thumb tip - forefinger tip distance)
4. grip aperture absolute velocity

5.5.2 Kinematic parameters extraction

The kinematic parameters extraction was performed using Matlab© (version R2010a, MathWorks, Natick, MA, USA). From the kinematic quantities of each trial (i.e. movement) of each participant (100 trials per participant), a set of parameters were extracted. It is important to underline that the overall hand movement actually consisted of two phases: the first one is the reach-to grasp movement that ends when the hand touches the stimulus and the second one is the return back at the start position. In the present thesis, always only the first phase (reach-to-grasp) was considered.

The kinematic parameters extracted were the following:

1. start of the movement [s]
2. end of the movement [s]
3. movement time (duration of the movement) [s]
4. maximum wrist absolute velocity [m/s]
5. time of maximum wrist absolute velocity [s]
6. maximum grip aperture [m]
7. time of maximum grip aperture [s]
8. maximum grip aperture absolute velocity [m/s]
9. time of maximum grip aperture absolute velocity [s]
10. maximum wrist acceleration [m/s²]
11. time of maximum wrist acceleration [s]
12. maximum wrist deceleration [m/s²]
13. time of maximum wrist deceleration [s]

They were found adopting the following criteria:

- Parameter 1* coincides with the time at which the wrist absolute velocity exceeds 5 mm/s
- Parameter 2* coincides with the time at which, after the start of movement, the wrist absolute velocity reaches a local minimum and simultaneously both the wrist absolute acceleration and the grip aperture absolute velocity are $\simeq 0$
- Parameter 3* is difference between the end of the movement and the start of movement
- Parameter 4 & 5* are the maximum value reached, before the end of the movement, by the wrist absolute velocity and its correspondent time
- Parameter 6 & 7* are the maximum value reached, before the end of the movement, by the grip aperture and its correspondent time
- Parameter 8 & 9* are the maximum value reached, before the end of the movement, by the grip aperture absolute velocity and its correspondent time
- Parameter 10 & 11* are the maximum value reached, before the end of the movement, by the wrist absolute acceleration and its correspondent time

Parameter 12 & 13 are the minimum value reached, before the end of the movement, by the wrist absolute acceleration and its correspondent time

The mean of all the trials for the *parameters 3, 4, 6, 8, 10* and *12* for each participant was also calculated. Except from the movement time, all the other time parameters (i.e. *parameters 1, 2, 5, 7, 9, 11* and *13*) were excluded due to the fact that they were cumulative and thus it were not possible to compare them within the different trials.

At this point, it could be possible to implement the correlation analysis between the BOLD signal and all the kinematic parameters obtained. However, a better way to proceed is trying to reduce the numerosity of the set of the kinematic parameters of interest. This could be done performing a linear regression analysis between every pair of parameters in order to see whether there were some parameters that depended from others.

5.5.3 Linear regression analysis

Regression analysis is a statistical process for estimating the relationships among variables. In particular, the linear regression fits a straight line through the set of n points (in this case $n=100$) in such a way that makes the sum of squared residuals of the model as small as possible.

In general, it is possible to measure the degree of linear dependence between two variables through many different coefficients. The most widely used are the *slope* of the fitted line, the *r coefficient* and the *determination coefficient* r^2 . The slope of the fitted line is equal to the r coefficient corrected by the ratio of standard deviations of the two variables. The r coefficient ranges from -1 to 1: values equal to 1 or -1 correspond to data points lying exactly on a line which means that a linear equation describes the relationship between the two variables perfectly, instead a value equals to 0 implies that there is no linear correlation between the variables. In all the other cases, the more a value is close to 1 (or -1) the higher is the degree of linear dependence between the two variables and on the other hand, the more a value approaches to 0, the lower is the degree of linear dependence. The determination coefficient r^2 is simply the square of the r coefficient and thus ranges from 0 to 1.

The kinematic parameters included in the analysis were the following:

1. maximum wrist absolute velocity (*parameter 4*)
2. maximum grip aperture (*parameter 6*)
3. maximum grip aperture absolute velocity (*parameter 8*)
4. maximum wrist acceleration (*parameter 10*)

5. maximum wrist deceleration (*parameter 12*)
6. movement time (*parameter 3*)

Except from the movement time, all the other time parameters were excluded due to the fact that they were cumulative and thus it were not possible to compare them within the different trials. There were calculated the value of the slope of the fitted line and the determination coefficient r^2 for every pair of kinematic parameters (in this case 13 different combinations).

5.5.4 1st level analysis

The 1st level analysis was performed using the software SPM12. The "first level" models are used to implement a within-subject analysis and typically there are as many first level models as the number of subjects. Statistical analysis of fMRI data used the General Linear Model (GLM) approach. Its implementation needed the specification of the GLM design matrix, the estimation of the GLM parameters and the interrogation of results using contrast vectors to produce Statistical Parametric Maps (SPMs).

Model specification

The steps followed to specify the fMRI model (without using kinematic regressors) were:

- Select "Specify 1st-level"
- Press "Units for design" and select "Seconds"
- Press "Interscan intervals" and enter 3
- Highlight "Data", select "New Subject/Session" and insert all the smoothed images (*swrf***.nii*) of the first session
- In "Conditions" select "Name" and enter the name of the condition (in this case *grasping*)
- In "Conditions" select "Onsets" and enter the vector containing the time onsets of the condition of the first session (in this case *parameter 1*)
- In "Conditions" select "Durations" and enter the vector containing the durations of the condition of the first session (in this case *parameter 3*)
- Press "Multiple regressors" and select the file containing the movement regressors (*rp_***.txt*) of the first session
- Highlight "Data", select "New Subject/Session" and repeat the steps above for the second session
- In "Basis Functions" select "Canonical HRF", press "Model derivatives" and select the appropriate option

It was chosen to test all the three canonical HRF, i.e. *canonical*, *canonical temporal derivatives* and *canonical dispersion derivatives*, in order to compare their results and select the one that describes better the experimental data.

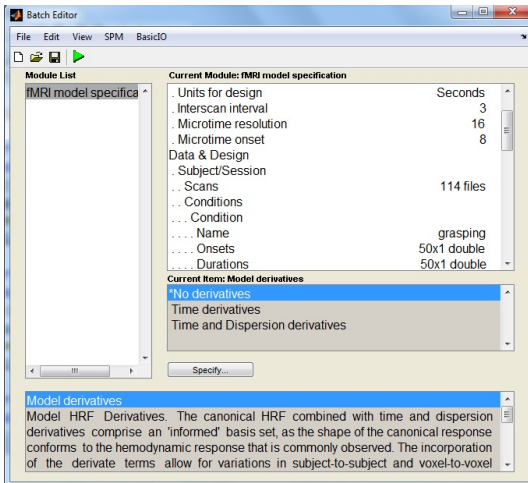


Figure 5.15: Batch Specify 1st-level.

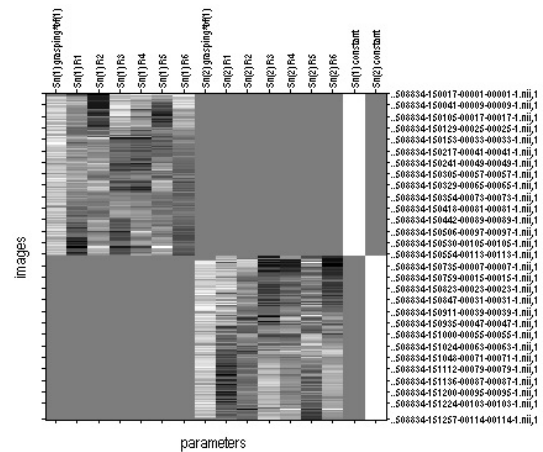


Figure 5.16: Design matrix using the canonical model (model 1).

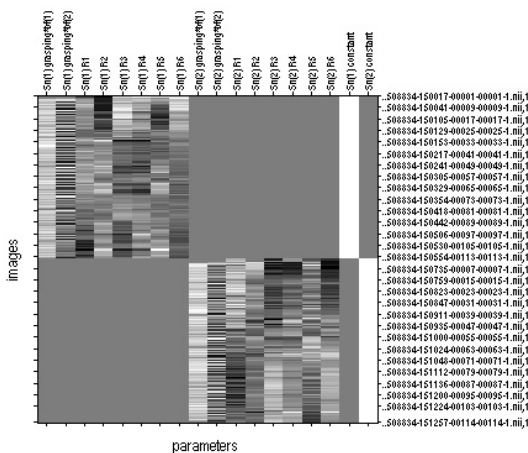


Figure 5.17: Design matrix using the canonical temporal derivatives model (model 2).

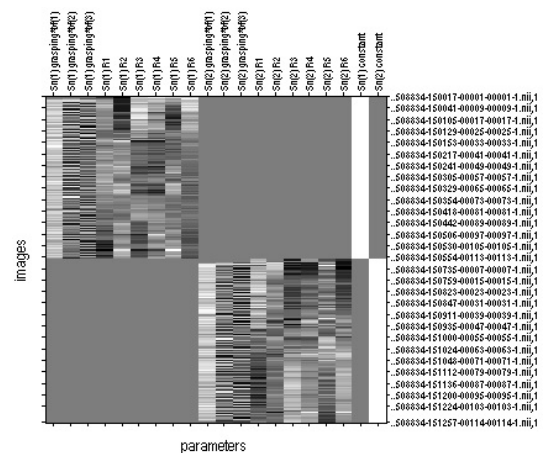


Figure 5.18: Design matrix using the canonical dispersion derivatives model (model 3).

The previous steps were then replicated including the *kinematic regressors*.

The first time, the kinematic regressors were built using the movement time (*parameter 3*), the maximum wrist absolute velocity (*parameter 4*), the maximum grip aperture (*parameter 6*) and the maximum grip aperture absolute velocity (*parameter 8*) of each trial of each session for every participant. From each column vector (50x1) was subtracted its mean value and then each value was inserted in a column vector of the same size of the number of scans

(114x1). The right time slot was calculated from the correspondent time on which every event occurred (i.e. *parameter 1*, *parameter 5*, *parameter 7* and *parameter 9* respectively). Time slots without any event were set to zero.

All the other times, the kinematic regressors were built using the same parameters except from the movement time (*parameter 3*) that was excluded.

The model specification with kinematic regressors was then repeated using also normalized kinematic regressors. They were obtained from the regressors above simply dividing each column by its standard deviation.

Parameters estimation

After the model specification, the parameters estimation is needed (in SMP, button "Estimate"). This process returns as many β parameters as the number of columns of the design matrix.

Only after the first time, the range of values of the estimated β parameter regarding the 4 kinematic regressors (i.e. the movement duration, the maximum wrist absolute velocity, the maximum grip aperture and the maximum grip aperture absolute velocity) were checked from the β images.

Results

After the parameters estimation, it is possible to see the results (in SPM, button "Results"). This process returns as many contrast images as the number of conditions tested. Depending on the presence of the kinematic regressors, different contrast vectors were applied.

Without kinematic regressors, the positive effect of the *grasping* condition was tested.

With kinematic regressors, the conditions tested were the following:

1. positive effect of the *grasping* condition (*contrast 1*)
2. positive effect of the *maximum wrist absolute velocity* condition (*contrast 2*)
3. negative effect of the *maximum wrist absolute velocity* condition (*contrast 3*)
4. positive effect of the *maximum grip aperture* condition (*contrast 4*)
5. negative effect of the *maximum grip aperture* condition (*contrast 5*)
6. positive effect of the *maximum grip aperture absolute velocity* condition (*contrast 6*)
7. negative effect of the *maximum grip aperture absolute velocity* condition (*contrast 7*)

5.5.5 2nd level analysis

The 2nd level analysis was performed using the software SPM12. The "second level" models are used to implement a between-subject analysis in order to make inferences about the population from which the subjects were drawn. Contrast images obtained at the 1st level from each subject are used as summary measures of subject responses and are therefore entered as data into a "second level" model. As at the 1st level, it is necessary to specify the design and to estimate the parameters. Inference on these estimated parameters is then handled by the SPM results section.

Two different approaches were implemented: the "one-sample t-test" and the "multiple regression".

Model specification

The steps followed to specify the fMRI model using the "one-sample t-test" approach were:

- Select "Specify 2nd-level"
- Press "Design" and select "One-sample t-test"
- Press "Scans" and select the contrast images of the condition of interest

The process was repeated for all the 7 conditions.

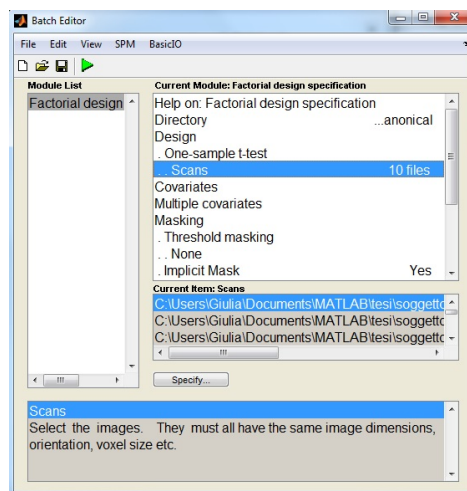


Figure 5.19: Batch One-sample t-test.

The steps followed to specify the fMRI model using the "multiple regression" approach were:

- Select "Specify 2nd-level"

- Press "Design" and select "Multiple regression"
- Press "Scans" and select the contrast images of the *grasping* condition
- Highlight "Multiple covariates", select "New Covariates" and in "File(s)" insert the kinematic covariates

The kinematic covariates were composed by 3 columns (10x1), each of them containing the mean values of all the 100 trials of every participant of the maximum wrist absolute velocity (first column), the maximum grip aperture (second column) and the maximum grip aperture absolute velocity (third column) (see Table 5.3).

	<i>parameter 4</i>	<i>parameter 6</i>	<i>parameter 8</i>
Sbj 1	0.334	0.091	0.164
Sbj 2	0.214	0.104	0.226
Sbj 3	0.160	0.094	0.082
Sbj 4	0.227	0.093	0.161
Sbj 5	0.170	0.091	0.116
Sbj 6	0.330	0.087	0.141
Sbj 7	0.348	0.095	0.214
Sbj 8	0.392	0.105	0.244
Sbj 9	0.249	0.096	0.156
Sbj 10	0.363	0.114	0.252

Table 5.3: Mean values of the maximum wrist absolute velocity (*parameter 4*), the maximum grip aperture (*parameter 6*) and the maximum grip aperture absolute velocity (*parameter 8*).

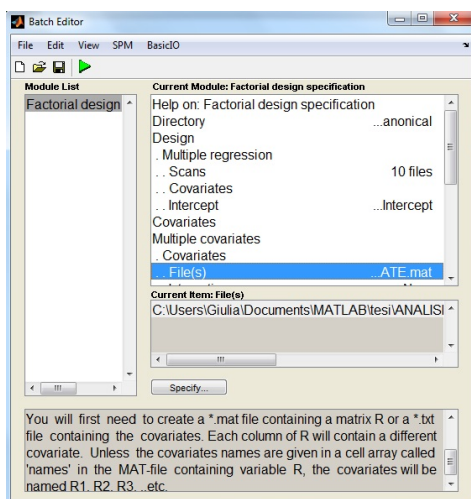


Figure 5.20: Batch Multiple Regression.

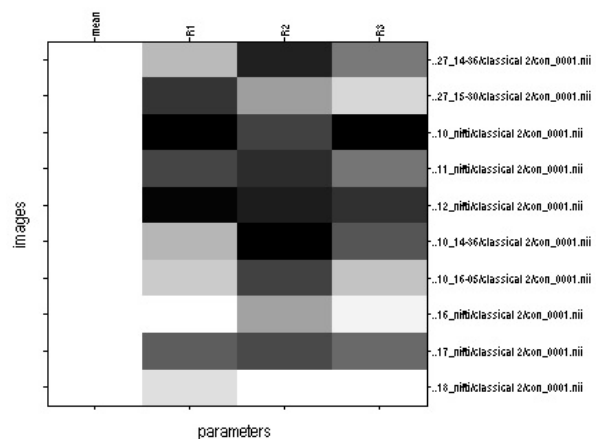


Figure 5.21: Design matrix with kinematic covariates.

Parameters estimation

After the model specification, the parameters estimation is needed (in SMP, button "Estimate"). This process returns as many β parameters as the number of columns of the design matrix.

Results

After the parameters estimation, it is possible to see the results (in SPM, button "Results"). This process returns as many contrast images as the number of conditions tested.

In both the approaches, the conditions tested were the following:

1. positive effect of the *grasping* condition (*contrast 1*)
2. positive effect of the *maximum wrist absolute velocity* condition (*contrast 2*)
3. negative effect of the *maximum wrist absolute velocity* condition (*contrast 3*)
4. positive effect of the *maximum grip aperture* condition (*contrast 4*)
5. negative effect of the *maximum grip aperture* condition (*contrast 5*)
6. positive effect of the *maximum grip aperture absolute velocity* condition (*contrast 6*)
7. negative effect of the *maximum grip aperture absolute velocity* condition (*contrast 7*)

At this point it was possible to obtain the SPMs. At the beginning, it was decided to not use any correction, the p-value was set to 0.005 and the voxels extent threshold was set to 10.

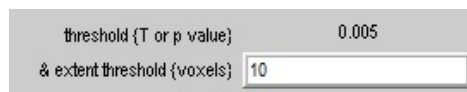


Figure 5.22: Settings of the p-value and the voxels extent threshold.

5.5.6 Strategy identification

The strategy that better describes the data from both a mathematical and a neurophysiological point of view was identified considering two aspects: the differences of the three models of the hemodynamic response and the differences of the two 2nd level approaches.

Hemodynamic response model selection

In order to identify which hemodynamic response model could describe better the experimental data, different criteria were adopted. For each one of the three models, i.e. *canonical* (model 1), *canonical temporal derivatives* (model 2) and *canonical dispersion derivatives* (model 3), the steps followed were:

1. Visually compare the graphs of the model and of the BOLD signal
2. Calculate the Residual Sum of Squares (RSS)
3. Calculate the Akaike Information Criterion coefficient (AIC)

The graph of the BOLD signal was derived directly from the smoothed images selecting one voxel that demonstrated a significant activation. The graph of the model was instead obtained from the design matrix. These two functions were not immediately comparable because the presence of a scaling factor in the model let them have different mean values and amplitudes. For this reasons, from both the functions was subtracted their mean value and the model function was scaled by a new $\hat{\beta}$ factor estimated with the least squares method.

In order to compare the performance of the three models, the simplest index to calculate is the RSS. The RSS is the sum of the differences between the model value and the data value taken in each sample point. The lower is the RSS, the better the model fits the data because the differences are smaller. If y_i are the data samples, x_i are the model samples and N is the number of sample points, the RSS of each model can be found with the following equation:

$$RSS = \sum_{i=1}^N (y_i - \hat{\beta}x_i)^2 \quad (5.1)$$

The RSS is a measure of the goodness of fit, but does not take into account the complexity of the model. In general, the more a model is complex, the lower is the RSS. For this reason, a better index that deals with the trade-off between these two aspects is the AIC, which is lower for the model to be preferred. If p is the number of parameters to estimate, the AIC can be calculated as:

$$AIC = N \cdot \ln(RSS) + 2p \quad (5.2)$$

The number of parameters to estimate grows with the complexity of the model. For the *canonical* model $p = 1$, for the *canonical temporal derivatives* model $p = 2$ and for the *canonical dispersion derivatives* model $p = 3$. Often it is not worth dealing with complex models and thus a lower AIC is preferable than a lower RSS.

2nd level approach selection

The 2nd level approach selection was done comparing some of the SPMs obtained using *contrast 2*, *contrast 3*, *contrast 4*, *contrast 5*, *contrast 6* and *contrast 7*.

The first set of SPMs were derived from all the strategies that adopted the *canonical* model of the hemodynamic response (*model 1*), i.e. *strategy I*, *strategy IV* and *strategy VII*.

The second set of SPMs were derived repeating the 2nd level analysis of all these three strategies using different groups of participants, in particular excluding the participant n° 9, excluding the participants n° 9 and n° 8 and excluding the participants n° 9, n° 8 and n° 5.

Chapter 6

Results and dicussions

In this chapter all the results found from the implemented methods are collected and discussed. First, the results of the calibrations comparison and of the fMRI preprocessing are provided. Then all the results found in order to select the kinematic regressors are given. Lastly the results of the hemodynamic response selection and of the final Statistical Parametric Maps (SPMs) are illustrated.

6.1 3D Calibration

The accuracy of the Static Calibration and of the Wand-Calibration were analyzed and compared.

With the Static Calibration, the axis angle measured was in the first camera 90.20° and in the second camera 90.24° . The calibration is accurate because both the angles are close to 90° .

With the Wand-Calibration, the mean Wand length measured was 26.99 cm and the standard deviation was 2.59 . The calibration is accurate because the mean value is close to the real value (27 cm) and the standard deviation is low.

The results of the calibration comparison (see Figure 6.1) show that the Wand-Calibration is more accurate than the Static Calibration because the mean length of the object is closer to 27 cm and because the standard deviation is lower. Therefore, for all the experiments, it was chosen to utilize the Wand-Calibration.

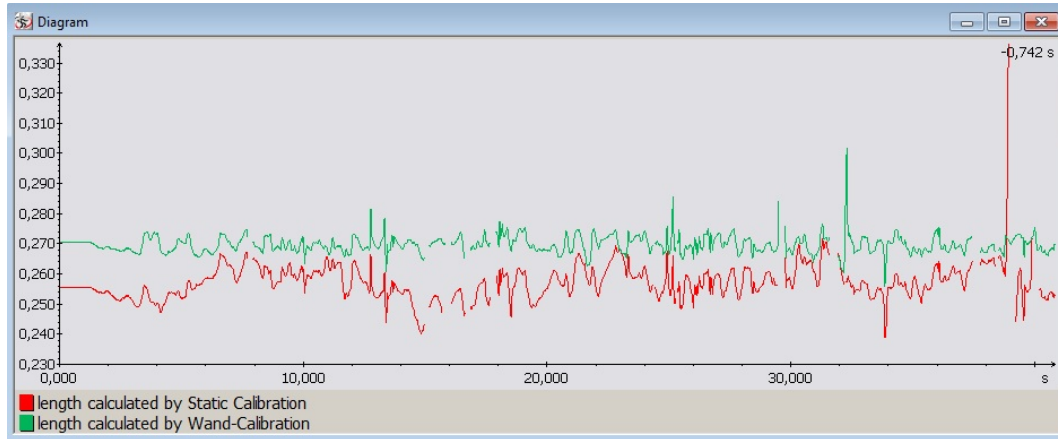


Figure 6.1: Measurements of the length of an object obtained using the Static Calibration video (red) and the Wand-Calibration video (green).

6.2 Preprocessed fMRI data quality check

Before to execute the first level analysis, the data quality after the fMRI data preprocessing were verified, in particular after the realignment and the normalization processes.

In Figure 6.2 and in Figure 6.3 are reported the two graphs of the translation and rotation movements relative to the participant with the smallest head movements amplitude and to the participant with the largest head movements amplitude.

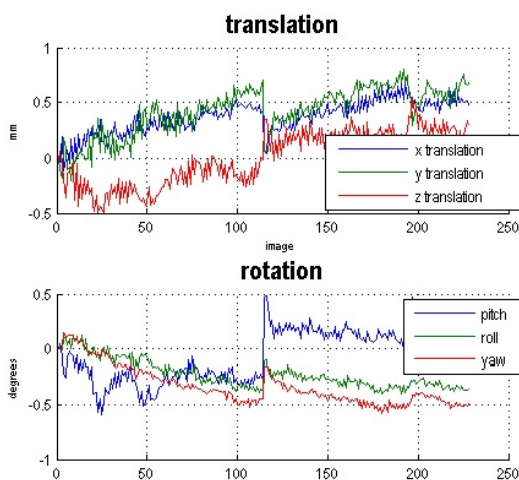


Figure 6.2: Translation and rotation movements of the participant with the smallest head movements amplitude (participant n° 4).

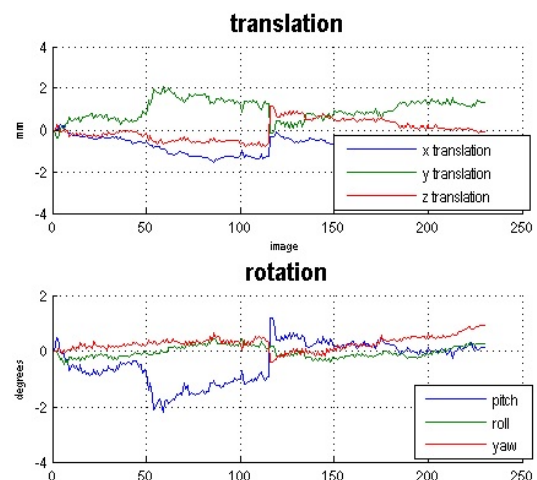


Figure 6.3: Translation and rotation movements of the participant with the largest head movements amplitude (participant n° 9).

In the first case, the translation movement ranges from -0.5 mm to 0.75 mm and in the second case, it ranges from -1.5 mm to 2 mm . Even in the worst case, the amplitude of the translation movement was included in the range of $\pm 5\text{ mm}$ and therefore the movements were correctable and no participant was excluded from the consequent analyses.

The results of the normalization process were checked comparing for each participant one normalized image with the average template provided by SPM12. In all the cases it was confirmed that there is an anatomical correspondence between the two images and thus no participant was excluded from the consequent analyses.

6.3 Kinematic quantities computation

After the 3D coordinates reconstruction of the wrist, the thumb tip and the forefinger tip over time, the interpolation and the filtering were performed. Examples of the result of these two procedures are shown in Figure 6.4 and in Figure 6.5.

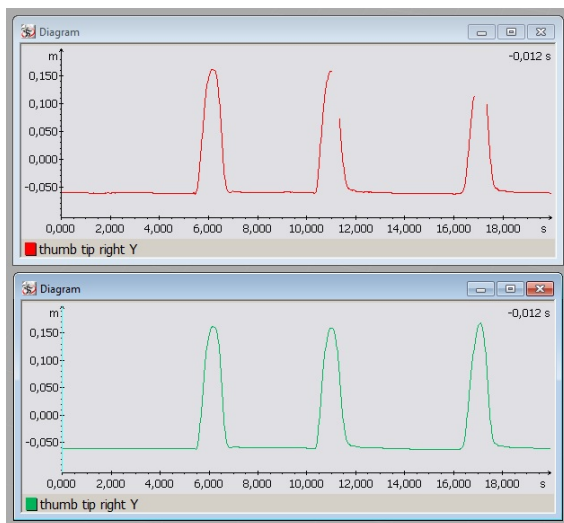


Figure 6.4: Example of the spline interpolation: original data (top) and interpolated data (bottom) (from participant n° 6, 2nd run, three trials, thumb tip Y-coordinate).

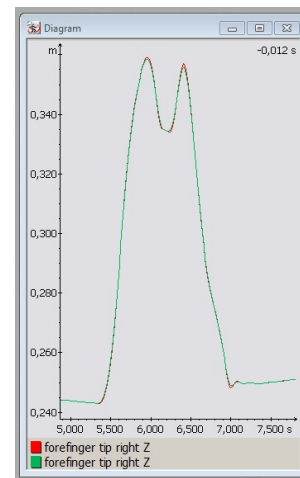
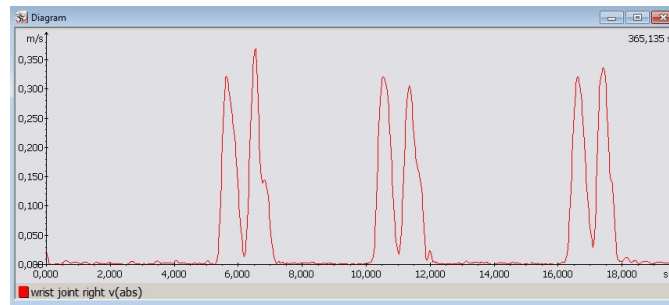
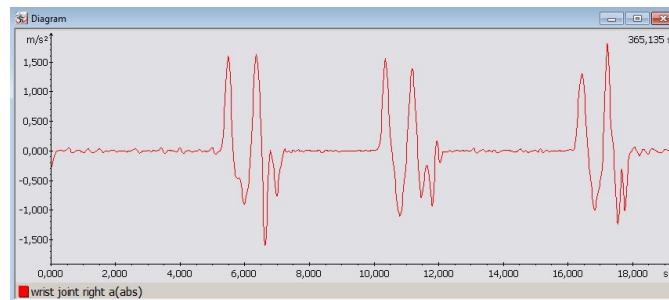


Figure 6.5: Example of the first-order low-pass filter with a cut-off frequency of 8 Hz: interpolated data (red) and filtered data (green) (from participant n° 6, 2nd run, one trial, forefinger tip Z-coordinate).

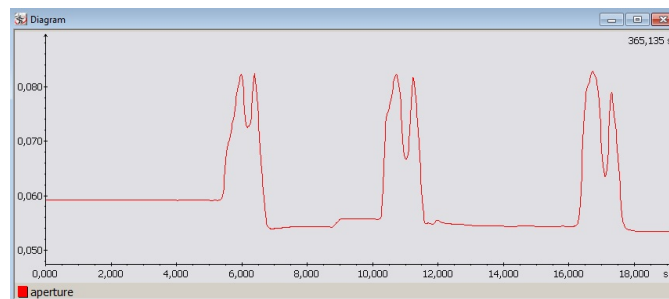
Then the 4 kinematic quantities (wrist absolute velocity, wrist absolute acceleration, grip aperture and grip aperture absolute velocity) were derived. Some examples are shown in Figure 6.6.



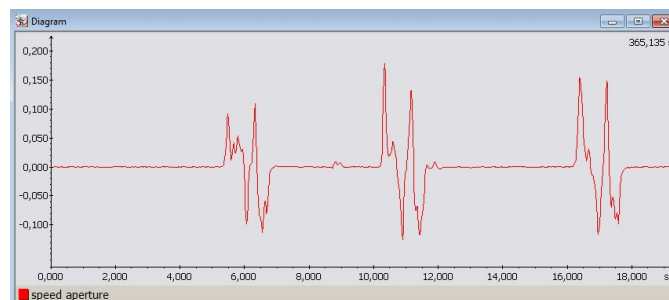
(a) wrist absolute velocity



(b) wrist absolute acceleration



(c) grip aperture



(d) grip aperture absolute velocity

Figure 6.6: Examples of the 4 kinematic quantities profiles (from participant n° 6, 2nd run, three trials).

6.4 Kinematic parameters extraction

From the kinematic quantities of each trial of each participant, a set of kinematic parameters were extracted. Some graphical examples of the results of this procedure are illustrated in Figure 6.7, Figure 6.8, Figure 6.9 and Figure 6.10.

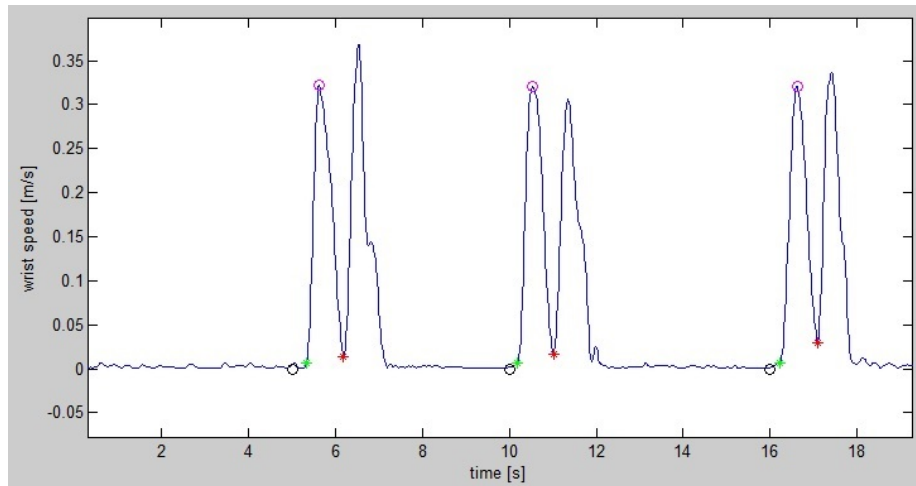


Figure 6.7: Examples of graphical representation of some kinematic parameters derived from the wrist absolute velocity: start of the movement (green star), end of the movement (red star), maximum wrist absolute velocity and its correspondent time (pink circle). The black circle corresponds to the acoustic tone time (from participant n° 6, 2nd run, three trials).

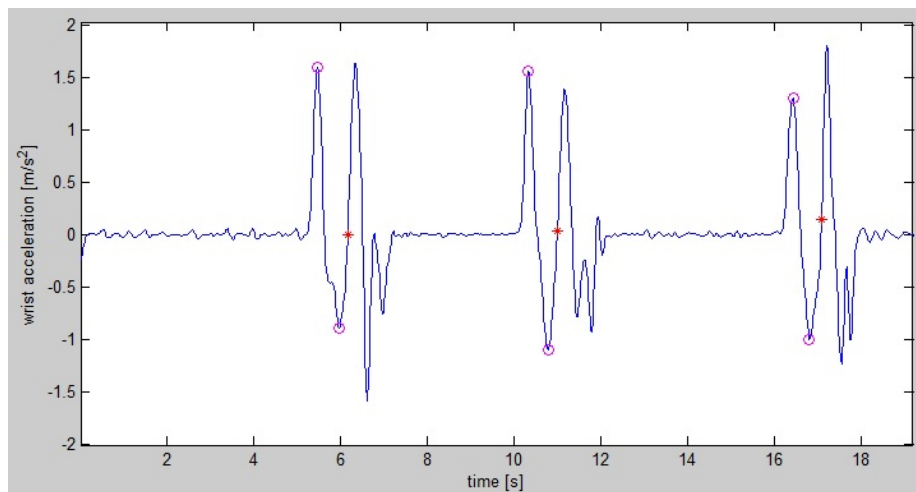


Figure 6.8: Examples of graphical representation of some kinematic parameters derived from the wrist absolute acceleration: end of the movement (red star), maximum wrist absolute acceleration and its correspondent time (pink circle), maximum wrist absolute deceleration and its correspondent time (pink circle) (from participant n° 6, 2nd run, three trials).

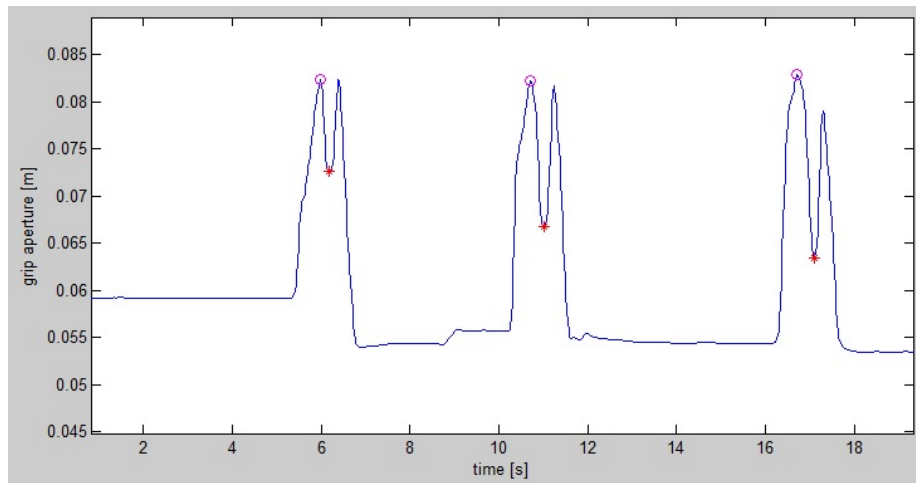


Figure 6.9: Examples of graphical representation of some kinematic parameters derived from the grip aperture: maximum grip aperture and its correspondent time (pink circle). The red star corresponds to the end of the movement (from participant n° 6, 2nd run, three trials).

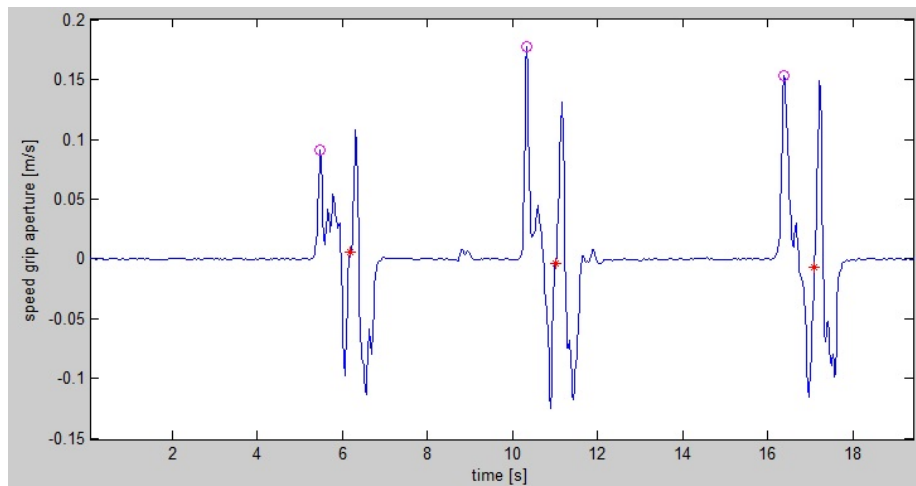


Figure 6.10: Examples of graphical representation of some kinematic parameters derived from the grip aperture absolute velocity: end of the movement (red star), maximum grip aperture absolute velocity and its correspondent time (pink circle) (from participant n° 6, 2nd run, three trials).

Then the mean of all the trials for the maximum wrist absolute velocity (*parameter 4*), the maximum grip aperture (*parameter 6*), the maximum grip aperture absolute velocity (*parameter 8*), the maximum wrist acceleration (*parameter 10*), the maximum wrist deceleration (*parameter 12*) and the movement time (*parameter 3*) for each participant was calculated (see Table 6.1).

	Sbj 1	Sbj 2	Sbj 3	Sbj 4	Sbj 5	Sbj 6	Sbj 7	Sbj 8	Sbj 9	Sbj 10
<i>Param 4</i>	0.3345	0.2144	0.1607	0.2273	0.1707	0.3308	0.3480	0.3925	0.2500	0.3636
<i>Param 6</i>	0.0920	0.1049	0.0950	0.0933	0.0912	0.0879	0.0950	0.1052	0.0961	0.1146
<i>Param 8</i>	0.1647	0.2268	0.0822	0.1620	0.1168	0.1412	0.2140	0.2447	0.1561	0.2522
<i>Param 10</i>	1.3702	1.2649	0.6738	0.8574	0.7056	1.2470	1.6355	1.9870	1.3327	1.6622
<i>Param 12</i>	-0.8572	-0.8059	-0.5329	-0.5932	-0.5713	-1.1831	-1.2880	-1.4707	-0.6641	-1.3019
<i>Param 3</i>	1.2234	0.8327	1.0504	1.1497	0.9570	0.9431	0.8250	0.7937	1.1254	0.8987

Table 6.1: Mean values of all the trials for the *parameters 3, 4, 6, 8, 10* and *12* for each participant.

6.5 Linear regression analysis

There were calculated the value of the slope of the fitted line and the determination coefficient r^2 for every pair of kinematic parameters. In Table 6.2 and in Table 6.3 are shown some examples of the values found for one participant.

	<i>Param 4</i>	<i>Param 6</i>	<i>Param 8</i>	<i>Param 10</i>	<i>Param 12</i>	<i>Param 3</i>
<i>Param 4</i>	1	0.0351	0.1562	7.3057	-3.7705	-0.7610
<i>Param 6</i>	-	1	4.3571	20.8160	-11.5706	-4.5423
<i>Param 8</i>	-	-	1	1.2951	-0.5782	-0.7969
<i>Param 10</i>	-	-	-	1	-0.3133	-0.0753
<i>Param 12</i>	-	-	-	-	1	0.0150
<i>Param 3</i>	-	-	-	-	-	1

Table 6.2: Examples of slope of the fitted line for every pair of parameters (from participant n° 9). Note that the matrix should be a symmetric matrix, but for simplicity only the upper part has been filled.

	<i>Param 4</i>	<i>Param 6</i>	<i>Param 8</i>	<i>Param 10</i>	<i>Param 12</i>	<i>Param 3</i>
<i>Param 4</i>	1	0.1001	0.0219	0.6518	0.5096	0.0505
<i>Param 6</i>	-	1	0.2099	0.0653	0.0592	0.0222
<i>Param 8</i>	-	-	1	0.0229	0.0134	0.0618
<i>Param 10</i>	-	-	-	1	0.2881	0.0405
<i>Param 12</i>	-	-	-	-	1	0.0005
<i>Param 3</i>	-	-	-	-	-	1

Table 6.3: Examples of determination coefficient r^2 for every pair of parameters (from participant n° 9). Note that the matrix should be a symmetric matrix, but for simplicity only the upper part has been filled.

The results collected into Table 6.2 and Table 6.3 were very similar for every participant and thus it is possible to deduce some general conclusions. In particular, from Table 6.3 it can be noticed that:

- there is a significant correlation between the *parameters 4* and *10* ($r^2 = 0.6518$) and between the *parameters 4* and *12* ($r^2 = 0.5096$)
- there is a moderate correlation between the *parameters 6* and *8* ($r^2 = 0.2099$) and between the *parameters 10* and *12* ($r^2 = 0.2881$)
- there is no significant correlation between all the other pairs of parameters ($r^2 \simeq 0$)

In Figure 6.11, the graphical representation of the regression line of the 4 pairs of parameters that demonstrated a higher linear correlation (*parameters 4* & *10*, *parameters 4* & *12*, *parameters 6* & *8* and *parameters 10* & *12*) for one participant are illustrated.

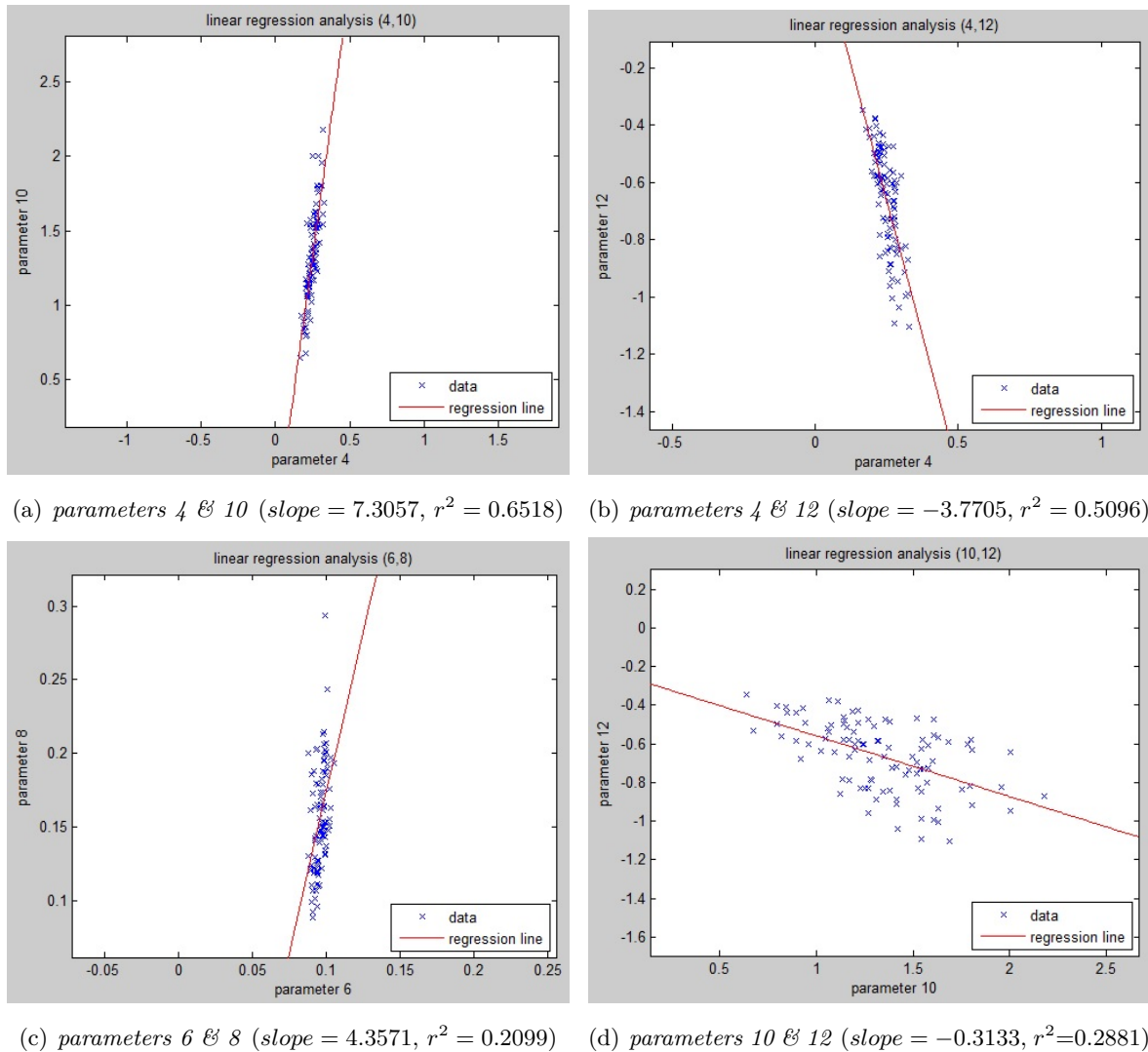


Figure 6.11: Examples of graphical representation of the regression line of the 4 pairs of parameters that demonstrated a higher linear correlation (from participant n° 9).

In Table 6.4, the determination coefficients r^2 of the 4 pairs of parameters that demonstrated a higher linear correlation (*parameters 4 & 10*, *parameters 4 & 12*, *parameters 6 & 8* and *parameters 10 & 12*) for each participant are shown.

	Sbj 1	Sbj 2	Sbj 3	Sbj 4	Sbj 5	Sbj 6	Sbj 7	Sbj 8	Sbj 9	Sbj 10
r^2 (4,10)	0.4859	0.8134	0.4788	0.4863	0.3677	0.8936	0.6432	0.2246	0.6518	0.4640
r^2 (4,12)	0.4435	0.5122	0.2666	0.2140	0.2725	0.8779	0.4253	0.5343	0.5096	0.5353
r^2 (6,8)	0.1365	0.1955	0.3334	0.4563	0.1647	0.4084	0.2918	0.3243	0.2099	0.1947
r^2 (10,12)	0.2413	0.4046	0.2695	0.0922	0.0398	0.8232	0.1253	0.0955	0.2881	0.1131

Table 6.4: Determination coefficients r^2 between the *parameters 4 & 10*, *parameters 4 & 12*, *parameters 6 & 8* and *parameters 10 & 12* of each participant.

6.6 Kinematic regressors selection

The results obtained from the linear regression analysis between the *parameters 4 & 10*, *parameters 4 & 12* and *parameters 10 & 12* mean that the *parameters 4*, *10* and *12* (i.e. the maximum wrist absolute velocity, the maximum wrist acceleration and the maximum wrist deceleration) are dependent on each other. For this reason, it was chosen to perform the correlation analysis with the BOLD signal using only one parameter of these three, i.e. the maximum wrist absolute velocity.

The results obtained from the linear regression analysis between the *parameters 6 & 8* mean that these two parameters (i.e. the maximum grip aperture and maximum grip aperture absolute velocity) are dependent on each other. However, because the degree of linear correlation was not so high and the two kinematic parameters have different meanings, it was chosen to maintain both the parameters for the consequent correlation analysis with the BOLD signal.

On the first time that the 1st level analysis was executed, the kinematic regressors were thus built using the movement time (*parameter 3*), the maximum wrist absolute velocity (*parameter 4*), the maximum grip aperture (*parameter 6*) and the maximum grip aperture absolute velocity (*parameter 8*) of each trial of each session for every participant. Only after this first time, the range of values of the estimated β parameter regarding the 4 kinematic regressors were checked from the β images. In Figure 6.12 are shown some examples of the β images.

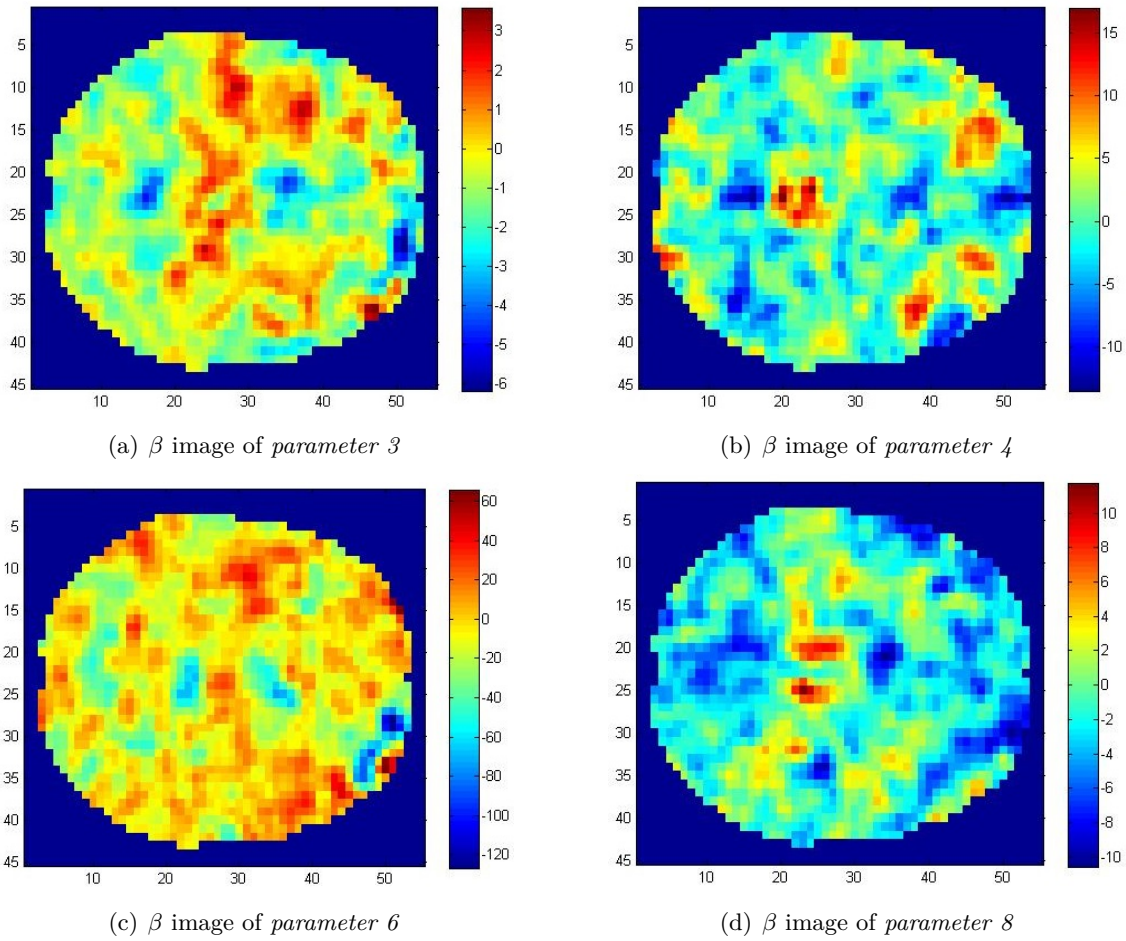
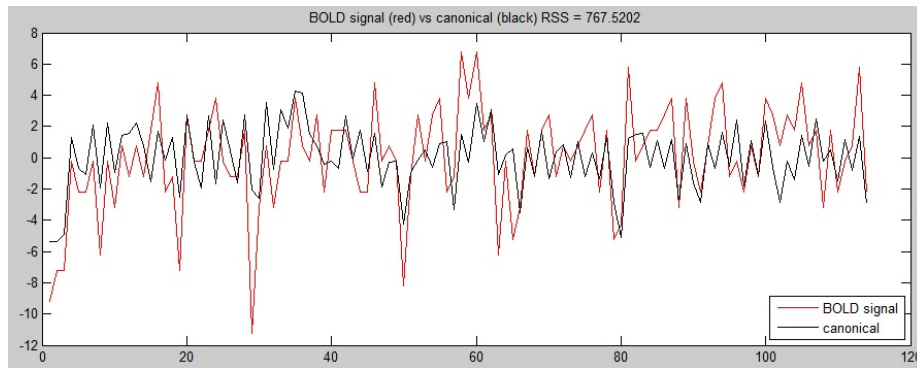


Figure 6.12: Examples of β images regarding the 4 kinematic regressors (from participant n° 1, slice 20).

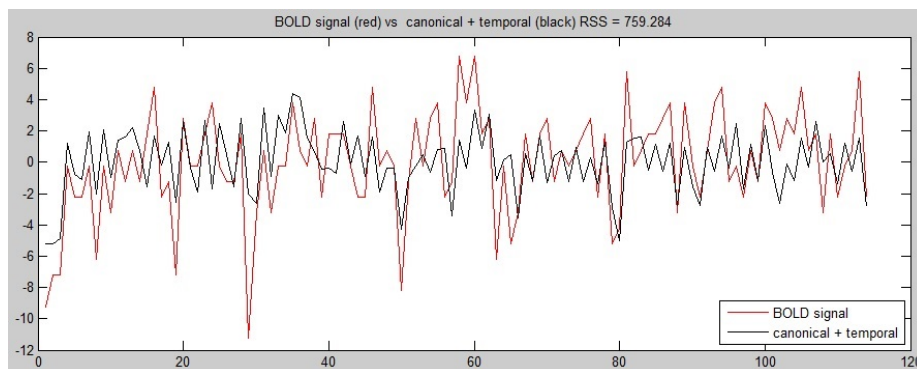
From the β images it can be noticed that the maximum value of the β parameter regarding the movement duration is around 3, regarding the maximum wrist absolute velocity is around 15, regarding the maximum grip aperture is around 60 and regarding the maximum grip aperture absolute velocity is around 10. A low β value means that the relative parameter does not give a significant contribution in the linear summation of the factors to reconstruct the BOLD signal. In this case, the β parameter regarding the movement duration has a pretty small range of values if compared to the others and therefore it can be concluded that the movement duration does not count that much in the linear summation. Moreover, the information regarding the duration of the movements is included in the model specification and so considering this parameter again as kinematic regressor may be redundant. Then, all the consequent analyses were performed without the movement duration (*parameter 3*) as kinematic regressor or as kinematic covariate.

6.7 Hemodynamic response model selection

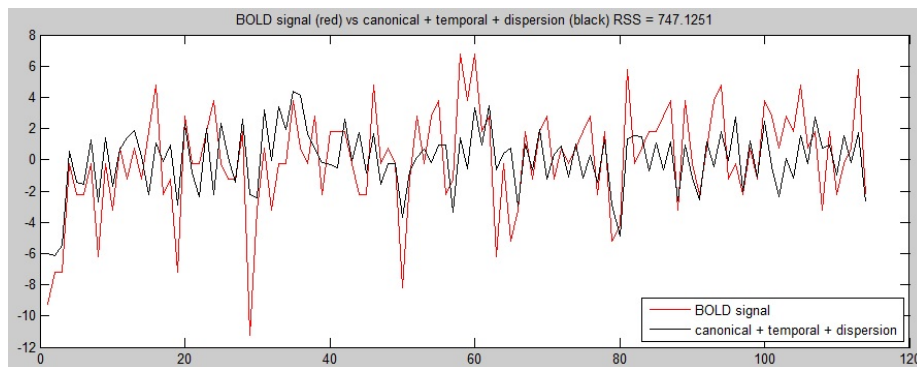
For each one of the three hemodynamic response models, i.e. *canonical* (model 1), *canonical temporal derivatives* (model 2) and *canonical dispersion derivatives* (model 3), the graphs of the model and of the BOLD signal were visually compared. In Figure 6.13 and in Figure 6.14 are shown the graphs of the BOLD signal and the three models of two different participants.



(a) BOLD signal and model 1

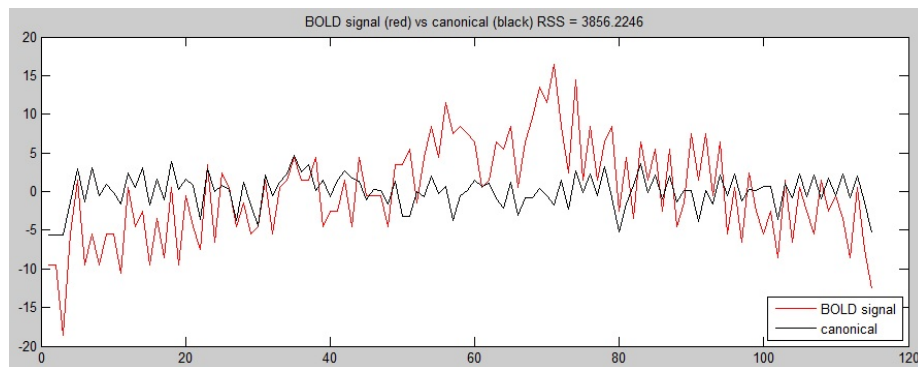


(b) BOLD signal and model 2

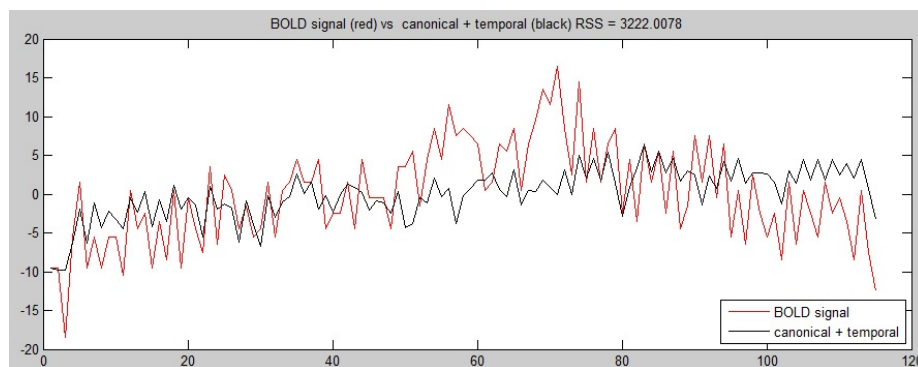


(c) BOLD signal and model 3

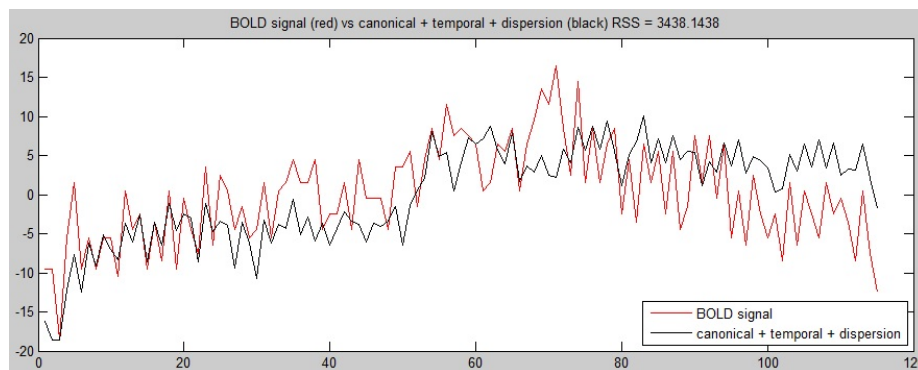
Figure 6.13: Graphical representation of the BOLD signal and the hemodynamic response function using the three models (from participant n° 1, session 1).



(a) BOLD signal and model 1



(b) BOLD signal and model 2



(c) BOLD signal and model 3

Figure 6.14: Graphical representation of the BOLD signal and the hemodynamic response function using the three models (from participant n° 9, session 1).

Most of the participants (7 participants) presented results similar to the participant n° 1 shown in Figure 6.13. It can be noticed that each one of the three models has a good fit to the experimental data. In general, the *model 2* can follow better the latency of the peak and the *model 3* can follow better the undershoot.

The other three participants (i.e. participant n° 5, n° 8 and n° 9) presented results similar to those shown in Figure 6.14. It can be noticed that anyone of the three models has not

a good fit to the experimental data. This happened because the BOLD signal has a significant drift that could be caused by scanner instabilities, spontaneous fluctuation in brain metabolism and physiology or physiologic noise from systemic sources such as cardiac and respiratory cycles [73].

The Residual Sum of Squares (RSS) of each model for every participant are collected in Table 6.5.

RSS	model 1	model 2	model 3
Sbj 1	767	759	747
Sbj 2	1766	1693	1864
Sbj 3	1250	1274	1293
Sbj 4	5502	5474	5541
Sbj 5	3117	3137	2540
Sbj 6	3234	3121	3125
Sbj 7	2551	2870	2591
Sbj 8	8233	8309	3811
Sbj 9	3856	3222	3438
Sbj 10	926	930	910

Table 6.5: Residual Sum of Squares (RSS) using the canonical function (model 1), the canonical temporal derivatives function (model 2) and the canonical dispersion derivatives function (model 3).

Considering the RSS, the *model 1* is to be preferred for participants n° 3 and n° 7, the *model 2* is to be preferred for participants n° 2, n° 4, n° 6 and n° 9 and the *model 3* is to be preferred for participants n° 1, n° 5, n° 8 and n° 10.

The Akaike Information Criterion coefficient (AIC) of each model for every participant are collected in Table 6.6.

AIC	model 1	model 2	model 3
Sbj 1	759	760	760
Sbj 2	854	851	864
Sbj 3	814	819	822
Sbj 4	983	985	988
Sbj 5	919	921	899
Sbj 6	923	921	923
Sbj 7	896	911	902
Sbj 8	1029	1032	946
Sbj 9	943	924	934
Sbj 10	780	783	782

Table 6.6: Akaike Information Criterion (AIC) using the canonical function (model 1), the canonical temporal derivatives function (model 2) and the canonical dispersion derivatives function (model 3).

Considering the AIC, the *model 1* is to be preferred for participants n° 1, n° 3, n° 4, n° 7 and n° 10, the *model 2* is to be preferred for participants n° 2, n° 6 and n° 9 and the *model 3* is to be preferred for participants n° 5 and n° 8.

It can be seen that, except for the participant n° 8, the differences among the three models are small because the values of both the RSS and the AIC are very similar within the same participant.

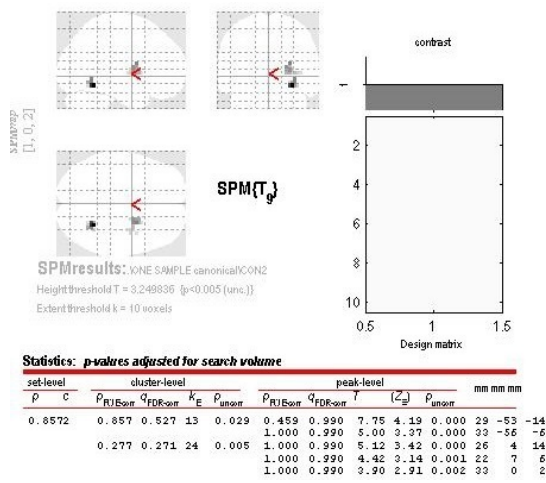
In the present thesis, the *canonical* model of the hemodynamic response (*model 1*) was identified as the best model because its AIC coefficient is the lowest in 5 out of 10 participants. That means that this model can deal with the trade-off between the goodness of fit and the complexity of the model.

6.8 2nd level approach selection

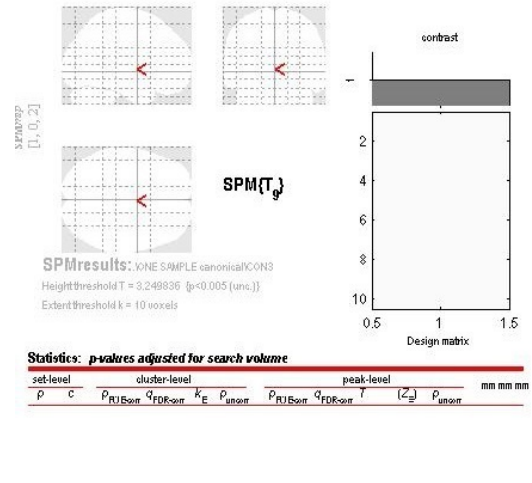
The SPMs obtained using *contrast 2*, *contrast 3*, *contrast 4*, *contrast 5*, *contrast 6* and *contrast 7* derived from all the strategies that adopted the *canonical* model of the hemodynamic response (i.e. *strategy I*, *strategy IV* and *strategy VII*) are illustrated in Figure 6.15, in Figure 6.16 and in Figure 6.17 respectively.

From each one of these SPMs, the anatomical correspondences of the biggest clusters was derived from their brain coordinates. It can be noticed that none of these brain areas has a significant physiological meaning because they belong to the white matter or to areas not included in the traditional reach-to-grasp activation pattern. Moreover, many SPMs show no suprathreshold clusters, that means that no voxels survived to the thresholding. In order to have more extended areas, one possibility could be to increase the p-value. However, increasing the p-value means also to increase the number of false positive results (type I error) and for this reason in this case the p-value was not changed. In conclusion, no significant correlation between the BOLD signal and the kinematics was found using these strategies.

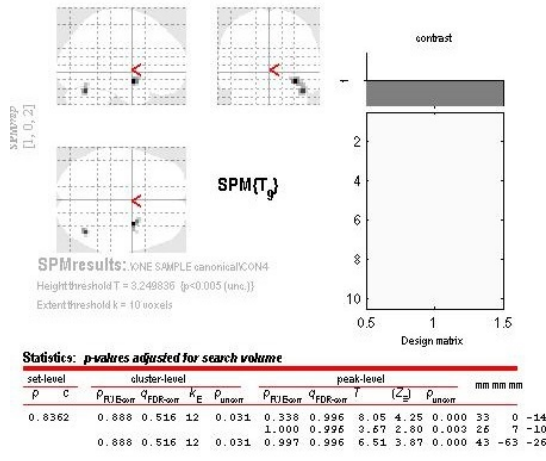
Other SPMs were then derived repeating the 2nd level analysis of all the three strategies (i.e. *strategy I*, *strategy IV* and *strategy VII*) using different groups of participants. As found in section 6.7, the BOLD signal of 3 participants presented a significant drift and therefore none of the models of the hemodynamic response could appropriately fit with the experimental data. This aspect could have compromised all the following results and for this reasons it was chosen to repeat the 2nd level analysis excluding the participant n° 9 (the one with the worst fit), excluding the participants n° 9 and n° 8 (the one with the second worst fit) and excluding the participants n° 9, n° 8 and n° 5 (the one with the third worst fit).



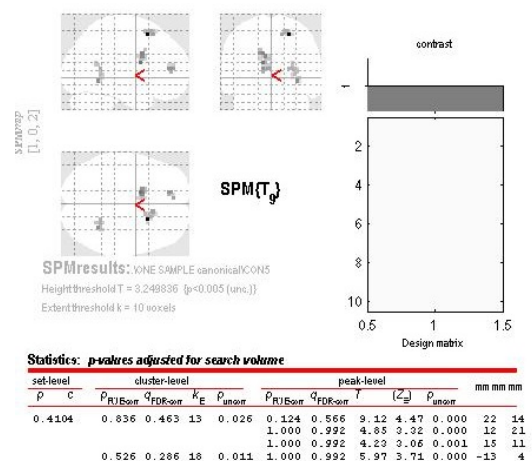
(a) contrast 2



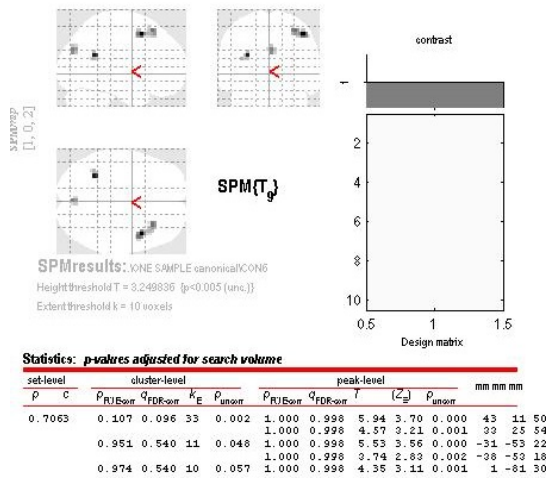
(b) contrast 3



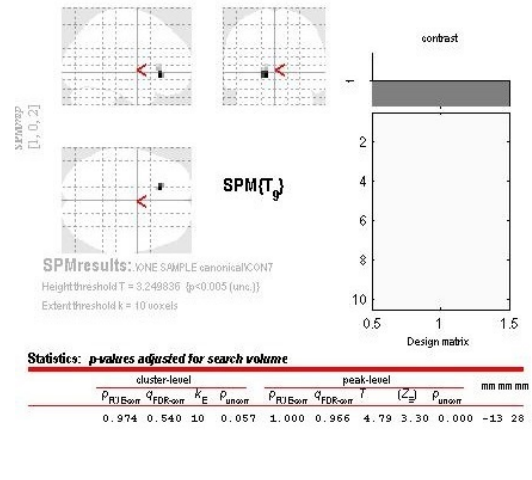
(c) contrast 4



(d) contrast 5

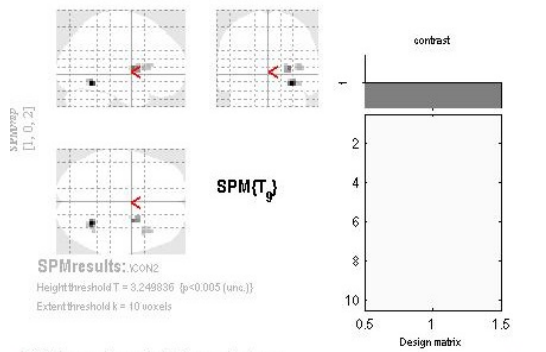


(e) contrast 6



(f) contrast 7

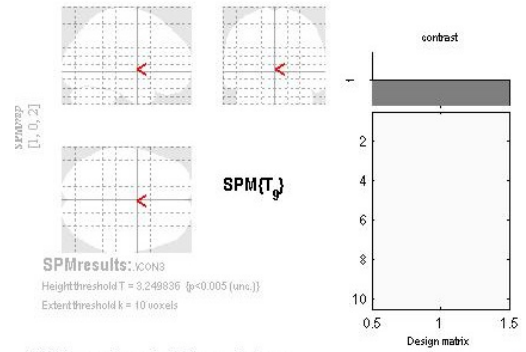
Figure 6.15: SPMs derived from strategy I.



Statistics: *p*-values adjusted for search volume

set-level		cluster-level				peak-level				mm mm mm			
ρ	c	$\rho_{\text{FWE}}^{\text{cluster}}$	$q_{\text{FDR}}^{\text{cluster}}$	k_E	ρ_{uncorr}	$\rho_{\text{FWE}}^{\text{peak}}$	$q_{\text{FDR}}^{\text{peak}}$	T	(Z_g)	ρ_{uncorr}			
0.3863		0.583	0.522	15	0.019	0.117	0.872	8.72	4.40	0.000	29	-56	-14
		1.000	0.978			1.000	0.978	2.92	2.92	0.002	40	-53	-14
		0.893	0.522	10	0.049	0.997	0.978	5.92	3.69	0.000	26	0	6
		0.640	0.522	11	0.040	1.000	0.978	4.25	3.07	0.001	40	14	6
		1.000	0.978			1.000	0.978	4.02	2.97	0.002	40	21	10

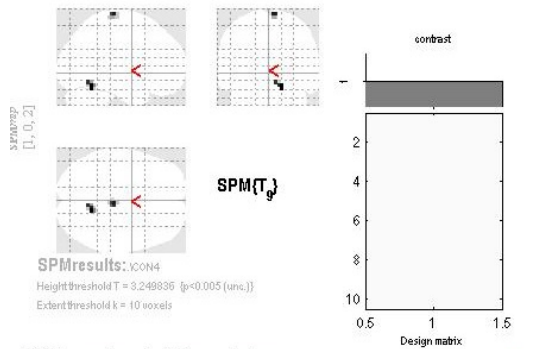
(a) contrast 2



Statistics: *p*-values adjusted for search volume

set-level		cluster-level				peak-level				mm mm mm			
ρ	c	$\rho_{\text{FWE}}^{\text{cluster}}$	$q_{\text{FDR}}^{\text{cluster}}$	k_E	ρ_{uncorr}	$\rho_{\text{FWE}}^{\text{peak}}$	$q_{\text{FDR}}^{\text{peak}}$	T	(Z_g)	ρ_{uncorr}			
0.3863		0.583	0.522	15	0.019	0.117	0.872	8.72	4.40	0.000	29	-56	-14
		1.000	0.978			1.000	0.978	2.92	2.92	0.002	40	-53	-14
		0.893	0.522	10	0.049	0.997	0.978	5.92	3.69	0.000	26	0	6
		0.640	0.522	11	0.040	1.000	0.978	4.25	3.07	0.001	40	14	6
		1.000	0.978			1.000	0.978	4.02	2.97	0.002	40	21	10

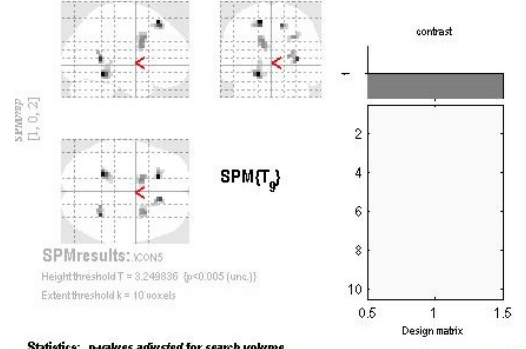
(b) contrast 3



Statistics: *p*-values adjusted for search volume

set-level		cluster-level				peak-level				mm mm mm			
ρ	c	$\rho_{\text{FWE}}^{\text{cluster}}$	$q_{\text{FDR}}^{\text{cluster}}$	k_E	ρ_{uncorr}	$\rho_{\text{FWE}}^{\text{peak}}$	$q_{\text{FDR}}^{\text{peak}}$	T	(Z_g)	ρ_{uncorr}			
0.6122		0.814	0.506	11	0.034	1.000	0.902	5.36	3.51	0.000	15	-56	-22
		1.000	0.902			1.000	0.902	4.88	3.33	0.000	8	-60	-14
		0.814	0.506	11	0.034	1.000	0.902	5.05	3.39	0.000	5	-25	74

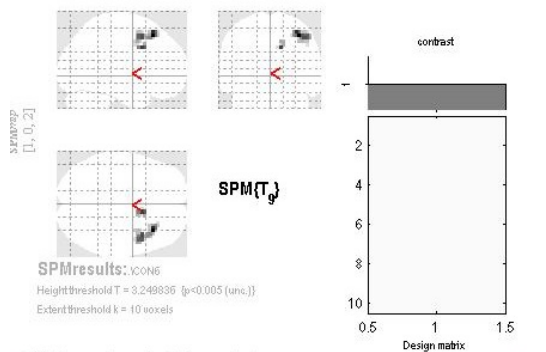
(c) contrast 4



Statistics: *p*-values adjusted for search volume

set-level		cluster-level				peak-level				mm mm mm			
ρ	c	$\rho_{\text{FWE}}^{\text{cluster}}$	$q_{\text{FDR}}^{\text{cluster}}$	k_E	ρ_{uncorr}	$\rho_{\text{FWE}}^{\text{peak}}$	$q_{\text{FDR}}^{\text{peak}}$	T	(Z_g)	ρ_{uncorr}			
0.0196		0.677	0.255	15	0.023	0.138	0.787	8.17	4.28	0.000	-17	28	54
		0.101	0.096	27	0.002	0.270	0.787	7.86	4.21	0.000	-20	-46	-14
		1.000	0.992			1.000	0.992	2.64	2.78	0.002	-17	-35	2
		0.874	0.311	10	0.042	0.912	0.787	6.73	3.93	0.000	33	-49	6
		0.874	0.311	10	0.042	1.000	0.992	4.75	3.28	0.001	22	-49	10
		0.318	0.173	19	0.008	0.988	0.787	6.35	3.82	0.000	12	32	50
		0.539	0.233	15	0.016	1.000	0.992	5.09	3.41	0.000	-13	7	30
		1.000	0.992			1.000	0.992	5.03	3.39	0.000	29	11	34
		1.000	0.992			1.000	0.992	3.84	2.88	0.002	33	4	38

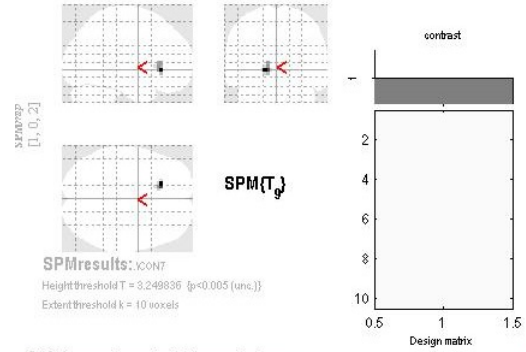
(d) contrast 5



Statistics: *p*-values adjusted for search volume

set-level		cluster-level				peak-level				mm mm mm			
ρ	c	$\rho_{\text{FWE}}^{\text{cluster}}$	$q_{\text{FDR}}^{\text{cluster}}$	k_E	ρ_{uncorr}	$\rho_{\text{FWE}}^{\text{peak}}$	$q_{\text{FDR}}^{\text{peak}}$	T	(Z_g)	ρ_{uncorr}			
0.7032		0.004	0.004	58	0.000	0.980	0.965	6.32	3.81	0.000	36	25	50
		1.000	0.965			1.000	0.965	5.16	3.43	0.000	43	11	46
		0.869	0.542	11	0.048	1.000	0.965	3.77	2.85	0.002	40	4	42
		1.000	0.965			1.000	0.965	5.37	3.51	0.000	12	11	34
		1.000	0.965			1.000	0.965	3.98	2.95	0.002	12	4	42

(e) contrast 6

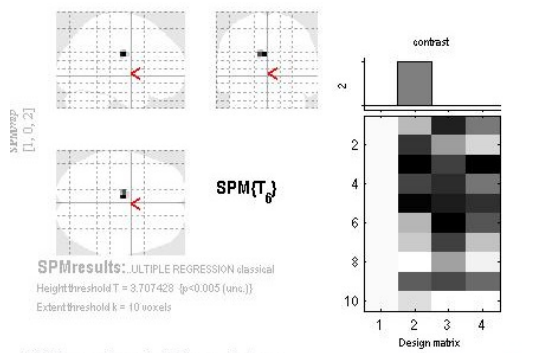


Statistics: *p*-values adjusted for search volume

set-level		cluster-level				peak-level				mm mm mm			
ρ	c	$\rho_{\text{FWE}}^{\text{cluster}}$	$q_{\text{FDR}}^{\text{cluster}}$	k_E	ρ_{uncorr}	$\rho_{\text{FWE}}^{\text{peak}}$	$q_{\text{FDR}}^{\text{peak}}$	T	(Z_g)	ρ_{uncorr}			
0.699		0.427	0.14	14	0.028	0.907	0.972	6.73	3.93	0.000	-17	28	-2

(f) contrast 7

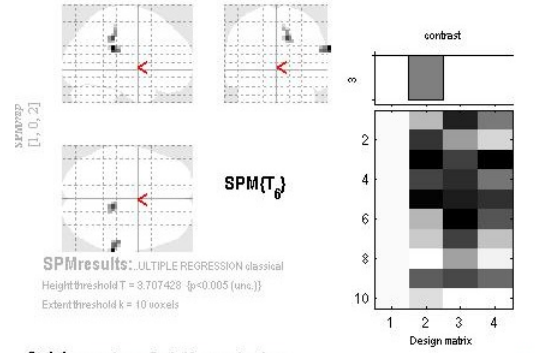
Figure 6.16: SPMs derived from strategy IV.



Statistics: *p*-values adjusted for search volume

cluster-level					peak-level					mm mm mm			
ρ	c	$\rho_{RJ\text{Bonf}}$	$q_{FDR\text{cor}}$	k_E	ρ_{uncorr}	$\rho_{RJ\text{Bonf}}$	$q_{FDR\text{cor}}$	t	(Z_{β})	ρ_{uncorr}			
0.854	0.549	12	0.050	0.533	0.801	10.26	4.06	0.000	-6	-11	26		

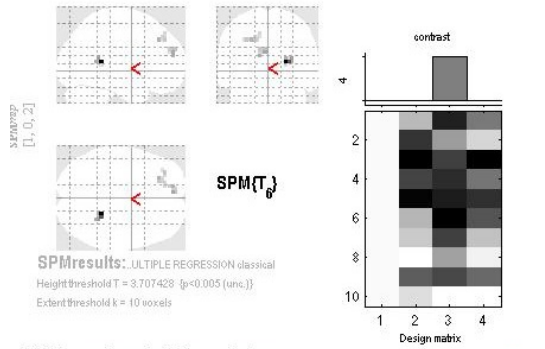
(a) contrast 2



Statistics: *p*-values adjusted for search volume

cluster-level					peak-level					mm mm mm			
ρ	c	$\rho_{RJ\text{Bonf}}$	$q_{FDR\text{cor}}$	k_E	ρ_{uncorr}	$\rho_{RJ\text{Bonf}}$	$q_{FDR\text{cor}}$	t	(Z_{β})	ρ_{uncorr}			
0.7532	0.640	0.557	16	0.027	1.000	0.999	7.22	3.57	0.000	68	-35	26	
					1.000	0.999	5.58	3.19	0.001	61	-32	22	
					1.000	0.999	6.03	3.31	0.000	12	-35	36	
					1.000	0.999	4.90	3.00	0.001	12	-32	46	
					1.000	0.999	4.47	2.86	0.002	19	-39	24	

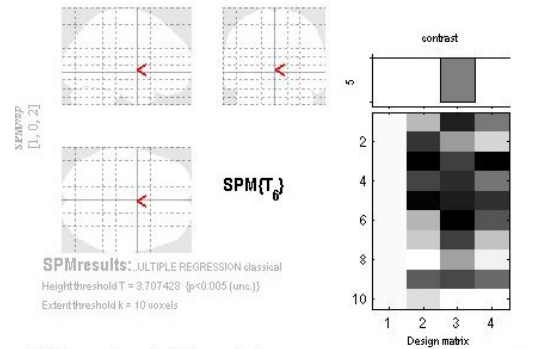
(b) contrast 3



Statistics: *p*-values adjusted for search volume

cluster-level					peak-level					mm mm mm						
ρ	c	$\rho_{RJ\text{Bonf}}$	$q_{FDR\text{cor}}$	k_E	ρ_{uncorr}	$\rho_{RJ\text{Bonf}}$	$q_{FDR\text{cor}}$	t	(Z_{β})	ρ_{uncorr}						
0.5093	0.933	0.565	10	0.070	0.974	0.998	9.41	3.94	0.000	22	-42	10				
					1.000	0.998	5.27	3.11	0.001	29	-46	14				
					0.897	0.565	11	0.059	1.000	0.998	5.12	3.07	0.001	-6	53	22
					1.000	0.998	4.94	3.01	0.001	-13	53	18				
					1.000	0.998	4.20	2.77	0.003	-13	49	26				
					1.000	0.998	4.94	2.99	0.001	-24	35	38				
					0.897	0.565	11	0.059	1.000	0.998	4.34	2.82	0.002	-31	42	38
					1.000	0.998	4.02	2.70	0.003	-17	42	38				

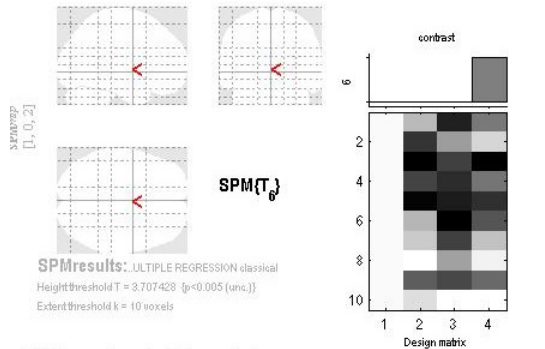
(c) contrast 4



Statistics: *p*-values adjusted for search volume

cluster-level					peak-level					mm mm mm			
ρ	c	$\rho_{RJ\text{Bonf}}$	$q_{FDR\text{cor}}$	k_E	ρ_{uncorr}	$\rho_{RJ\text{Bonf}}$	$q_{FDR\text{cor}}$	t	(Z_{β})	ρ_{uncorr}			

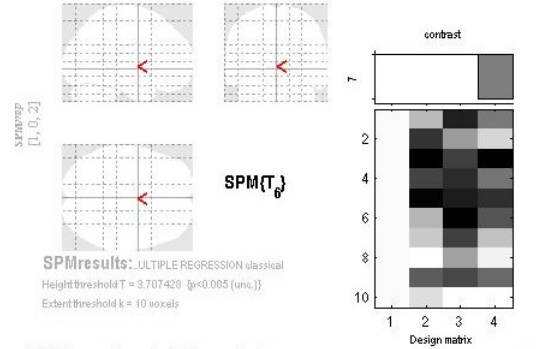
(d) contrast 5



Statistics: *p*-values adjusted for search volume

cluster-level					peak-level					mm mm mm			
ρ	c	$\rho_{RJ\text{Bonf}}$	$q_{FDR\text{cor}}$	k_E	ρ_{uncorr}	$\rho_{RJ\text{Bonf}}$	$q_{FDR\text{cor}}$	t	(Z_{β})	ρ_{uncorr}			

(e) contrast 6



Statistics: *p*-values adjusted for search volume

cluster-level					peak-level					mm mm mm			
ρ	c	$\rho_{RJ\text{Bonf}}$	$q_{FDR\text{cor}}$	k_E	ρ_{uncorr}	$\rho_{RJ\text{Bonf}}$	$q_{FDR\text{cor}}$	t	(Z_{β})	ρ_{uncorr}			

(f) contrast 7

Figure 6.17: SPMs derived from strategy VII.

Using the *strategy IV* with the 2nd level analysis conducted excluding the participant n° 9, it was found a significant correlation in the SPM obtained from *contrast 4*, i.e. from the test of the positive effect of the maximum grip aperture (see Figure 6.18). The most extended brain areas have an anatomical correspondence with the *inferior frontal gyrus triangularis* that corresponds to the ventrolateral Premotor Cortex (vPMC). The other smaller areas found are of no interest and do not appear if an higher voxels extent threshold (e.g. equals to 15) is chosen (see Figure 6.19).

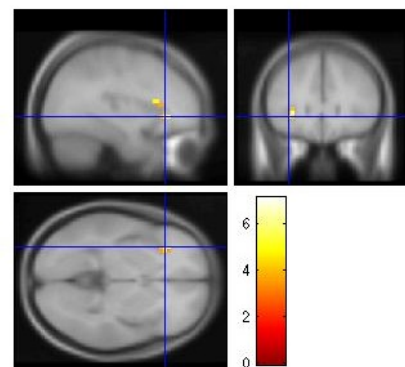
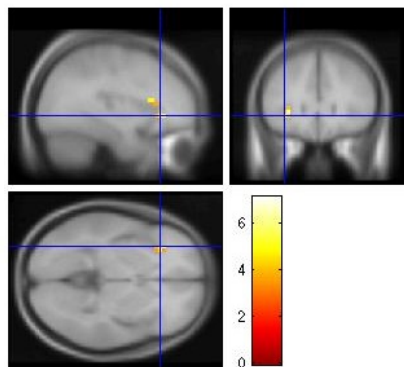
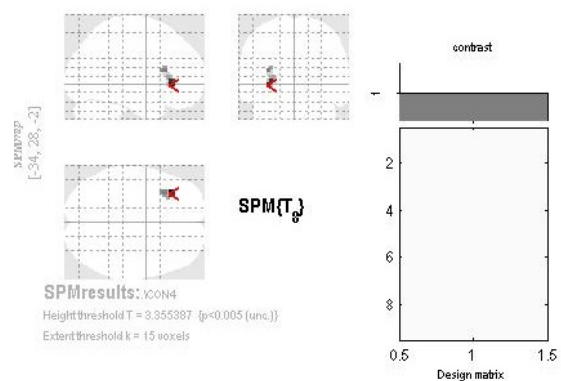
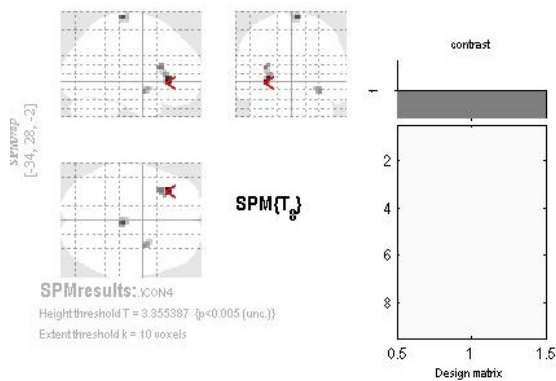


Figure 6.18: SPM obtained from *contrast 4* using the *strategy IV* without the participant n° 9 (p-value=0.005 and voxel extent threshold=10).

Figure 6.19: SPM obtained from *contrast 4* using the *strategy IV* without the participant n° 9 (p-value=0.005 and voxel extent threshold=15).

The results found in Figure 6.18 and in Figure 6.19 mean that there is a positive correlation between the BOLD signal and the maximum grip aperture in the vPMC. The bigger the maximum grip aperture, the higher the neuronal activity in the vPMC. This is consistent with the literature because it has been proposed that the vPMC has a role in selecting the specific "motor prototype" for the reach-to-grasp movement, such how the object should be reached, the goal of the action or the temporal segmentation of the action [25] [36]. The efficiency of the reach-to-grasp movement is higher when the maximum grip aperture is bigger because there is a more relevant neuronal activity in the brain area designated to select the best type of movement to be performed.

The other SPMs derived from the other contrasts do not show significant results because the resultant areas belong to the white matter or are not included in the traditional reach-to-grasp activation pattern. Moreover, also in these cases, many SPMs show no suprathreshold clusters.

Excluding only the participant n° 9 from the 2nd level analysis has been demonstrated to be the best choice probably due to the fact that the drift detected in the BOLD signal of the other two participants (i.e. participants n° 5 and n° 8) was not so severe to affect the results of the analysis.

In conclusion, among *strategy I*, *strategy IV* and *strategy VII*, the *strategy IV* proved to be the best. The *strategy I* did not show meaningful results probably because significant differences in the values of the non-normalized regressors could be solely due to a different dispersion of the data, i.e. to a different standard deviation. The normalization of the regressors allows indeed more accurate further calculations and comparisons. The *strategy VII* did not show significant results probably because the information about the time of the extracted parameters was completely lost when the temporal mean was calculated in order to build the covariates.

Chapter 7

Conclusions

Reaching, grasping and manipulating an object are actions that require multiple visuomotor transformation which imply the ability to transform the visual features of the object in the appropriate hand configuration and the capacity to perform and control the hand and the fingers movement. A significant number of studies [43]-[54] suggest that in humans, like in monkeys, reach-to-grasp movements involve a large network of interconnected structures in the parietal and frontal lobes, in particular the primary motor cortex (M1), the ventral and dorsal sectors of the premotor cortex (vPMC and dPMC respectively) and the anterior intraparietal area (AIP). Nevertheless, how the neural control systems interact with the complex biomechanics of moving arms remains an open question.

The aim of the present thesis was to investigate the correlation between the human brain activity recorded by fMRI technique and the kinematic signal coming from the moving arm during the reach-to-grasp movement. The goal to capture the complex natural cerebral activity required a multimodal approach which take benefits from all the different techniques used.

In the present study, a motion capture system integrated with the MR scanner (1.5 T) was used. The simultaneous acquisition of the videos recorded from two different cameras positioned in front of the MR scanner and the fMRI data allowed to obtain at the same time information regarding the kinematics of the moving arm and the neuronal activity coming from the BOLD signal.

Ten healthy right-handed volunteers participated in the fMRI experiments. On their right hand, 3 passive reflective markers were fixed on the wrist, on the thumb tip and on the forefinger tip. Participants were requested to grasp a small wooden sphere of 2 *cm* diameter using a precision grip every time that an acoustic tone was delivered through MR-compatible headphones. The entire experiment consisted of two sessions of 50 trials each. A mixed design was adopted with variable interstimulus interval (ISI) that varied from 5 to 10 seconds.

The kinematic data processing was performed off-line using the software Simi Motion©. From the movement videos it was possible to calculate the 3D coordinates of the 3 markers over time and from them to derive 4 kinematics quantities: the wrist absolute velocity, the wrist absolute acceleration, the grip aperture (thumb tip-forefinger tip distance) and the grip aperture absolute velocity. Then, a set of 13 kinematic parameters were extracted from the kinematic quantities and a linear regression analysis was performed in order to select only those to insert in the following analyses. The result of the regression analysis identified the maximum wrist absolute velocity, the maximum grip aperture and maximum grip aperture absolute velocity as the most significant kinematic parameters to be tested for the correlation with the BOLD signal.

The data analysis was executed combining the information provided from both the techniques, i.e. from the movement videos and the fMRI images. The fMRI images were pre-processed with the realignment, the segmentation, the coregistration, the normalization and the smoothing. Then, a within-subject analysis (1st level analysis) and a between-subject analysis (2nd level analysis) were implemented following some different strategies. Two main methods were tested: the first one consisted of using the kinematic information at the 1st level and the second one of using them at the 2nd level. In the first case, kinematic regressors were inserted in the 1st level analysis and then at the 2nd level a "one-sample t-test" was applied (this process was repeated also using normalized kinematic regressors). In the second case, the 1st level analysis was done without kinematic regressors and at the 2nd level the kinematic information were included as covariates in the "multiple regression" approach. Moreover, these analyses were replicated for all the three canonical models of the hemodynamic response function, i.e. canonical, canonical temporal derivatives and canonical dispersion derivatives.

Statistical analysis of fMRI data used the General Linear Model (GLM) approach. Its implementation needed the specification of the GLM design matrix, the estimation of the GLM parameters and the interrogation of results using contrast vectors to produce Statistical Parametric Maps (SPMs). The contrasts vectors tested were the positive effect of the grasping condition (main effect) and the positive and negative effects of the 3 kinematic parameters selected from the linear regression analysis.

The choice of the best model of the hemodynamic response was done comparing the Akaike Information Criterion (AIC) coefficient of all the 3 models. The model of the canonical response was selected as the best one because of its lowest AIC in half of the participants. All the analyses were then repeated excluding one participant due to the presence of a significant drift in his BOLD signal. Finally, the SPMs obtained from all the strategies that adopted the canonical model of the hemodynamic response were compared.

The results showed that there is a positive correlation between the BOLD signal and the maximum grip aperture in the vPMC. The bigger the maximum grip aperture, the higher the neuronal activity in the vPMC. This is consistent with the literature because it has been proposed that the vPMC has a role in selecting the specific "motor prototype" for the reach-to-grasp movement, such how the object should be reached, the goal of the action or the temporal segmentation of the action [25] [36]. The efficiency of the reach-to-grasp movement is higher when the maximum grip aperture is bigger because there is a more relevant neuronal activity in the brain area designated to select the best type of movement to be performed.

Further studies can be done in order to specify better the kind of interaction between the kinematics and the BOLD signal. Starting from the results obtained from the 2nd level analysis, it could be interesting to implement a parametric modulation to modulate the model of the hemodynamic response on each trial in a different way. Moreover, a large number of participants could help to have more significant statistical results. Finally, BOLD signals with drifts could be decomposed using the Independent Component Analysis (ICA) approach in order to avoid the exclusion of the participants who presented that problem.

Bibliography

- [1] Jeannerod. The timing of natural prehension movements. *J. Mot. Behav.*, 16:235–254, 1984.
- [2] Castiello. The neuroscience of grasping. *Nat. Rev. Neurosci.*, 6:726–736, 2005.
- [3] Haines. The anatomy of the hand of certain insectivores. *Proceedings of the Zoological Society of London*, 125:761–777, 1955.
- [4] Stern and Susman. The locomotor anatomy of the australopithecus afarensis. *American Journal of Physical Anthropology*, 60:279–317, 1987.
- [5] Napier. Prehensility and opposability in the hands of primates. *Symp. Zool. Soc.*, 5:115–132, 1961.
- [6] Zoia et al. Evidence of early development of action planning in the human foetus: a kinematic study. *Experimental Brain Research*, 176:217–226, 2007.
- [7] Woodward and Sommerville. Twelve-month-old infants interpret action in context. *Psychological Science*, 11:73–77, 2000.
- [8] Gordon et al. Visual size cues in the programming of manipulative forces during precision grip. *Experimental Brain Research*, 83:477–482., 1991.
- [9] Johansson. *Sensory Guidance of Movement*. New York: John Wiley, 1998.
- [10] Forssberg et al. Development of human precision grip. ii. anticipatory control of isometric forces targeted for object’s weight. *Experimental Brain Research*, 90:393–398, 1992.
- [11] Zoia et al. A comparison of the reach to grasp movement between children and adults: a kinematic study. *Developmental Neuropsychology*, 30:719–738, 2006.
- [12] Jeannerod. *Attention and Performance IX*. Erlbaum, Hillsdale, 1981.
- [13] Smeets and Brenner. A new view on grasping. *Mot. Cont.*, 3:237–271, 1999.
- [14] Marteniuk et al. Functional relationship between grasp and transport component in prehension task. *Human Movement Science*, 9:149–176, 1990.

-
- [15] Gentilucci et al. Influence of different types of grasping on the transport component of prehension movements. *Neuropsychologia*, 29:361–378, 1991.
- [16] Cohen and Rosenbaum. Where grasps are made reveals how grasps are planned: generation and recall of motor plans. *Exp. Brain Res.*, 157:486–495, 2004.
- [17] Ansuini et al. Effects of end-goal on hand shaping. *J. Neurophysiol.*, 95:2456–2465, 2006.
- [18] Mason, Theverapperuma, Hendrix, and Ebner. Monkey hand postural synergies during reach-to-grasp in the absence of vision of the hand and object. *J. Neurophysiol.*, 91:2826–2837, 2004.
- [19] Faugier Grimaud et al. Effects of posterior parietal lesions on visually guided behaviour in monkeys. *Neuropsychologia*, 16:151–168, 1978.
- [20] Roy et al. Hand kinematics during reaching and grasping in the macaque monkey. *Behav. Brain Res.*, 117:75–82, 2000.
- [21] Christel and Billard. Comparison between macaques’ and humans’ kinematics of prehension: the role of morphological differences and control mechanisms. *Behav. Brain Res.*, 131:169–184, 2002.
- [22] Napier. Studies of the hands of living primates. *Proc. Zool. Soc.*, 134:647–657, 1960.
- [23] De Sanctis. *Reach to grasp movement: a simultaneous recording approach*. PhD thesis, University of Padova, 2014.
- [24] Raos et al. Functional properties of grasping-related neurons in the dorsal premotor area f2 of the macaque monkey. *J. Neurophysiol.*, 92:1990–2002, 2004.
- [25] Rizzolatti et al. Functional organization of inferior area 6 in the macaque monkey. ii. area f5 and the control of distal movements. *Exp. Brain Res.*, 71:491–507, 1988.
- [26] Lawrence and Hopkins. The development of motor control in the rhesus monkey: evidence concerning the role of corticomotoneuronal connetions. *Brain*, 99:235–254, 1976.
- [27] Muir and Lemon. Corticospinal neurons with a special role in precision grip. *Brain Res.*, 261:312–316, 1983.
- [28] Gibson et al. *Insights into the Reach to Grasp Movement*. Amsterdam: Elsevier Science., 1994.
- [29] Smith and Boubonnais. Neural activity in cerebellar cortex related to control of prehensile force. *J. Neurophysiol.*, 45:286–303, 1981.

-
- [30] Jeannerod et al. Grasping object: the cortical mechanisms of visuomotor transformation. *Trends Neurosci.*, 18:314–320, 1995.
- [31] Castiello and Begliomini. The cortical control of visually guided grasping. *Neuroscientist*, 14(2):157–170, 2008.
- [32] Fagg and Arbib. Modeling parietal-premotor interactions in primate control of grasping. *Neural Netw*, 11:1277–1303, 1998.
- [33] Rizzolatti and Luppino. The cortical motor system. *Neuron*, 31:889–901, 2001.
- [34] Brodmann. Comparative localization studies in the brain cortex, its fundamentals represented on the basis of its cellular architecture. *Leipzig, JA Barth*, 1909.
- [35] Dum and Stick. The origin of the corticospinal projections from the premotor areas in the frontal lobe. *J. Neurosci.*, 11:667–689, 1991.
- [36] Grèzes et al. Does perception of biological motion rely on specific brain region? *Neuroimage*, 13:775–785, 2001.
- [37] Wise et al. The premotor cortex and nonstandard sensorimotor mapping. *Canadian Journal of Physiological Pharmacology*, 74:469–482, 1996.
- [38] Passingham. Functional specialization of the supplementary motor area in the monkeys and humans. *Adv. Neurol.*, 70:105–116, 1996.
- [39] Picard and Stick. Imaging the premotor areas. *Curr. Opin. Neurobiol.*, 11:663–672, 2001.
- [40] Crossman. Functional anatomy of movement disorders. *Journal of Anatomy*, 196:519–525, 2000.
- [41] Holsapple et al. The origin of thalamic inputs to the "hand" representation in the primary motor cortex. *The Journal of Neuroscience*, 11:2644–2654, 1991.
- [42] Doyon et al. Distinct contribution of the cortico-striatal and cortico-cerebellar systems to motor skill learning. *Neuropsychologia*, 41:252–262, 2003.
- [43] Binkofski et al. Human anterior intraparietal area subserves prehension a combined lesion and functional mri activation study. *Neurology*, 50:1253–1259, 1998.
- [44] Culham. Human brain imaging reveals a parietal area specialized for grasping. *Attention and performance XX: functional neuroimaging of human cognition*, 2004.
- [45] James et al. Ventral occipital lesions impair object recognition but not object-directed grasping: an fmri study. *Brain*, 126:2463–2475, 2003.

- [46] Grèzes et al. Activations related to ‘mirror’ and ‘canonical’ neurons in the human brain: an fmri study. *Neuroimage*, 18:928–937, 2003.
- [47] Begliomini et al. Differential cortical activity for precision and whole-hand visually guided grasping in humans. *Eur. J. Neurosci.*, 25:1245–1252., 2007.
- [48] Begliomini et al. Comparing natural and constrained movements: new insights into the visuomotor control of grasping. 2(10), e1108. *PLoS One*, 2(10):e1108, 2007.
- [49] Ehrsson et al. Cortical activity in precision-versus power-grip tasks: an fmri study. *J. Neurophysiol.*, 83:528–536, 2000.
- [50] Cavina-Pratesi et al. fmri reveals the neural substrates of arm transport and grip formation in reach to grasp actions in humans. *The Journal of Neuroscience*, 30:10306–10323, 2010.
- [51] Glover et al. Distinct cortical networks support the planning and online control of reaching-to-grasp in humans. *Eur. J. Neurosci.*, 35:909–915, 2012.
- [52] Konen et al. Functional organization of human posterior parietal cortex: grasping-and reaching-related activations relative to topographically organized cortex. *J. Neurophysiol.*, 109:2897–2908, 2013.
- [53] Grafton. The cognitive neuroscience of prehension: recent developments. *Exp. Brain Res.*, 204:475–491, 2010.
- [54] Tunik et al. Basal ganglia contribution to the initiation of corrective submovements. *Neuroimage*, 47:1757–1766, 2009.
- [55] De Sanctis et al. Co-registering kinematics and evoked related potentials during visually guided reach to grasp movements. *PloS One*, 8:e65508, 2013.
- [56] Huettel, Song, and McCarthy. *Functional Magnetic Resonance Imaging*. Sinauer Associates, 2004.
- [57] *Begliomini. Slides of "Neuroimmagini funzionali", 2014-2015.*
- [58] Arthurs et al. How well do we understand the neural origins of the fmri bold signal? *Trends Neurosci.*, 25(1):27–31, 2002.
- [59] *Bertoldo. Slides of "Neuroingegneria", 2013-2014.*
- [60] Girotto. Studio di correlazione tra fmri e analisi del cammino per la valutazione della riabilitazione con biofeedback in pazienti post ictus. Master’s thesis, University of Padova, 2011.

-
- [61] Friston. *SPM manual*.
- [62] Friston et al. *Statistical parametric mapping: the analysis of functional brain images*. Elsevier, 2007.
- [63] Menache. Understanding motion capture for computer animation and video games. *Los Altos, CA*, 1999.
- [64] Mantoan. Underwater gait analysis: a markerless approach. Master's thesis, University of Padova, 2011.
- [65] Ceseracciu. *New frontiers of markerless motion capture: application to swim biomechanics and gait analysis*. PhD thesis, University of Padova, 2011.
- [66] Abdel-Aziz and Karara. Direct linear transformation into object space coordinates in close-range photogrammetry. *Proc ASP Symp Close Range Photogram - Urbana - IL*, 1971.
- [67] Dapena et al. Three-dimensional cinematography with control object of unknown shape. *J Biomech*, 15:11-19, 1982.
- [68] Cappello, Cappozzo, and di Prampero. *Bioingegneria della postura e del movimento*. Pàtron Editore, 2007.
- [69] Zhang. A flexible new technique for camera calibration. *IEEE Transactions on Pattern Analysis and Machine Intelligence*, 22(11):1130–1134, 2000.
- [70] Del Din. *Innovative Techniques for Biomechanical Evaluation of Stroke Survivors: Combined fMRI-Gait Analysis Assessment and Fugl-Meyer Clinical Scores Estimation Through Wearable Sensors*. PhD thesis, University of Padova, 2012.
- [71] Gennery. Visual tracking of known three-dimensional objects. *International Journal of Computer Vision*, 7:243–270, 1992.
- [72] Allard et al. *Three-dimensional analysis of human movement*. 1995.
- [73] Yan et al. Physiological origin of low-frequency drift in blood oxygen level dependent (bold) functional magnetic resonance imaging (fmri). *Magnetic Resonance in Medicine*, 61:819–827, 2009.

List of Figures

1.1	Examples of different types of grip. a Power grip. b Precision grip. [2]	12
1.2	Kinematics of grasping. a Hand preshaping during its journey to the target. b Grip aperture during the overall movement. c Representation of traces demonstrating the scaling of maximum grip aperture with respect to object size. [2]	14
1.3	The visuomotor grasping circuit in the monkey cerebral cortex. [2]	16
1.4	Motor cortical areas and somatosensory areas.	17
1.5	Brodmann areas.	18
1.6	Motor homunculus (left side) and sensory homunculus (right side).	19
2.1	MRI scanner. [57]	24
2.2	Volume coils. [56]	26
2.3	Gradient coils. [57]	26
2.4	Random spin orientation. [56]	27
2.5	Spin precession. [56]	27
2.6	Net magnetization.	27
2.7	Spiral path of the net magnetization.	28
2.8	Longitudinal (left side) and transverse (right side) relaxation. [57]	30
2.9	Effects of blood deoxygenation upon MR relaxation constants. [56]	31
2.10	Sequence of events after stimulus presentation.	32
2.11	Neuronal events that trigger the HDR and cause the fMRI BOLD response. [58]	32
2.12	Hemodynamic response. [57]	33
2.13	Relative changes in cerebral blood flow (CBF) and cerebral blood volume (CBV) following neuronal activity. [56]	33
2.14	Blocked experimental design. [59]	34
2.15	Event-related experimental design. [59]	35
2.16	Schematic representations of the fMRI BOLD hemodynamic response. a HDR to a single short-duration stimulus. b HDR to a block of multiple consecutive stimuli. [56]	35
2.17	Interpolation to correct slice timing errors.	36
2.18	Head restraint systems. a Volume head coil with a bite bar system and a vacuum pack [56]. b Thermoplastic mask [56]. c Immobilization mask.	37

2.19	Head rotations. [60]	38
2.20	Plots of head motion over an experimental session. [56]	38
2.21	Functional (left side) and structural (right side) images. [56]	38
2.22	Typical coordinate system for fMRI data. [56]	39
2.23	Gaussian filter 2D. [60]	39
2.24	Gaussian filter 3D. [60]	39
2.25	Original functional image (left side) and smoothed image (right side). [56]	40
2.26	Steps from data preprocessing to data statistical analysis. [61]	40
2.27	Matrix notation of the General Linear Model.	41
2.28	Canonical function (red), temporal derivative (dashed blue) and dispersion derivative (dashed green). [59]	43
2.29	Possible results of a significance test.	44
2.30	Effects of Bonferroni correction. [56]	45
3.1	The point P projection on the image plane in the 3D space. [68]	49
3.2	Pin-hole model. [68]	50
3.3	3D reconstruction performed from 2D views recorded from two cameras. [65]	50
3.4	Graphical representation of the triangulation method. [70]	51
3.5	Devices used for the Wand Calibration.	52
3.6	Examples of markers labels.	53
4.1	Reflective passive markers with plastic support.	56
5.1	Parallelepiped used for the Static Calibration.	58
5.2	Positions of the markers on the parallelepiped used for the Static Calibration.	58
5.3	The static "L" and the moving Wand.	58
5.4	Position of the 3 markers on the right hand.	60
5.5	Experimental setup of data acquisition.	60
5.6	The SPM12 base window.	62
5.7	Batch Realign: Estimate & Reslice.	63
5.8	Batch Segment.	63
5.9	Segmented gray matter.	63
5.10	Batch Coregister.	64
5.11	Normalized mutual information coregistration.	64
5.12	Batch Normalise.	65
5.13	Batch Smooth.	66
5.14	Normalized image (top) and common space (bottom).	66
5.15	Batch Specify 1st-level.	72
5.16	Design matrix using the canonical model (model 1).	72
5.17	Design matrix using the canonical temporal derivatives model (model 2).	72

5.18	Design matrix using the canonical dispersion derivatives model (model 3).	72
5.19	Batch One-sample t-test.	74
5.20	Batch Multiple Regression.	75
5.21	Design matrix with kinematic covariates.	75
5.22	Settings of the p-value and the voxels extent threshold.	76
6.1	Measurements of the length of an object obtained using the Static Calibration video (red) and the Wand-Calibration video (green).	80
6.2	Translation and rotation movements of the participant with the smallest head movements amplitude (participant n° 4).	80
6.3	Translation and rotation movements of the participant with the largest head movements amplitude (participant n° 9).	80
6.4	Example of the spline interpolation: original data (top) and interpolated data (bottom).	81
6.5	Example of the first-order low-pass filter with a cut-off frequency of 8 Hz: interpolated data (red) and filtered data (green).	81
6.6	Examples of the 4 kinematic quantities profiles.	82
6.7	Examples of graphical representation of some kinematic parameters derived from the wrist absolute velocity	83
6.8	Examples of graphical representation of some kinematic parameters derived from the wrist absolute acceleration.	83
6.9	Examples of graphical representation of some kinematic parameters derived from the grip aperture.	84
6.10	Examples of graphical representation of some kinematic parameters derived from the grip aperture absolute velocity.	84
6.11	Examples of graphical representation of the regression line of the 4 pairs of parameters that demonstrated a higher linear correlation (from participant n° 9).	86
6.12	Examples of β images regarding the 4 kinematic regressors (from participant n° 1, slice 20).	88
6.13	Graphical representation of the BOLD signal and the hemodynamic response function using the three models (from participant n° 1, session 1).	89
6.14	Graphical representation of the BOLD signal and the hemodynamic response function using the three models (from participant n° 9, session 1).	90
6.15	SPMs derived from <i>strategy I</i> .	93
6.16	SPMs derived from <i>strategy IV</i> .	94
6.17	SPMs derived from <i>strategy VII</i> .	95
6.18	SPM obtained from <i>contrast 4</i> using the <i>strategy IV</i> without the participant n° 9 (p-value=0.005 and voxel extent threshold=10).	96
6.19	SPM obtained from <i>contrast 4</i> using the <i>strategy IV</i> without the participant n° 9 (p-value=0.005 and voxel extent threshold=15).	96

List of Tables

2.1	T1 and T2 values at 1.5 T field strength.	30
2.2	Advantages and disadvantages of blocked and event-related designs.	35
5.1	Coordinates of the marker centers [cm] on the parallelepiped used for the Static Calibration.	59
5.2	Summary of all the strategies adopted.	67
5.3	Mean values of the maximum wrist absolute velocity (<i>parameter 4</i>), the maximum grip aperture (<i>parameter 6</i>) and the maximum grip aperture absolute velocity (<i>parameter 8</i>).	75
6.1	Mean values of all the trials for the <i>parameters 3, 4, 6, 8, 10</i> and <i>12</i> for each participant.	85
6.2	Examples of slope of the fitted line for every pair of parameters (from participant n° 9).	85
6.3	Examples of determination coefficient r^2 for every pair of parameters (from participant n° 9).	85
6.4	Determination coefficients r^2 between the <i>parameters 4 & 10</i> , <i>parameters 4 & 12</i> , <i>parameters 6 & 8</i> and <i>parameters 10 & 12</i> of each participant.	87
6.5	Residual Sum of Squares (RSS) using the canonical function (model 1), the canonical temporal derivatives function (model 2) and the canonical dispersion derivatives function (model 3).	91
6.6	Akaike Information Criterion (AIC) using the canonical function (model 1), the canonical temporal derivatives function (model 2) and the canonical dispersion derivatives function (model 3).	91

Ringraziamenti

Vorrei ringraziare innanzitutto la Prof.ssa Alessandra Bertoldo e il Prof. Umberto Castiello per aver permesso la realizzazione di questa tesi, per la loro immensa disponibilità e per avermi trasmesso il giusto entusiasmo per intraprendere questo percorso.

Ringrazio la Prof.ssa Chiara Begliomini che mi ha affiancato dal principio al termine nello svolgimento della tesi, sempre presente per chiarire ogni mio dubbio e curiosità.

Ringrazio Philipp, Matthias e Julian che mi hanno accolta nel loro laboratorio, per i loro preziosi insegnamenti e per esser sempre stati disposti a rispondere alle mie domande anche a distanza.

Grazie a Tommaso, Erica e Matteo per il loro fondamentale aiuto e i loro utili consigli.

Ringrazio tutti i miei amici, quelli "di sempre", quelli incontrati durante il periodo universitario e quelli conosciuti durante i miei anni vissuti a Padova. Grazie per avermi supportato durante questo percorso, per le risate, i pranzi in compagnia, il tempo trascorso in aula studio, gli aperitivi, le serate, i viaggi e per aver condiviso con me momenti indimenticabili che porterò sempre nel mio cuore.

Ed infine un grazie speciale ai miei familiari ed in particolare ai miei genitori, Giovanna e Maurizio, che mi sono sempre stati vicini, mi hanno incoraggiato e sostenuto rispettando le mie scelte, che sono sempre stati dei punti di riferimento e senza i quali non avrei potuto raggiungere questo importante traguardo.